AN EXPERIMENTAL AND COMPUTATIONAL STUDY OF NITROGEN ACTIVATION ON PROMOTED RUTHENIUM CATALYSTS

by

Emil Sebastian Gutterød

Thesis for the degree of
Master of Science

Department of Chemistry
Faculty of Mathematics and Natural Sciences
University of Oslo

May 2016

Preface

This thesis finalizes the Master of Science degree in Chemistry, at the Department of Chemistry, University of Oslo. The experimental and computational work has been conducted in the group for Solid State Electrochemistry (FASE), at the Center for Materials Science and Nanotechnology (SMN) in the time period from August 2014 to May 2016.

First of all, I would like to thank my supervisors, Professor Reidar Haugsrud and Jonathan M. Polfus for all their guidance and support throughout the entire period. I am also thankful to all members of the PlusUltra project for the opportunity to participate in educative and inspiring meetings at SINTEF.

Moreover, I wish to thank the entire FASE group, Adrian Lervik for valuable assistance with TEM, and especially Matthias Schrade for creating a pleasant office environment as well as for help with proofreading.

Most of all I wish to thank my family for being supportive and showing a great deal of interest all these years, and I am truly grateful to Marry for always believing in me.

University of Oslo, May 2016

Emil Sebastian Gutterød

Abstract

Ruthenium based catalysts for ammonia synthesis have been studied extensively following the industrial adoption of a promoted carbon supported ruthenium catalyst in the Kellogg Advanced Ammonia Process (KAAP). Nevertheless, there are still fundamental aspects such as the dissociative adsorption of nitrogen—generally regarded as the rate determining step of NH_3 synthesis—and the influence of the barium promoter, not fully explored. In the present work, the activation of nitrogen on barium promoted ruthenium is elucidated through a combined experimental and computational approach.

Nitrogen dissociation and association on a clean and barium promoted Ru(0001) step were investigated through DFT based calculations using VASP. Unpromoted dissociation was found to proceed with an energy barrier of $51\,\mathrm{kJmol^{-1}}$, with a N-N distance of the transition state (TS) of 1.864 Å. The calculated activation barrier for association was $135\,\mathrm{kJmol^{-1}}$, which increased to $161\,\mathrm{kJmol^{-1}}$ when diffusion of atomic nitrogen along the terrace was considered. Upon promotion by a unit of atomic Ba, BaOH and BaO at the step, the dissociation barrier decreased rather similarly by 21, 18 and $18\,\mathrm{kJmol^{-1}}$, respectively. The chemical state of the promoting unit was determined to have a larger effect on the association barrier, which decreases by 19, 10 and $5\,\mathrm{kJmol^{-1}}$, respectively. A previously not reported local energy minimum state with one nitrogen atom adsorbed on the b5-hcp site and the other at a step-bridge site was identified. A significant stabilization of the local minimum state is observed upon promotion: the N-N distance of the initial and final state of dissociation increased (which can be associated with a weakening of the N-N bond), while it decreased for the TS and the local minimum state. The promoting effect decreases rapidly with increasing distance to the dissociating nitrogen, indicating that the interactions were of electronic nature.

Powdered catalyst samples of Ru-Ba/AC were prepared by $Ba(NO_3)_2$ wet-impregnation of 5 wt% Ru on activated carbon. The nitrogen isotope exchange (IE) reaction $^{14,14}N_2 + {}^{15,15}N_2 = 2^{14,15}N_2$ on Ru-Ba/AC was investigated in the temperature range 320–750°C at N_2 pressures of 20–230 mbar, by means of gas-phase analysis with mass spectrometry (GPA-MS). Apparent isotope exchange activation energies in range 162–$178\,\mathrm{kJmol^{-1}}$ were obtained below 425°C. This is in good agreement with the literature and the present computational results. At higher temperatures the apparent activa-

tion energy abruptly decreases to 64–88 $\mathrm{kJmol^{-1}}$. It is suggested that the change in temperature dependence is due to limitations by pore diffusion at higher temperatures. In the presence of 1 mbar water vapor in the temperature range 575–625°C, the isotope exchange rate was significantly reduced compared to under dry conditions, and the apparent activation energy increased from $88 \pm 2\,\mathrm{kJmol^{-1}}$ to $126 \pm 12\,\mathrm{kJmol^{-1}}$. When water vapor was introduced, evolution of H_2 was observed, indicating that oxidation of partially reduced Ba occurred in the presence of H_2O. Isotherms of the isotope exchange rate showed reaction orders with respect to nitrogen partial pressure of 0.83 ± 0.05 and 0.88 ± 0.03 at 625°C and 700°C, respectively, and 1.1 at 450°C. All of which are in good agreement with values reported in literature for NH_3 synthesis.

Deactivation of the catalyst was observed at temperatures above 500°C, resulting in a significantly decreasing IE rate with time. In accordance with reports from literature, and the computational and experimental results, it is proposed the isotope exchange rate and activation energy are highly dependent on the chemical state of the barium promoter, which is further dependent on the environmental conditions, such as temperature and the presence of water vapor.

Contents

1 Introduction

In a world with an increasing population of more than 7 billion, the demand for food is extraordinarily high. In order to meet this demand, extensive production and utilization of fertilizers to increase crop yields are vital. Fertilizers are produced in nature through the process of biological nitrogen fixation; nitrogen from air is converted to ammonia by microorganisms, catalyzed by enzymes of nitrogenase. Fixation of nitrogen also occurs during thunderstorms, where during lightning nitrogen and oxygen are combined. These natural sources of nitrogen fixation are however only responsible for barely half of the annual fixation; the other half is anthropogenic [1].

1.1 Motivation and background

At the beginning of the 20^{th} century a discovery that would later revolutionize the agricultural industry, was made. The German chemist Fritz Haber managed to successfully synthesize ammonia from its elements by reacting nitrogen from air with hydrogen in the presence of an iron catalyst at high pressures and temperatures [2]. Up until that point, the main source of fixated nitrogen had been sodium nitrate extracted from the high-mountain deserts of Chile, and ammonium sulfate, a by-product of the coal distillation process [2]. However, the extent of the source of sodium nitrate was clearly limited, and even though much work was put into optimizing the production from coal distillation, the low yield of the process would not be able to uphold the world's increasing demand for fixated nitrogen [2]. It was clear, a demand of this magnitude could only be met by utilizing the largest source of nitrogen available; elemental nitrogen in the atmosphere.

Some years after Fritz Haber's groundbreaking discovery of ammonia synthesis, Carl Bosch was able to develop the process on an industrial scale, and the result of this was the well-known Haber-Bosch process:

$$N_2 + 3H_2 \rightleftharpoons 2NH_3 \quad \Delta H = -91.8\,\mathrm{kJmol}^{-1} \tag{1.1}$$

The impact the Haber-Bosch process had on the world was remarkable. As a result of all the available ammonia, development and production of nitrogen-containing explosives during the First World War were made possible for Germany without the need for import, and this may in fact have contributed to extending the duration

of the war [3]. However, most importantly, the agricultural industry was revolutionized. In fact, ammonia-based fertilizers are estimated to be responsible for supporting approximately 27% of the world's population over the past century [3]. Moreover, estimations for 2008 indicate that as much as 48% of the human population are fed due to Haber-Bosch fixated nitrogen. In order to produce such a massive amount of ammonia, a corresponding large amount of hydrogen also has to be produced. Unlike nitrogen, hydrogen is not abundant in the atmosphere, instead, steam reforming of natural gas is the predominating source of hydrogen:

$$CH_4 + 2H_2O \rightleftharpoons 4H_2 + CO_2 \tag{1.2}$$

Considering the fact that climate change is on the brink of no return, the use of steam reforming as source of H_2—which not only consumes a rather large amount of energy, but also produces CO_2—may be regarded as one of the main disadvantages of the current Haber-Bosch process. Although there is no direct greenhouse gas emission in the Haber-Bosch process, the need of relatively high temperatures and pressures (typically around 400–600 °C and 200–400 bar) also require a large amount of energy, and if H_2 is produced from fossil fuels, indirect emissions will be major.

The magnitude of these disadvantages, however, could be significantly reduced by using renewable energy and a non-fossil source of hydrogen. Another way the process could be improved with respect to environmental impact is by reducing the amount of energy consumed. In order to do so, catalysts that allows for milder working conditions are a necessity. This is to some extent achieved with ruthenium based catalysts, which allows for a higher yield of ammonia at lower temperatures and pressures, compared to the conventional iron based catalysts implemented in most of the ammonia industry.

A substantial amount of research has been done in the field ever since Fritz Haber's discovery, and especially in the nineties and early two-thousands, much of the focus was directed toward various ruthenium based catalysts. Even so, increased fundamental insight in all parts of the process is—in addition to being of academic interest—still important to develop new and better catalysts that will further improve, or even revolutionize, the process of ammonia synthesis.

1.2 Aim of the thesis

The aim of the thesis is to address fundamental aspects of the catalytic activation of nitrogen on barium promoted ruthenium, in a combined experimental and computational approach.

In the computational approach, various aspects of the dissociation and association of nitrogen on the ruthenium surface will be addressed on the basis of Density Functional

Theory calculations. A main focus is the influence of the barium promoter on the energy barriers of dissociation and association on various sites and steps of the Ru catalyst surface.

In the experimental approach, nitrogen isotope exchange $^{14,14}N_2 + {}^{15,15}N_2 = 2\,{}^{14,15}N_2$ under variable conditions—e.g. high temperatures up to 750°C, pressures of 20–230 mbar and in the presence of water vapor—will be addressed on a barium promoted ruthenium catalyst supported on activated carbon, Ru-Ba/AC. Gas-phase analysis with mass spectrometry (GPA-MS) will be used for the investigation.

2 Theory

2.1 Surface activity of transition metals

The active component of a heterogeneous catalyst is usually a transition metal. In this section, a brief description of the interaction between a diatomic molecule and a transition metal surface—based on Concepts of Modern Kinetics and Catalysis by Chorkendorff and Niemantsverdriet (2007)[4]—is presented. For a detailed explanation, the reader is referred to the original text.
In brief, when a second period diatomic molecule, such as CO, O_2 or N_2, approaches a transition metal surface, a chemisorption bond (i.e. bonding due to rearrangement of the electron structure) may form due to overlapping wavefunctions and projection of metal states onto the molecule. The interaction with the metals sp-orbtials lowers and broadens the originally bonding 5σ and antibonding $2\pi^*$ orbitals of the molecule, while the interaction with the d-orbitals splits both into pairs of bonding and antibonding chemisorption orbitals (Fig. 2.1). These are filled with electrons up to the Fermi level. Occupancy of the originally antibonding orbitals strengthens the bond between the metal and the molecule, but weakens the intramolecular bond. If the originally antibonding orbitals are filled sufficiently, the intramolecular bond may break, giving two isolated atomic adsorbates, relaxing into separate local minima. This dissociation process is usually referred to as "back donation".

In general, when focusing on the late transition metals, the chemisorption energy is to a large degree determined by the interaction between the $2\pi^*$ antibonding orbitals and the metal d-band. The energy contribution from this interaction can be estimated by the hybridization energy, which can be described according to

$$\Delta E_{\text{d-hyb}} \approx -2f\frac{\beta_{2\pi}^2}{\epsilon_{2\pi} - \epsilon_d} + 2f\gamma_{2\pi}\beta_{2\pi}^2 \tag{2.1}$$

where f is the degree of filling, β is the resonance integral—describing the bonding strength due to orbital overlap—$\epsilon_{2\pi}$ and ϵ_{d} are the energies of the 2π orbital and the energy of the center of the d-band, respectively, and $\gamma_{2\pi}$ is a proportionality constant. The first term in Eq. 2.1 is attractive, and the second is repulsive. Going from left to right in the transition metal series, the d-band gradually narrows and decreases in

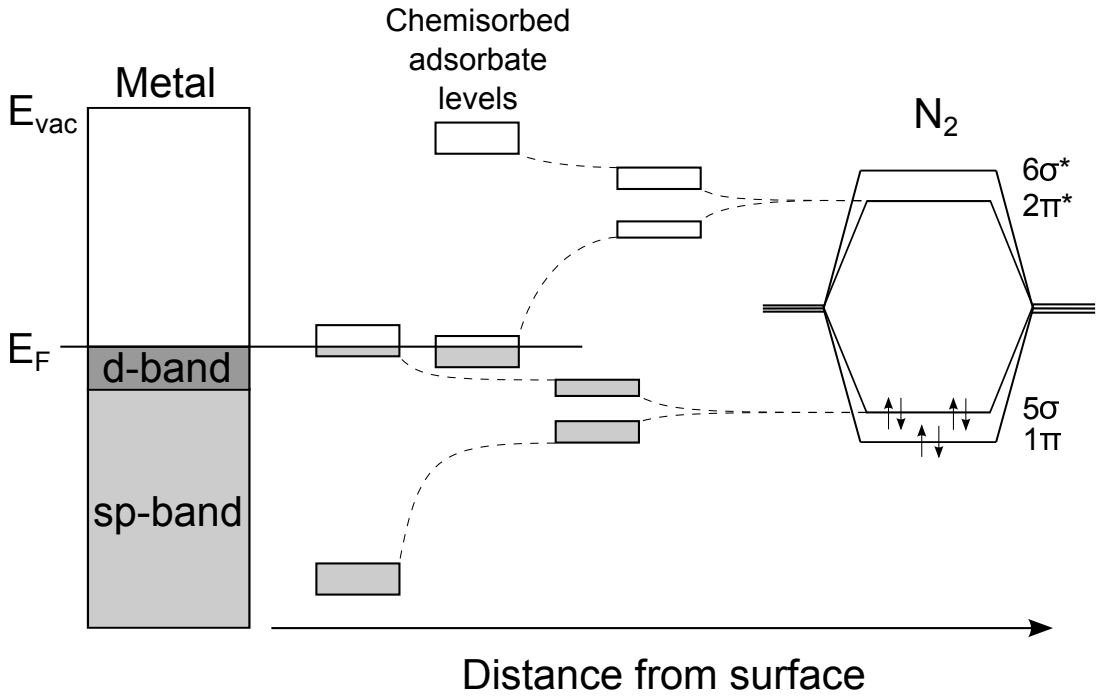

Figure 2.1: Conceptual figure of the interaction between the bonding and antibonding orbitals of N_2 with the sp- and d-bands of a transition metal. The orbitals are lowered in energy and broadened by the sp-band, while split into bonding and antibonding chemisorption orbitals by the d-band. The figure is redrawn from [4].

energy due to less overlap between of the d-orbitals. In light of this, it is clear that the term $\epsilon_{2\pi} - \epsilon_{\mathrm{d}}$ increases and thus the attractive interaction decreases, from left to right. Accordingly, the reactivity of the metal and strength of the chemisorption bond also decreases to the right.

For a metal to function as a good catalyst, a strong chemisorption bond alone is not adequate. A metal on the left side of the late transition metals, e.g. iron, may easily dissociate a molecule due to a very strong interaction, however, because of this, the adsorbed species may be so strongly bound to the surface that its reactivity becomes low. In other words, the interaction should be strong, but not too strong for a good catalyst. This is the essence of Sabatier's Principle: the rate of a catalytic reaction is a function of the heat of adsorption, and exhibits a maximum. Usually, when plotting the activities of different heterogeneous catalysts for a given reaction as function of a quantity related to the bond-strength between the catalyst and participating species, a so-called volcano plot is obtained [5, 6, 7]. This is illustrated in Fig. 2.2, where the activity for ammonia synthesis of several transition metals at similar conditions is plotted versus d-band occupancy. Molybdenum and Rhenium, metals to the left, are

capable of dissociating N_2, but the products—adsorbed nitrogen atoms—are bound strongly and have low reactivity. To the right, the metals are barely capable of slowly breaking the strong N_2 triple bond. In the middle, metals exhibiting the highest NH_3 activity are found: the group 8 metals Iron, Ruthenium and Osmium.

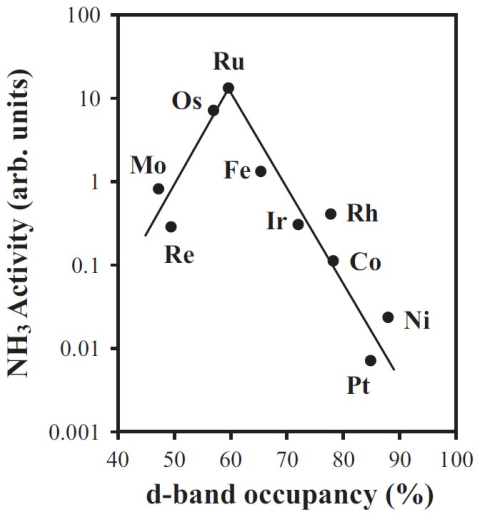

Figure 2.2: Catalytic activity for ammonia synthesis of various transition metals as function of d-band occupancy (%). The figure is taken from [4].

2.2 Surface kinetics

2.2.1 Reaction rate theory

The rate at which a chemical reaction occurs, and how it is related to a reaction mechanism—describing how molecules react via intermediates to products—as well as to macroscopic parameters such as pressures and temperatures, can be described through reaction kinetics. In a reaction between two arbitrary molecules, A and B, where molecule C is formed,

$$\nu_a \mathrm{A} + \nu_b \mathrm{B} \underset{k^-}{\overset{k^+}{\rightleftharpoons}} \nu_c \mathrm{C} \tag{2.2}$$

with forwards and backwards rate constants, k^+ and k^-, and stoichiometric coefficients ν_a, ν_b and ν_c, the rate of reaction is defined as the rate at which products are formed, or reactants disappear. For a reaction that occurs in gas phase, the rate expression may be written:

$$r = -\frac{1}{\nu_a}\frac{\mathrm{d}p_\mathrm{A}}{\mathrm{d}t} = -\frac{1}{\nu_b}\frac{\mathrm{d}p_\mathrm{B}}{\mathrm{d}t} = \frac{1}{\nu_c}\frac{\mathrm{d}p_\mathrm{C}}{\mathrm{d}t} \tag{2.3}$$

Here the partial pressures p represent relative quantities—i.e. partial pressures. For an elementary reaction—which is a reaction that cannot be further divided into substeps—the rate is equal to

$$r = k^{+} p_a^{\nu_a} p_b^{\nu_b} - k^{-} p_c^{\nu_c} \tag{2.4}$$

Reactions in heterogeneous catalysis are often rather complex and almost always occur in a series of elementary steps, such as adsorption, dissociation, adsorbent-adsorbent reactions and desorption. For that reason, it might be useful to express the rate of reaction as function of all partial pressures, in the form of a power rate law

$$r = k p_a^{n_a} p_b^{n_b} p_c^{n_c} \tag{2.5}$$

where n_i is the reaction order with respect to component i, defined as $n_i \equiv \dfrac{\partial \ln(r)}{\partial \ln(p_i)}$. Elementary reactions assume integer reaction orders that are independent of conditions (e.g. temperature and pressure), while non-elementary reactions can take any number and are valid only within a narrow range of conditions. By plotting the logarithm of the rate as function of the logarithm of the partial pressure of one component, the reaction order with respect to that particular component can be extracted from the slope:

$$\ln(r) = \ln(k p_b^{n_b} p_c^{n_c}) + n_a \ln(p_a) \tag{2.6}$$

Measurements of the pressure dependency of the rate may therefore give valuable information of the reaction, and help to optimize process parameters in industrial processes.

2.2.2 Temperature dependence of the rate

In thermally activated reactions, the rate increases with temperature. For an elementary reaction, the temperature dependency is given by the Arrhenius equation:

$$k(T) = \nu \mathrm{e}^{-E_\mathrm{a}/RT} \tag{2.7}$$

where k is the rate constant, ν is a pre-exponential factor and E_a is the activation energy—the potential energy barrier that has to be overcome for a reaction to complete. In the Arrhenius equation, the prefactor is assumed to be independent of temperature, however, transition state theory shows that the prefactor may in fact be proportional to T^x, where x is a number dependent on the type of reaction. Even so, the Arrhenius equation is still a very good approximation since the exponential term dominates the dependency. As stated earlier, reactions are usually not dependent on one elementary step alone; to describe the temperature dependence of an overall reaction a term for

an *apparent* activation energy must be introduced:

$$E_{\text{app}} \equiv RT^2 \frac{\partial \ln(r)}{\partial T} \tag{2.8}$$

Through this term, the contribution from thermodynamics is included in the temperature dependence of the rate. For that reason—similarly to the case of reaction order of a non-elementary reaction—the validity of the apparent activation energy often limited to a restricted range of conditions.

2.2.3 Adsorption of diatomic molecules

The first step of every heterogeneous catalytic reaction is the adsorption of one or more reactants onto a catalytically active surface. Here the focus is on gaseous reactants. For a diatomic molecule this can occur in two ways: the molecule adsorbs to the surfaces in its molecular form, or it *directly* dissociates upon adsorption. These two scenarios are referred to as associative- and dissociative adsorption, respectively. For N_2, the reaction equations may be written as

$$\mathrm{N_2}(g) + * \underset{k_1^-}{\overset{k_1^+}{\rightleftharpoons}} \mathrm{N_2}* \tag{2.9}$$

$$\mathrm{N_2} * + 2* \underset{k_2^-}{\overset{k_2^+}{\rightleftharpoons}} 2\mathrm{N}* \tag{2.10}$$

Free and active adsorption sites on the surface are denoted $*$, and adsorbed species are marked with an asterisk, $*$. In the cases above, the rate of each reaction is given by

$$r_{\mathrm{N_2}} = \frac{\mathrm{d}\theta_{\mathrm{N_2}}}{\mathrm{d}t} = k^+_{\mathrm{N_2}} p_{\mathrm{N_2}} \theta_* - k^-_{\mathrm{N_2}} \theta_{\mathrm{N_2}} \tag{2.11}$$

$$r_{\mathrm{N}} = \frac{\mathrm{d}\theta_{\mathrm{N}}}{\mathrm{d}t} = k^+_{\mathrm{N}} p_{\mathrm{N_2}} \theta_*^2 - k^-_{\mathrm{N}} \theta_{\mathrm{N}}^2 \tag{2.12}$$

where the species and free sites are described as site fractions, θ. On a surface with n chemically equal adsorption sites that each can be occupied by one adsorbate, the number of a given adsorbate i is $n\theta_i$. Thus, the sum of all site fractions are equal to unity. In this way the rate is site specific and has unit of reactions per site, commonly referred to as the turnover frequency (TOF). At equilibrium, the rate expressions above are equal to zero, and by utilizing that $\theta_* = (1 - \theta_i)$, the surface coverage of nitrogen may be written as function of the equilibrium constant for the reaction and

nitrogen partial pressure

$$\theta_{N_2} = \frac{K_{N_2} p_{N_2}}{1 + K_{N_2} p_{N_2}} \tag{2.13}$$

$$\theta_N = \frac{\sqrt{K_N p_{N_2}}}{1 + \sqrt{K_N p_{N_2}}} \tag{2.14}$$

which represent the Langmuir adsorption isotherms for associative- and dissociative adsorption, respectively.

If more than one species can adsorb on a surface, the coverage of each is influenced by the other. This is known as competitive adsorption. In competing adsorption between CO and N_2, following Eq. 2.9 and 2.10, respectively, the coverage of each species may be written as

$$\theta_N = \frac{\sqrt{K_N p_{N_2}}}{1 + \sqrt{K_N p_{N_2}} + K_{CO} p_{CO}} \tag{2.15}$$

$$\theta_{CO} = \frac{K_{CO} p_{CO}}{1 + \sqrt{K_N p_{N_2}} + K_{CO} p_{CO}} \tag{2.16}$$

Here $\theta_* = 1 - \theta_N - \theta_{CO}$ is utilized. When the coverage of CO increases, that of N decreases, and vice versa. Competitive adsorption also has importance for determination of reaction parameters: for example, in a reaction where one surface species A binds more strongly than another B (i.e. $K_A > K_B$), the pressure of B may be increased as compensation.

2.3 Isotope exchange (IE)

The rate at which gas molecules dissociate and associate on a surface is a measure of its activity. This can be investigated at a fundamental level through utilization of isotopically labeled gas and measurements of the isotope exchange (IE) rate, r_{IE}. In this section, the theory behind such measurements is explained. Most of the content in this section is based on Hörnlund (2002)[8] and Byrne and Belton (1983)[9].

2.3.1 Dissociation

Imagine a closed system where a catalyst surface is exposed to a diatomic homonuclear gas, such as nitrogen, with isotopes ^{14}N and ^{15}N, at a given temperature and pressure. In this system, three different species of N_2 may exist, $^{28}N_2$, $^{29}N_2$ and $^{30}N_2$, and hence,

three possible surface reactions may occur:

$$^{28}\mathrm{N}_2 \rightleftharpoons 2^{14}\mathrm{N}_{\mathrm{ad}} \tag{2.17}$$

$$^{29}\mathrm{N}_2 \rightleftharpoons {}^{14}\mathrm{N}_{\mathrm{ad}} + {}^{15}\mathrm{N}_{\mathrm{ad}} \tag{2.18}$$

$$^{30}\mathrm{N}_2 \rightleftharpoons 2^{15}\mathrm{N}_{\mathrm{ad}} \tag{2.19}$$

Where the overall isotope exchange reaction is defined as

$$^{28}\mathrm{N}_2 + {}^{30}\mathrm{N}_2 \rightleftharpoons 2^{29}\mathrm{N}_2 \tag{2.20}$$

If the gas molecules and the adsorbed atoms are in equilibrium, and the isotopes are assumed to be chemically identical—which is a fair assumption for nitrogen since the masses are roughly the same—then the isotopic coverage is completely random. Thus, the probability of forming a given molecular species may be found through combinatorial analysis:

$$P^f_{28} = I^2_{14} \tag{2.21}$$

$$P^f_{29} = 2I_{15}I_{14} \tag{2.22}$$

$$P^f_{30} = I^2_{15} \tag{2.23}$$

where P^f_m is the probability of forming molecular species m and I_i is the relative abundance, or fraction, of isotope i, i.e., $I_{14} + I_{15} = 1$. Similarly, the probability that the dissociating N_2 is a specific isotope species is simply given by the respective relative molecular fraction. For example, the probability that the dissociating molecule is $^{29}\mathrm{N}_2$ is I_{29}. As time goes by and $t \to \infty$, the relative abundance of each molecular species approach the statistical equilibrium fraction, I_{eq}, which is equal to the respective probability of formation, P^f. How quickly this is reached is determined by the rate at which molecules decompose and reform on the surface, i.e., the rate of exchange r_{IE}.

2.3.2 Time evolution

To describe the time evolution of a given species, say $^{29}\mathrm{N}_2$, four different exchange reactions must be considered. Firstly, $^{29}\mathrm{N}_2$ dissociates while $^{28}\mathrm{N}_2$ or $^{30}\mathrm{N}_2$ forms, secondly, $^{28}\mathrm{N}_2$ or $^{30}\mathrm{N}_2$ dissociates while $^{29}\mathrm{N}_2$ forms, thirdly, $^{29}\mathrm{N}_2$ both dissociates and forms, and fourthly, $^{29}\mathrm{N}_2$ does neither. Only the first two scenarios contribute to a change in I_{29}. If the formation of $^{29}\mathrm{N}_2$ is taken as the positive direction, the rate at which I_{29} changes with time may be written as the rate at which scenario two occurs, minus the rate of scenario one:

$$\frac{\mathrm{d}I_{29}}{\mathrm{d}t} = r^i_{\mathrm{IE}} I^{29}_{\mathrm{eq}}(1 - I_{29}) - r^i_{\mathrm{IE}} I_{29}(1 - I^{29}_{\mathrm{eq}}) = r^i_{\mathrm{IE}}(I^{29}_{\mathrm{eq}} - I_{29}) \tag{2.24}$$

here r^i_{IE} has unit s^{-1}. If the rate of exchange is expressed in mole per second per gram, the equation becomes

$$\frac{\mathrm{d}I_{29}}{\mathrm{d}t} = \frac{RTm_{\mathrm{cat}}}{p_{\mathrm{N_2}}V} r_{\mathrm{IE}}(I^{29}_{\mathrm{eq}} - I_{29}) \tag{2.25}$$

which is solved to obtain the expression for I_{29} as function of time:

$$I_{29}(t) = I_{\mathrm{eq}} + (I_0 - I_{\mathrm{eq}})\exp\Big(- \frac{RTm_{\mathrm{cat}}}{p_{\mathrm{N_2}}V} r_{\mathrm{IE}} t\Big) \tag{2.26}$$

here I_0 is I_{29} at $t = 0$, m_{cat} is the mass of the catalyst and V is the volume of the closed system.
The exchange rate can further be evaluated by curve fitting Eq. 2.26, or by rearranging the equation to get r_{IE} as the negative slope:

$$\xi = \ln\Big(\frac{I_{29}(t) - I_{\mathrm{eq}}}{I_0 - I_{\mathrm{eq}}}\Big)\frac{p_{\mathrm{N_2}}V}{RTm_{\mathrm{cat}}} = -r_{\mathrm{IE}}t \tag{2.27}$$

Any changes in the rate during an experiment are observed using Eq. 2.27.

2.4 Quantum mechanical modeling of functional materials

This section briefly treats the theory behind quantum mechanical modeling using Density Functional Theory (DFT). Subsections 2.4.1 and 2.4.2 are mostly based on "Brief Introduction to the Density Functional Theory" - Lecture Notes to MSc course FYS-MENA4111 by Prof. Clas Persson [10], while 2.4.3 is based on Sholl and Steckel (2009)[11].

2.4.1 Many-particle Schrödinger equation

The properties of any given system of atoms or molecules can be analyzed theoretically by solving the time-independent, non-relativistic, many-particle Schrödinger equation:

$$H\Psi(\boldsymbol{r}, \boldsymbol{R}) = E\Psi(\boldsymbol{r}, \boldsymbol{R}) \tag{2.28}$$

E is the total energy of the system and $\Psi(\boldsymbol{r}, \boldsymbol{R})$ is the many particle wavefunction with $\boldsymbol{r}$ and $\boldsymbol{R}$ describing the coordinates of all electrons and nuclei, respectively. H is the Hamiltonian operator, describing the total energy of the system

$$H = T_{\mathrm{e}}(\boldsymbol{r}) + T_{\mathrm{n}}(\boldsymbol{R}) + U_{\mathrm{ee}}(\boldsymbol{r}) + U_{\mathrm{nn}}(\boldsymbol{R}) + U_{\mathrm{en}}(\mathbf{r}, \boldsymbol{R}) \tag{2.29}$$

where the two first terms describe the kinetic energy of all electrons and nuclei, respectively, the two following describe the repulsive electron-electron and nucleus-nucleus

interactions, respectively, and the last describes attractive electron-nucleus interactions.

When the number of electrons and nuclei in the system increases, the number of interactions and terms describing these increases accordingly, and solving the equation then becomes huge numerical problem. Another problem with the many-particle Schrödinger equation is that we do not know how to operate H on the many-particle wavefunction $\Psi(\boldsymbol{r}, \boldsymbol{R})$. The first step on the way to overcome this problem is to simplify the wavefunction through the Born Oppenheimer Approximation (BOA) by assuming that it can be separated into an electronic and nuclear part. In essence, this is based on the two following arguments: *i*) nuclei are believed to be point like charges. *ii*) the nuclei are moving slowly in comparison to the electrons due to the much higher mass, and hence, if a nucleus moves, the electrons are expected to follow instantaneously; i.e., the nuclei positions are fixed. The second step can for example be to approximate the overall wavefunction from linear combination of atomic orbitals (LCAO) [12], or to utilize Density Functional Theory (DFT) and the Kohn-Sham equation (KS-equation) to generate an exact total energy for an approximated wavefunction. As DFT and the KS-equation is utilized in the present work, this is further treated in the following subsection.

2.4.2 DFT and the Kohn-Sham equation

The fundamental idea of DFT is that the ground-state electron density of a system, $n_0(\boldsymbol{r}) = |\Psi_0(\boldsymbol{r})|^2$, determines all physical ground-state properties of that system; i.e., they are all functionals of the electron density. For the ground-state energy this may be written $E_0 = E[n_0]$. This is essentially the first of the two Hohenberg-Kohn theorems, in which DFT is based upon. The second theorem states that there exists a variational principle for the energy density functional, in a way that if the electron density n is not the ground-state density, n_0, then $E[n_0] < E[n]$. This means that the electron density that minimizes the energy functional, is the true ground-state electron density. According to the theorems of DFT, the exact energy of a system can be calculated if we know the exact electron density, and the energy functional can be written

$$E[n] = T[n] + U_{\mathrm{ee}}[n] + U_{\mathrm{en}}[n] \tag{2.30}$$

where $T[n]$ and $U_{\mathrm{ee}}[n]$ is the kinetic energy of the many-electron system and the many-electron interaction energy, respectively, and $U_{\mathrm{en}}[n]$ is the interactions between the electrons and nuclei. A problem is, however, that we do not know the form of the unique functionals of the two first terms. In the KS approach—leading to the KS-equation—this is overcome by rewriting the equation in order to incorporate the many-electron terms into a another term called the *Exchange-Correlation Energy*,

$E_{\mathrm{xc}}[n]$:

$$E[n] = T_{\mathrm{s}}[n] + U_{\mathrm{s}}[n] + U_{\mathrm{en}}[n] + \Big((T[n] - T_{\mathrm{s}}[n]) + (U_{\mathrm{ee}}[n] - U_{\mathrm{s}}[n])\Big) \tag{2.31}$$

$$= T_{\mathrm{s}}[n] + U_{\mathrm{s}}[n] + U_{\mathrm{en}}[n] + E_{\mathrm{xc}}[n] \tag{2.32}$$

Here $T_{\mathrm{s}}[n]$ and $U_{\mathrm{s}}[n]$ is the kinetic and the electron-electron interaction energy, respectively, of a Hartree-like total wavefunction written as a product of auxiliary independent single-particle wavefunctions, $\Psi_j(\boldsymbol{r})$ (an ansatz used in the derivation of the KS-equation). By minimizing the energy with respect to $\Psi_j(\boldsymbol{r})$ under constraint, eventually the KS-equation is obtained:

$$\left\{ -\frac{\hbar^2}{2m_{\mathrm{e}}}\nabla_j^2 + V_{\mathrm{H}}(\boldsymbol{r}) + V_{\mathrm{en}}(\boldsymbol{r}) + V_{\mathrm{xc}}(\boldsymbol{r}) \right\} \Psi_j(\boldsymbol{r}) = \epsilon_j \Psi_j(\boldsymbol{r}) \tag{2.33}$$

The first term describes the kinetic energy of electron j, $V_{\mathrm{H}}(\boldsymbol{r})$ is the Hartree-potential, describing the electron-electron interaction the single-electron wavefunction feels, $V_{\mathrm{en}}(\boldsymbol{r})$ is the external potential, $V_{\mathrm{xc}}(\boldsymbol{r}) = \dfrac{\partial E_{\mathrm{xc}}[n]}{\partial n}$ is the exchange-correlation potential and ϵ_j is the single-electron energy. Through combination and rearrangement of Eq. 2.32 and 2.33, we get a new expression for the total energy:

$$E[n] = \sum_j \epsilon_j - \frac{1}{2}\int\int q^2 \frac{n(\boldsymbol{r})n(\boldsymbol{r'})}{|\boldsymbol{r} - \boldsymbol{r'}|} d\boldsymbol{r} d\boldsymbol{r'} + E_{\mathrm{xc}}[n] - \int V_{\mathrm{xc}}(\boldsymbol{r}) n(\boldsymbol{r}) d\boldsymbol{r} \tag{2.34}$$

Here the second term describes the electron-electron interaction energy. If $E_{\mathrm{xc}}[n]$ is exact, the total energy obtained is also exact; however, the exact form of $E_{\mathrm{xc}}[n]$ is not known. How this term can be approximated is addressed in the following subsection. As closing remarks of this subsection, some advantages and disadvantages of the KS-equation are listed:

Some advantages of the KS-equation are

- If $E_{\mathrm{xc}}[n]$ is exact, the energy is exact.
- Implementation of new approximations for $E_{\mathrm{xc}}[n]$ is trivial.
- Any electronic system can be described.

and some disadvantages are

- The exact expression of $E_{\mathrm{xc}}[n]$ is not known.
- Because of this, we cannot know if the variational method is accurate.
- It is not a full DFT method.

2.4.3 Approximations for the exchange-correlation energy

The *Local-Density Approximation* (LDA) is the original and the most simple approximation to the exchange-correlation functional. In the LDA, $V_{\text{xc}}(\boldsymbol{r})$ is approximated to that of a uniform electron gas, with equal density as the local electron density of the system [11]:

$$V_{\text{xc}}^{\text{LDA}}(\mathbf{r}) = V_{\text{xc}}^{\text{electron gas}}[n(\boldsymbol{r})] \tag{2.35}$$

From this it follows that at total uniformity, the LDA is correct. In bulk materials, where electron density is usually varying rather slowly, the LDA is a better fit than in the case of atoms or molecules—where the electron density is varying more quickly. In that case, the LDA fails. The *Generalized Gradient Approximation* (GGA) builds on the LDA and is a commonly used method for approximating the exchange-correlation energy. In the GGA, the electron density gradient is included in the potential:

$$V_{\text{xc}}^{\text{GGA}}(\mathbf{r}) = V_{\text{xc}}^{\text{electron gas}}[n(\mathbf{r}), \nabla n(\mathbf{r})] \tag{2.36}$$

This feature enhances the flexibility of the method and making it more suitable for describing real materials, while still being correct at total uniformity.

2.5 Thermodynamic properties from DFT

Since the energy obtained from DFT is purely the electronic contribution to the energy (cf. BOA in subsection 2.4.1), physical properties are evaluated at 0 K, and possible effects of temperature are hence not included. These effects can however be included through the Gibbs free energy

$$G = H - TS \tag{2.37}$$

where H is enthalpy and S is entropy. Using that $H = U + pV$, where U is the electronic energy including zero-point correction, the expression for Gibbs energy becomes

$$G = E_{\text{el}} + E_{\text{ZPE}} + pV + dH_{T,0} - TS \tag{2.38}$$

with E_{ZPE} as the vibrational zero-point energy and $dH_{T,0}$ as the temperature correction of the enthalpy, i.e., the change in enthalpy when going from 0 K to a given temperature T. For solids the pV term becomes very small compared to the other terms, and can hence be neglected [13]:

$$G_{\text{solid}} = E_{\text{el}} + E_{\text{ZPE}} + dH^{T,0} - T(S_{\text{vib}} + S_{\text{conf}}) \tag{2.39}$$

S_{vib} and S_{conf} is the vibrational- and configuration entropy, respectively. For gases, at constant volume, the Gibbs energy is written as the chemical potential as a function of temperature and pressure:

$$\mu_{\text{gas}} = E_{\text{el}} + E_{\text{ZPE}} + dH_{T,0} - TS + k_{\text{B}}T\ln(p/p^0) \tag{2.40}$$

Here p^0 is a reference pressure, usually taken as 1 bar. The terms $dH_{T,0}$ and S are tabulated values calculated from the gas phase heat capacity. The equations 2.39 and 2.40 can be used further to calculate the Gibbs energy of reaction.

2.5.1 Adsorption

In the case of adsorption of a gas species on a solid surface, the Gibbs energy of reaction may be written

$$\Delta G(\text{ads}) = G(\text{solid surface w/adsorbate}) - G(\text{clean solid surface}) - N\mu(\text{gas}) \tag{2.41}$$

where N is the number of molecules adsorbed in the reaction. By assuming that the presence of the adsorbate does not significantly change the enthalpy nor the entropy of the solid itself, these terms cancel out. The only contributions to the entropy of the solid surface w/adsorbate is then the vibrational entropy of the adsorbates, $S^{\text{ad}}_{\text{vib}}$, and the coverage dependent configurational entropy, $\Delta S^{\theta}_{\text{conf}}$. The former may be written as [14]

$$S^{\text{ad}}_{\text{vib}} = Nk_{\text{B}}\Big\{\frac{\beta\epsilon}{e^{\beta\epsilon}-1} - \ln(1-e^{-\beta\epsilon})\Big\} \tag{2.42}$$

where $\beta = 1/k_{\text{B}}T$ and $\epsilon = \sum_i h\nu_i$ is the total vibrational energy of the adsorbent obtained from normal-mode analysis DFT calculations, and the latter may be included as [15]

$$\Delta S^{\theta}_{\text{conf}} = k_{\text{B}}\ln\left(\frac{1-\theta}{\theta}\right) \tag{2.43}$$

where θ is the surface coverage. The expression for Gibbs energy of adsorption then becomes

$$\Delta G(\text{ads}) = \Delta E^{\text{ads}}_{\text{el}} + \Delta E^{\text{ads}}_{\text{ZPE}} - dH^{\text{gas}}_{T,0} - T\left(\Delta S^{\theta}_{\text{conf}} + S^{\text{ad}}_{\text{vib}} - S^{\text{gas}}\right) - Nk_{\text{B}}T\ln(p/p^0) \tag{2.44}$$

with the electronic adsorption energy defined as $\Delta E^{\text{ads}}_{\text{el}} = E^{\text{surf+ad}}_{\text{el}} - E^{\text{surf}}_{\text{el}} - NE^{\text{gas}}_{\text{el}}$. If the adsorption reaction is at equilibrium and follows second order Langmuir adsorption kinetics (Eq. 2.14), the surface coverage may be written as function of Gibbs energy

of adsorption:

$$\theta = \frac{\sqrt{\exp(-\frac{\Delta G}{RT})p}}{1 + \sqrt{\exp(-\frac{\Delta G}{RT})p}} \tag{2.45}$$

Here the relationship $K = \exp(-\frac{\Delta G}{RT})$ is utilized.

3 Literature

In this chapter, a review of literature reports relevant for the present work is presented. A brief overview of ammonia synthesis is initially given before the interaction between nitrogen and the ruthenium surface is addressed. The focus is thereafter directed towards promoted Ru on activated carbon Ru-Ba/AC, before a final section on the isotope exchange of nitrogen on Ru catalysts.

3.1 Ammonia synthesis

Both Iron and Ruthenium have received much attention as active metals in catalysts for ammonia synthesis. Ruthenium, which shows the highest NH_3 activity (see Fig. 2.2), was in the beginning of the nineties used for the first time as an industrial catalyst in the Kellogg Advanced Ammonia Process (KAAP), where the high low-temperature low-pressure activity is utilized [16]. However, much due to the high prize of Ru, Iron is still the most commonly used metal in industrial catalysts.

The metal alone does not exhibit all the properties required of a catalyst for applications. Since the reactions occurs at the metal surface, a high surface area is essential. Using lumps or shots of metal is then out of the question. Using fine metal powder would also be problematical, mainly because small metal particles are unstable and prone to sinter at elevated temperatures. Thus, surface area would decrease with time. This problem may be prevented by forming small metal particles on the surface of a porous, thermally stable and chemically inert support. A large number of materials meet these criteria where the most common are Al_2O_3, MgO, CaO and active carbon (activated charcoal, AC) [4]. In addition to the structural supports, alkaline and alkaline-earth compounds are usually added to increase the overall catalytic activity. The promoting effect is related to the electronegativity and size—i.e. charge density—of the compounds, explained by electrostatic interactions between the promoter and adsorbate [17]. The highest promoting activity is encountered for Ba, Cs and K, which are all rather large and have low electronegativity [18].

3.1.1 Primary steps in catalytic ammonia synthesis on Ru

It is well accepted [19, 20, 21, 22] that the mechanism of the reaction between N_2 and H_2 to ammonia catalyzed by ruthenium

$$N_2 + 3H_2 \overset{Ru}{\rightleftharpoons} 2NH_3 \tag{3.1}$$

can be described by the following elementary reaction steps:

$$N_2 + 2* \rightleftharpoons 2N* \tag{3.2}$$

$$H_2 + 2* \rightleftharpoons 2H* \tag{3.3}$$

$$N* + H* \rightleftharpoons NH* + * \tag{3.4}$$

$$NH* + H* \rightleftharpoons NH_2* + * \tag{3.5}$$

$$NH_2* + * \rightleftharpoons NH_3* + * \tag{3.6}$$

$$NH_3* + * \rightleftharpoons NH_3 + * \tag{3.7}$$

$$\tag{3.8}$$

The mechanism is nearly identical to that of the reaction catalyzed by iron, however, in that case an adsorbed state of molecular nitrogen is usually included [19, 21, 23, 24, 25]. For both Fe and Ru-based catalyst, the dissociation of N_2 is generally considered to be the rate determining step of ammonia synthesis.

3.2 Adsorption, activation and desorption of N_2 on Ru(0001)

In 1997, Mortensen et al. [26] investigated N_2 adsorption and dissociation on a Ru(0001) surface by means of DFT. The N_2 molecule was found to adsorb on top site oriented perpendicularly to the surface (Fig. 3.1), with an adsorption energy of -45 and -59 $kJmol^{-1}$ per molecule, at coverages of 1/4 and 1/3 ML (monolayer), respectively. Experimentally this adsorption state has been found to saturate at -178°C at a coverage of 0.35 ML [27]. The rate of desorption was shown—through temperature-programmed-desorption (TPD) measurements—to peak at -145°C at low coverages, and at -154°C at saturation [27]. Feulner et al. [28] similarly reported the desorption peak to shift from -149 to -160°C with increasing coverage. Based on first-order desorption kinetics and neglecting adsorbate-adsorbate interactions, the adsorption energy was estimated to -30 $kJmol^{-1}$.

The dissociative adsorption of nitrogen follows second order Langmuir-Hinselwood kinetics (Eq. 2.14) [4, 29, 30, 31], i.e. dissociation occurs immediately upon adsorption

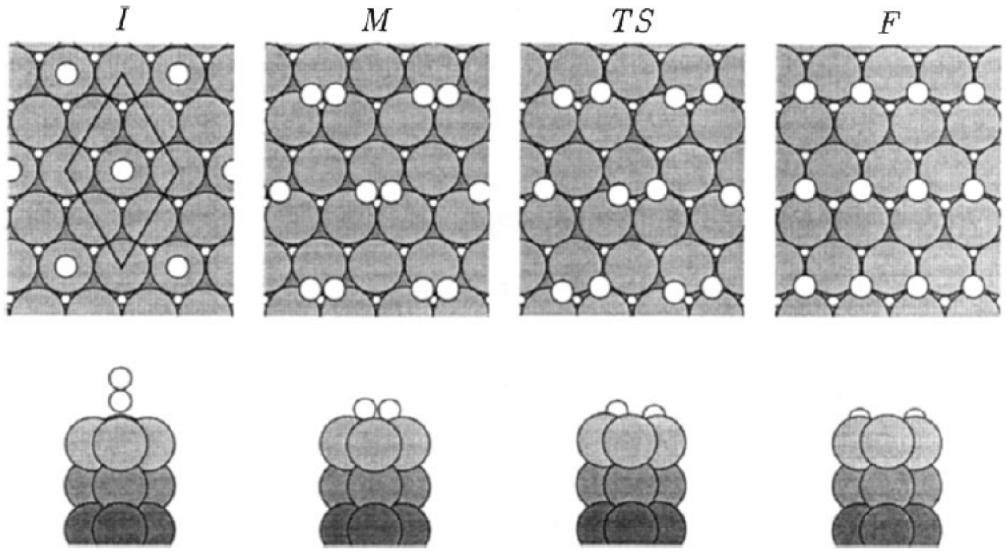

Figure 3.1: Illustration of notable configurations of nitrogen along the reaction path in the dissociation of N_2 on Ru(0001). The top figure is a top view, and the bottom figure is a side view. I, M, TS and F marks the configurations of the initial and metastable molecular states, transitions state and final state, respectively. The figure is taken from [26].

with practically non-existing adsorbed molecular species, and in the process, two active sites are occupied. In the dissociation pathway suggested by Mortensen et al. [26], shown in Fig. 3.1, the perpendicularly adsorbed molecule orients planar to the surface in a metastable state with its center-of-mass in hollow site, and the atoms are oriented towards bridge site. This intermediate state increases the overlap between the nitrogen 2π orbitals and rutheniums 5d orbitals (section 2.1), and dissociation is facilitated. The transition state (TS) was characterized by a N-N bond length of 1.9 Å. Here one atom is close to the final hcp site—found to be the most stable site for atomic nitrogen—while the other is still at bridge. A further increase in the intra-molecular distance and decrease in energy leaves both atoms at adjacent hcp sites. Agreeing results have been reported by Murphy et al. [32].

Mortensen et al. [26] calculated the dissociation process using a model corresponding to a 1/2 ML coverage of atomic nitrogen after the dissociation. When the coverage was decreased to 1/4 ML both the adsorption energy of the hcp-adsorbed nitrogen atoms and the activation barrier of dissociation decreased. The former from -37 to -150 $\mathrm{kJmol^{-1}}$ per molecule, and the latter decreased by 15 $\mathrm{kJmol^{-1}}$ to 130 $\mathrm{kJmol^{-1}}$. This can be explained by a rather large N-N repulsion when the nitrogen atoms share Ru-atoms at coverages higher than 1/4 ML [26]. Since the adsorption energy at the

hcp site is influenced by the proximity of other adsorbents, the energy of the system will be lowered if the N-atoms disperse through diffusion after dissociation [26]. The diffusion barrier was found to be 90 $kJmol^{-1}$, which is in good agreement with results from scanning tunneling microscopy [33].

In single crystal studies of the Ru(0001) surface, the activation barrier of N_2 dissociation is ranging from around 36 up to above 200 $kJmol^{-1}$, dependent on the experimental method [29, 34, 35]. Values obtained from single crystal adsorption experiments—determination of sticking coefficient by exposing the single crystal surface to a given dosage of N_2 at constant temperature for a given duration of time—falls in the lower range, while molecular beam studies show upper range values. This is explained by a highly site-dependent activation barrier, and furthermore, that the different experimental techniques (thermal methods and molecular beam studies) are to a large degree site-specific [29, 35, 36].

3.2.1 Site specific activity

On the ruthenium surface—as on all metal surfaces—atomic steps are always present in small concentrations (e.g. 1%). And since the step Ru-atoms are low-coordinated, the d-band is raised in energy compared to that of the terrace atoms, leading to a higher reactivity [4, 29, 36]. Dahl et al. [29, 36] showed that the initial sticking coefficient was much higher on a clean Ru(0001) compared to an Au-passivated Ru(0001) surface. This is because Au preferentially adsorbs on and blocks the especially active steps, which makes the passivated surface representative of a flat, step-less surface (i.e. terrace). At 227°C the difference in initial sticking coefficients between the two cases was seven orders of magnitude. Similarly, in the temperature-programmed desorption (TPD) experiments, the desorption peak of the passivated surface was shifted up roughly 123°C, which corresponds to a desorption barrier difference of about 73 $kJmol^{-1}$ between the two surfaces. The energy barriers for adsorption and desorption on the terrace and on the step are shown in Fig. 3.2. Since the steps dominate the N_2 activity of Ru(0001), the activation barrier measured in thermal methods is that of the step, while generally in molecular beam studies, the most abundant sites—even if the activation barrier is higher—will mostly be probed due to the high energies used [29, 35, 36]

Through computational methods Dahl et al. [36] further elucidated the difference in N_2 activation barrier between terrace and step sites. A 144 $kJmol^{-1}$ difference was found, corresponding to barriers of 183 $kJmol^{-1}$ and 39 $kJmol^{-1}$, at the terrace and step, respectively. The difference may be explained by the number of Ru atoms

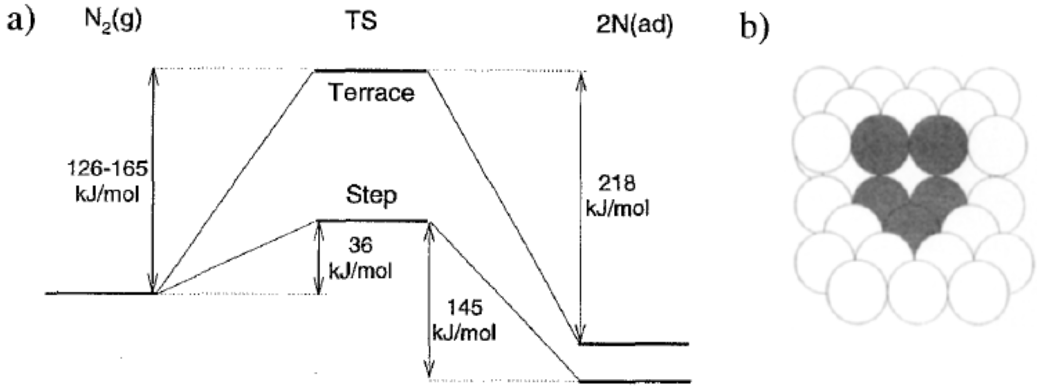

Figure 3.2: (a) A schematic illustration of the desorption and adsorption barriers clean and Au-passivated Ru(0001), representing the activity of step and terrace Ru(0001), respectively. (b) Illustration of the active so-called b5 step site (black atoms). The figure is taken from [29].

associated with the transition state; four at the terrace in contrast to five at the step. Because of one additional Ru atom participating in the process, the N-N repulsion in the TS is reduced, hence lowering the energy [36]. Furthermore, a lower dissociation barrier is usually associated with a stronger bonding of products—in this case atomic nitrogen—to the surface (see section 2.1). However, this is not the case for the step-dissociation. The high activity towards ammonia synthesis of the steps can therefore be seen as due to a low activation energy in combination with fewer products blocking the active sites [36].

3.2.2 Promoted Ru(0001)

The effect of alkali promotion of Ru(0001) on adsorption and dissociation of N_2 was investigated through computational methods by Mortensen et al. [37]. The minimum energy path (MEP) of dissociation was calculated according to the same procedure as in Ref. [26] for clean and promoted surfaces. In the presence of 1/8 and 1/6 ML of isolated hcp-adsorbed Na and Cs atoms, respectively, the molecularly adsorbed N_2 at top site is raised (destabilized) slightly in energy. This is also true for the metastable state lying flat on the surface. However, the transition state is stabilized (decreased in energy), and in combination with destabilizing the molecular state, this results in the barrier of dissociation being lowered by $13\,\mathrm{kJmol^{-1}}$ due to the presence of Na, and $28\,\mathrm{kJmol^{-1}}$ due to Cs. This—as was the case with activation on the stepped surface—is somewhat contradictory to what is expected: a lowering of the barrier is usually accompanied with more stable adsorbents [37]. The effect of the proximity of the promoter was also investigated by fixing the geometry of the TS as the position was

changed. The activation barrier decreased with a decreasing distance to the promoters. Mortensen et al. [37] explained this by electrostatic interactions between the promoter and the TS nitrogen dominating the promotion effect.

In a follow up paper [38], the interaction between nitrogen and the promoter was described as an attractive dipol-dipol interaction which decreases with distance (r) approximately as $1/r^3$. Sulfur, which is known to be poison in ammonia synthesis [4], was found to instead increase the barrier of dissociation. However, this was not explained by electrostatic repulsion, but rather due to the S-atom forming covalent bonds with three Ru atoms resulting in weaker bonds to the nitrogen transition state [38].

The electrostatic effect of promoters has been explained by Lang et al. [39] based on a model of adsorbed electropostive and electronegative atoms on a uniform electron gas surface (see LDA in section 2.4.3): adsorbed electropostive atoms, such as the alkali metals, induces a negative electrostatic potential on neighboring sites on the surface, while the opposite is true for the electronegative atoms, such as S and Cl. Whether or not another adsorbate is stabilized because of the atoms setting up the potential is then dependent on the nature of the adsorbing molecule [39].

3.3 Promoted Ru/AC

3.3.1 Structural outline

Active carbon supports (AC) have in general a high surface area up to $1500\,\mathrm{m}^2 g^{-1}$, with pore-volume from around 0.10 to $1\,\mathrm{cm}^3\mathrm{g}^{-1}$, both dependent on the source of raw carbon, as well as treatment temperatures and atmospheres (carbon pretreatment) [16, 40, 41].

Carbon pretreatment (graphitization) was shown by Forni et al. [40] to be related to the degree of unwanted methanation, i.e., the formation of methane in a reaction between the carbon support and hydrogen at elevated temperatures. For catalysts on non-pretreated supports and supports pretreated at 1500°C under inert atmosphere, methane formation started at 500°C and increased substantially up to 700°C (highest measured temperature). However, for the catalysts on supports pretreated at temperatures above 1900°C, the methane formation dropped dramatically in the temperature range 500–600°C, but increased slowly from 600°C up to 700°C. This suggests the pretreatment temperature and degree of graphitization as an important factor in support stability [40].

On the various types of AC supports, nano-particles of ruthenium are usually formed in the size regime below 10 nm in diameter, commonly through impregnation methods using precursors such as $Ru_3(CO)_{12}$, $RuCl_3$ or $Ru(NO)(NO_3)_3$ [42, 43, 44]. The amount

of Ru in the catalysts generally varies in range 1–9.1 wt% [42, 43, 44, 45]. Promotion of Ru/AC with potassium, cesium or barium is usually done through aqueous impregnation from either a solution of the respective hydroxides or the nitrates [40][46], where the promoter is homogeneously dispersed over both the supporting material and the ruthenium surface. The effect of the barium load on the activity of ammonia synthesis is treated in a later section.

3.3.2 The effect of the nature of the promoter

In a comparison with a commercial Fe-based catalyst, Kowalczyk et al. [47] showed that the rate of ammonia synthesis—with respect to the weight of ruthenium and the carbon support—was 5 times higher for K promoted Ru/AC and up to 10 times higher for Ba promoted Ru/AC. When the same comparison was done with respect to catalyst bed volume, the rate was 2 times higher for the Ru-Ba/AC catalyst compared to the Fe-based one, since the bed volumes of the Ru/AC catalysts were much larger. The activity measurements were performed in a reactor with ammonia content of 8%, and as Ru is less sensitive to an increase in NH_3 content compared to Fe [48], a larger different in catalytic activity is expected with increasing NH_3 content [47].

In another study by Kowalczyk et al. [49] the activity of Cs promoted Ru/AC was found to be slightly higher than K promoted. As the activity of Ru-Ba/AC was shown in Ref. [47] to be 5 times higher than the latter, it is indicated that the effects of the three promoters can be ranked as Ba$\gg$Cs>K [46]. In contrast, Forni et al. [40] reported the promoting effect to increase as Cs>Ba$\gg$K. In order to explain contradicting order of the promoting effect, Rarorg et al. [46] studied the effect of the three promoters on the kinetics of NH_3 formation. The general conclusions were as follows: Ba is more sensitive both to variations in ammonia concentration in gas phase and total pressure. However, the reaction rate of ammonia synthesis on the alkali promoted catalysts is more dependent on the Ru dispersion. Therefore, the ranking of the promoters varies both with reaction conditions and Ru dispersion. Nevertheless, the effect of Cs was alway higher than that of K.

Rosetti et al. [18] showed that the presence of promoters also affect the support stability in relation to methanation. At 700°C, addition of a small amount of Ba (Ba/Ru atomic ratio of 0.6) reduced the degree of methanation by about 75% compared to the unpromoted catalyst. Further improved resistance towards methanation was observed when either K or Cs was added in addition to Ba. When all three promoters were present, methanation was barely detectable.

3.4 Ru-Ba/AC

In this section, relevant literature regarding the barium promoted ruthenium catalyst investigated in the experimental part of the present work is presented. As Ru-Ba/AC is a catalyst for NH_3 synthesis, the focus in the literature is mainly in this regard.

3.4.1 Decomposition of $Ba(NO_3)_2$

In 2009, Truszkiewicz et al. [43] thoroughly investigated the working state of the barium promoter. High-temperature x-ray diffraction (XRD) was performed while Ru-$Ba(NO_3)_2$/AC was activated in a flow of H_2 going up to 520°C. At 120°C $Ba(NO_3)_2$ started to decompose while $BaCO_3$ formed. This signal peaked at 300°C. The signal of BaO was not observed until at approximately 480°C. The author suggest that $BaCO_3$ in fact forms from BaO and CO_2 (BaO +CO_2 = $BaCO_3$) at moderate temperatures, while at higher temperatures, the reaction is shifted to the left. Carbon dioxide can possibly be produced by $2H_2O$ + C = CO_2 +$2H_2$, or originating from oxygen-containing functional groups on the support surface. At 520°C the only present Ba-containing phase was BaO, and the signal increased with time, indicating that the phase becomes more ordered [43]. Hansen et al. [44] suggested through high-resolution transmission electron microscopy (TEM) studies that some of the BaO takes the form of a BaO_x monolayer partly covering the surface of a small amount of the Ru crystals.

In a similar experiment, Truszkiewicz et al. [43] monitored the evolving gases as the raw-catalyst (Ru-$Ba(NO_3)_2$/AC) was activated through a temperature ramp to above 700°C in reducing atmosphere (Fig. 3.3). At around 100°C—a temperature corresponding to the decomposition of $Ba(NO_3)_2$—consumption of H_2 started, while H_2O, NH_3 and CO formed, possibly from the following reaction [43]:

$$Ba(NO_3)_2 + 8H_2 \rightleftharpoons BaO + 2NH_3 + 5H_2O \tag{3.9}$$

The formation of CO may be originating from oxygen-containing functional groups. Decomposition of $Ba(NO_3)_2$ through reaction 3.9 is also suggested by Zeng et al. [45]. Moreover, only small amount of CO_2 was present in the gas phase, indicating that the amount of $BaCO_3$ is small. The same activation process was performed for a sample without ruthenium, i.e., only barium on AC, and no consumption of H_2 or evolution of gas species was observed below 400°C. This means that Ru is catalyzing the decomposition of $Ba(NO_3)_2$ shifting it down almost 300° [43]. Facilitation of $Ba(NO_3)_2$ decomposition by Ru is also suggested by Zeng et al. [45].

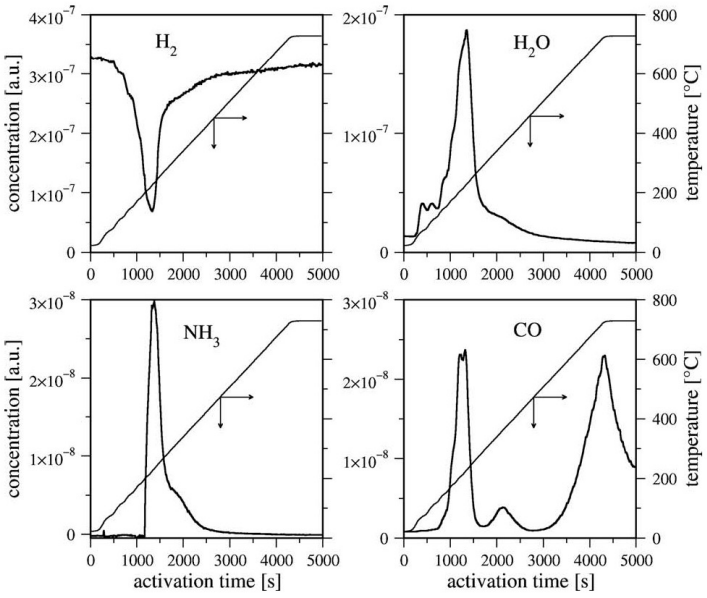

Figure 3.3: Concentration of the main components in gas phase under temperature-programmed-reduction in a stream of 6%H_2/Ar, measured by MS as function of activation time and temperature. The figure is taken from [43].

3.4.2 The effect of the promoter load

Liang et al. [16] showed that for Ba promoted 4 wt% Ru, the ammonia concentration (volume %) in the effluent gas at 400°C and 300 bar increased from close to zero for an unpromoted catalyst, up to just below 5 vol% when the Ba/Ru molar ratio was equal to unity (Fig. 3.4). A further increase in the ratio up to 6.2 only slightly increased the ammonia output. In addition to changes in the ammonia output, also the Ru dispersion was affected: an increased Ba/Ru ratio from 0.5 up to 1 nearly doubled the dispersion, while it barely changed when the amount was further doubled. When increasing the Ba/Ru ratio to 6.2, the dispersion was reduced in half. This lead to a nearly equal turnover frequency (TOF) for the three lowest ratios, while it was close to doubled for the highest. The author suggests that the activity is low when only a small amount of promoter is added, because some is consumed through reaction with surface anions originating from the the carbon support and Ru precursor. Moreover, it is further suggested that the reduced dispersion at higher promoter ratio might be related to blocking of the Ru surface and support pores [16].

Another explanation could be that some of the surface is blocked by the promoter but while doing so, the free sites are in closer proximity of the promoter as well. Since the effect of the promoter increases with the proximity (see section 3.2.2), the free sites should have an especially enhanced activity.

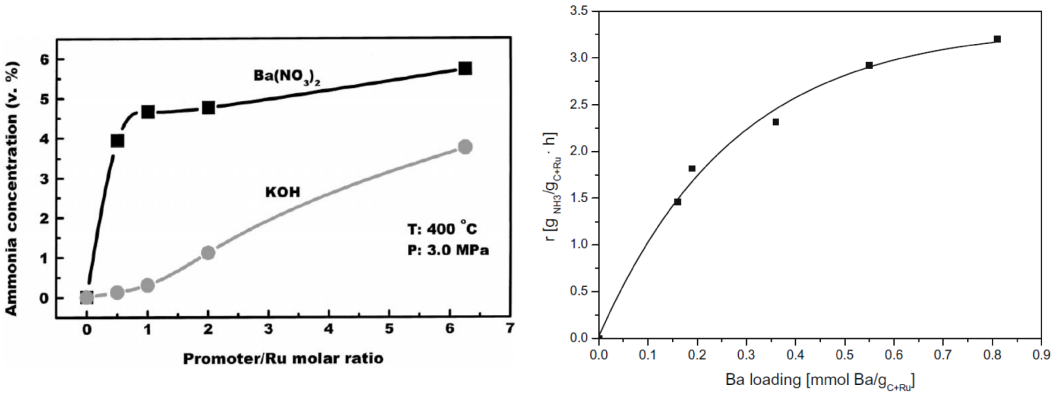

Figure 3.4: Ammonia concentration in effluent gas versus promoter/Ru molar ratio (left), and ammonia synthesis reaction rate versus Ba loading ($mmol/g_{C+Ru}$) (right). The figures are taken from [16] and [43], respectively.

A similar trend of increasing activity with Ba loading was shown by Truszkiewicz et al. [43]. At zero Ba loading the rate of ammonia synthesis was close to zero, while addition of $0.15\,mmol/g_{c+Ru}$ had a large effect, increasing the rate of synthesis to about $1.5\,g_{NH_3}/(g_{C+Ru}h)$ (Fig. 3.4). As the Ba loading was further increased, so was the rate; however, the effect of increased promoter loading was subsiding. The reaction conditions were 400°C, 63 bar and 8.5 % NH_3 in the gas stream, with 9.1 wt% Ru. The highest loading investigated was $0.81\,mmol/g_{C+Ru}$, which resulted in a rate of about $3.5\,g_{NH_3}/(g_{C+Ru}h)$. The loading of $0.81\,mmol/g_{C+Ru}$ corresponds to a Ba/Ru molar ratio of 0.9 (calculated from the known Ru wt%), which is close to the third data point in the figure of Liang et al. [16]. In both studies, the effect of the Ba:Ru ratio is shown to have largest effect on the activity of ammonia synthesis at ratios below one. Thus, the general effect of the Ba loading on the activity of ammonia synthesis is indicated to be fairly independent of Ru content, reaction pressure and the method of activity determination.

3.4.3 Influence of O_2

The interaction between O_2 and the catalyst was investigated at 0°C by Truszkiewicz et al. [43]. To elucidate specifically how the different components of the catalyst interacts with O_2, the O_2 consumption was measured on Ru/AC, and on Ru-Ba/AC and Ba/AC at different promoter loading, using a conventional fully automated temperature-programmed set-up with a thermal conductivity detector. The catalyst was initially pretreated at reaction conditions, then cooled in stream of He to 0°C before pulses of O_2 were added to the stream.

Blank samples of only the carbon support showed no O_2 consumption at 0°C, and the O_2 consumption of Ru/AC was hence attributed solely to Ru [43]. Furthermore, it was assumed that the O_2 consumption by Ru was the same in the promoted and unpromoted samples. The difference between the two was taken as the consumption of the Ba promoter. The total O_2 consumption of the unpromoted sample was about 300 μmol/g_{C+Ru}, in the samples with 0.36 and 0.81 mmol Ba/g_{C+Ru} this increases to about 400 and 500, respectively. This corresponds to O_2 consumption of 0.64 and 0.42 mol O per mol Ba. While the consumption was much lower for the Ba/AC samples, the same trend was followed; the total consumption increased from 55 to 300 μmol/g_{C+Ru} when the Ba loading was increased from 0.3 to 0.75 mmol Ba/g_{C+Ru}, corresponding to 0.37 and 0.29 mol O/mol Ba. This means that in both cases (i.e. with and without Ru) the consumption increased with increasing loading, however, the O/Ba ratio decreased [43].

A possible explanation for the higher O_2 consumption of Ru-Ba/AC compared to Ba/AC, could be that either the consumption by Ba is facilitated by Ru, the other way around, or that Ba is in another chemical state when bonded to AC as compared to Ru. It seems reasonable that Ru exhibits a different O_2 consumption in the presence of Ba (contrary to the assumption made by the authors) since active sites in close proximity of the promoter are highly activated. An increased activity for O_2 dissociation at sites nearby the promoter is for example seen in Na promoted Pt(111) [50].

Truszkiewicz et al. [43] argue that since the samples take up O_2, $Ba(OH)_2$ cannot be the only Ba-containing phase, as it is inert towards oxygen. Moreover, from the XRD results of [43] presented earlier, BaO is the main (crystalline) phase present; however, at 0°C BaO does not react with O_2. Thus, it is likely that a partially reduced form of Ba which reacts with O_2 is present [43].

3.4.4 Influence of H_2O

The influence of H_2O on three different catalyst systems, Ba/AC, Ru/AC and Ru-Ba/AC, was investigated by Truszkiewicz et al. [43]. After pretreatment at reaction temperature, the catalysts were cooled in flowing Ar down to 50°C. At this temperature, the catalyst was exposed a stream of wet Ar (7% H_2O) while the gas phase was monitored by a MS. In all cases, water was consumed and hydrogen evolved. The H_2 yield in the unpromoted sample was 15 μmol H_2/g_{C+Ru}, while in the promoted samples, the yield was significantly increased to 85 and 154 μmol H_2/g_{C+Ru}, in samples of 0.36 and 0.81 mmol Ba/g_{C+Ru}, respectively. In samples without Ru, the amount of evolved H_2 was more than 20 times less then of a Ru-containing samples with a corre-

sponding amount of Ba. The reduction degree of Ba, i.e. Ba^0/Ba_{total}, was calculated based on the assumption that H_2 can only form through the following reaction:

$$Ba + 2H_2O \rightleftharpoons Ba(OH)_2 + H_2 \tag{3.10}$$

The reduction degree was found to be 16 and 18 mol in the Ru-Ba/AC samples with low and high Ba content, respectively, and 20 times lower when Ru was not present. This means that Ba could be somewhat reduced by the carbon support, while Ru strongly facilitates the reduction [43]. Thus, in reducing conditions, it is likely that both metallic Ba and Ba(II) exist.

In a study by Zeng et al. [45] the rate of ammonia synthesis was found to significantly decrease with time at reaction temperatures below 450°C (Fig. 3.5). The observed

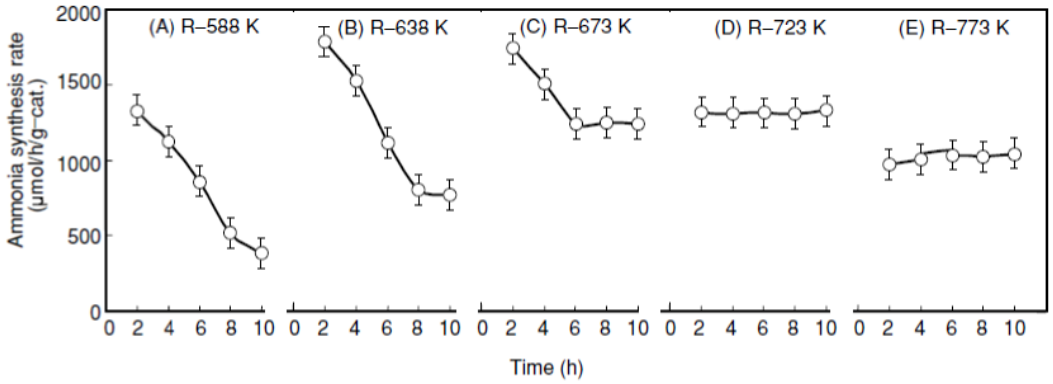

Figure 3.5: Ammonia synthesis rate ($\mu molh^{-1}g_{cat}^{-1}$) versus time at varying reaction temperature 1 atm. Prior to each measurement the catalyst was activated in H_2 at the 550°C for 3 h. The figure is taken from [45].

deactivation can be explained by a changing state of the promoter [45]. When the catalyst is reduced at 550°C, a given amount of active promoter is formed; however, at lower temperatures the equilibrium of the exothermic reaction

$$BaO + H_2O \rightleftharpoons Ba(OH)_2 \tag{3.11}$$

is more right shifted. Because of this, the amount of BaO—having a lower electronegativity than $Ba(OH)_2$ and should therefore be a more efficient promoter—gradually decreases with time through reaction with H_2O impurities in the feed [45]. Thus, the rate of ammonia formation also decreases with time.

At the higher temperatures the rate does not change with time, however, the level of the stable rate is lowered (Fig. 3.5). This can be explained by the temperatures

being sufficiently high for maintaining the initial amount of active promoter while at the same time limiting the thermodynamic equilibrium of ammonia synthesis, thus decreasing the level of the rate [45].

This was verified by investigating how the rate changed after feeding synthesis gas containing 31.7 mbar of water vapor for 5 minutes prior to a activity measurement [45]. At 315°C, the rate decreased to about 13% of the initial after exposure to water. Similar changes were observed at 365 and 400, and at all temperatures the catalysts were reactivated after a treatment in H_2 at 550°C [45]. After an initial drop in activity due to the water vapor in the feed, the initial rate was at 450 and 550°C recovered without an additional H_2 treatment [45].

Based on the results of both Truszkiewicz et al. [43] and Zeng et al. [45], it is reasonable that both the reactions

$$\mathrm{Ba} + 2\mathrm{H_2O} \rightleftharpoons \mathrm{Ba(OH)_2} + \mathrm{H_2} \tag{3.12}$$

$$\mathrm{BaO} + \mathrm{H_2O} \rightleftharpoons \mathrm{Ba(OH)_2} \tag{3.13}$$

and presumably

$$\mathrm{Ba} + \mathrm{H_2O} \rightleftharpoons \mathrm{BaO} + \mathrm{H_2} \tag{3.14}$$

may occur, dependent on pretreatment, temperature and water vapor pressure.

3.4.5 Activity of Ru-Ba/AC

The activity of a Ru-Ba/AC type catalyst depends on several factors such as promoter loading and state, Ru content and particle size [51], pretreatment [22, 45], carbon type [16, 22], ammonia content in the feed [46], and reaction pressure [46] and temperature [45]. In Table 3.1 a summary of ammonia synthesis activities reported in literature is presented. As can be seen from Fig. 3.6, the TOF is highly dependent on the pressure. Here, the logarithm of the TOFs listed in 3.1 are plotted versus the logarithm of the total reaction pressures. From a power rate law (Eq. 2.5) the reaction order with respect to total pressure can be estimated from the slope. The dependence on other parameters than the pressure is evident, especially at 30 bar. Overall, the highest reported TOF is $0.145\,\mathrm{s^{-1}}$. However, extrapolating the highest reported TOF of Ref. [16]($0.089\,\mathrm{s^{-1}}$) to higher pressures, a similar value is obtained. The lowest reported apparent activation energy is $72.5\,\mathrm{kJmol^{-1}}$ in temperature range 320–400°C, at 1 bar pressure, 9.1 wt% Ru and Ba/Ru ratio of 6.2 [42].

Table 3.1: Summarizing list of activities of NH_3 synthesis over Ru-Ba/AC catalysts reported in literature.

Rate (mol NH_3/(gs))	TOF (s^{-1})	Ba/Ru (mol/mol)	Ru (wt %)	T (°C)	p (bar)	Ref.
5.6×10^{-5}	0.14	0.97	9.1	400	90	[52][e]
5.3×10^{-5}	0.098	0.9	9.1	400	63	[43][a,d]
2.3×10^{-5}	n/a	0.6	9	400	60	[47][d]
4.3×10^{-5}	0.13	0.81	9.1	400	60	[41][d]
2.3×10^{-6}	0.02	6.2	9.1	400	10	[42]
6.2×10^{-7}	0.003	6.2	9.1	400	1	[42][b]
4.1×10^{-8}	0.003	6.2	1	400	1	[42][c]
3.9×10^{-9}	0.00016	6.2	1	320	1	[42]
3.5×10^{-7}	n/a	1	5	400	1.013	[45]
6.6×10^{-7}	0.089	6.2	4	400	30	[16]
2.8×10^{-8}	0.030	6.2	4	400	30	[16]
1.8×10^{-6}	0.041	6.2	4	400	30	[16]
1.9×10^{-6}	0.023	2	4	400	30	[16]
1.9×10^{-6}	0.024	1	4	400	30	[16]
1.1×10^{-6}	0.025	0.5	4	400	30	[16]
n/a	0.145	0.7	9.1	400	63	[46][d]

[a] $E_{app} = 100\,kJmol^{-1}$ (T = 370–400°C). [b,c] $E_{app} = 72.5$ and $88.8\,kJmol^{-1}$ (T = 320–400°C), respectively. [d,e] Inlet gas contains 8 and 10 vol. % NH_3, respectively.

3.5 Isotope exchange of nitrogen on Ru catalysts

The isotope exchange (IE) reaction is well suited to investigate the interaction of various materials with H_2 [53, 54] and O_2 [55, 56], and to some extent N_2 [57, 58]. In this section, relevant literature regarding N_2 isotope exchange on heterogeneous Ru-based catalysts is presented.

Hikita et al. [59] found isotope exchange rates (IER) of $7.7 \times 10^{-8}\,molg^{-1}s^{-1}$ and $6.7 \times 10^{-6}\,molg^{-1}s^{-1}$ for unpromoted and $CsNO_3$ promoted so-called Raney ruthenium, respectively. The reaction conditions were 315°C and p_{N_2} of 0.2 bar. Raney Ru is an alloy of Ru-Al, where in this case the Al content was about 10 wt%. Based on hydrogen adsorption on the unpromoted catalyst, a site specific IER (i.e. TOF-IER) was estimated to 2.2 and $187 \times 10^{-4}\,s^{-1}$, for the unpromoted and promoted catalyst, respectively. The reaction order of the IER with respect to p_{N_2} was found to be 0.42 at 290°C for the latter. As function of H_2 pressure, the IER decreased, likely due to competitive adsorption. Even though promoted Raney Ru catalysts might show very high per gram IER activities, the Ru content is also very high. Thus, because of the high cost of Ru, such catalysts are not suitable for industrial applications.

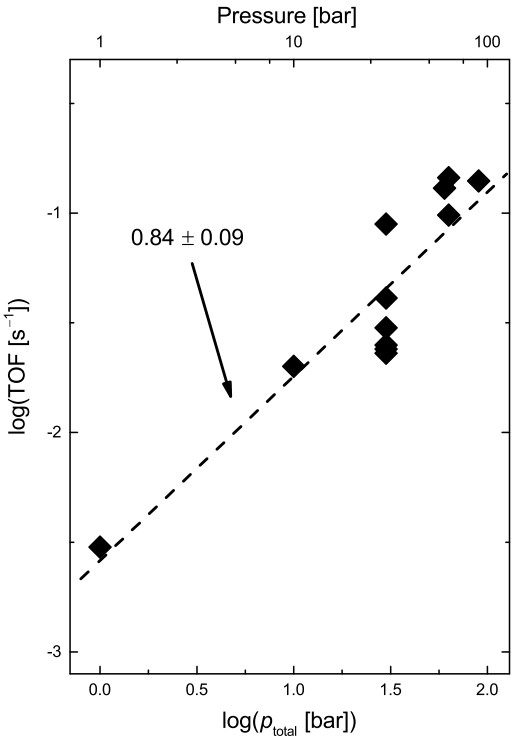

Figure 3.6: Total reaction pressure dependency of the literature TOFs at 400°C presented in Table 3.1. The slope represents the reaction order with respect total pressure (Eq. 2.5).

Ogata et al. [60] also investigated similar Raney Ru catalysts, as well as supported K promoted ruthenium. Unpromoted and K-promoted Raney Ru showed higher activity and TOF-IER than reported by Ref. [59]. Compared to K-promoted Raney Ru, all the supported K promoted Ru catalysts (5%Ru-K on AC, BeO, MgO, and 4.2%Ru-K on CaO) showed lower activities and TOF-IERs. The activation energies of the catalysts in both studies [59, 60] were similar and in range 92–109 kJmol^{-1}. Of the supported catalysts, 5%Ru-K/BeO showed the highest TOF-IER and an activation energy of 100 kJmol^{-1}. The TOF-IER of 5%Ru-K/AC was about 7 times lower, however, the activation energy was also the lowest of all the supported catalysts, at 96 kJmol^{-1}.

Hinrichsen et al. [61] investigated the activity of Ru/Al_2O_3, Ru/MgO and Ru-Cs/MgO by means of temperature-programmed-adsorption (TPA) and desorption (TPD), and the IE reaction. Since the IE reaction is dependent on adsorption and desorption, both rate constants are contained in the IER. Moreover, since the activation energy of dissociation is significantly smaller than of association, the kinetics of the IE reaction reflects associative desorption [61]. Thus, in combination with TPD, the rate constant of adsorption can be determined. A general finding was that Ru-Cs/MgO is

much more active towards nitrogen activation than both the unpromoted Ru/MgO, and even more so $RuAl_2O_3$. Based on all three techniques, the energy barriers of dissociative adsorption and associative desorption on Ru-Cs/MgO were determined to 33 and 137 $kJmol^{-1}$, respectively.

A nearly identical activation energy for isotope exchange on Ru-Cs/MgO at 139 $kJmol^{-1}$ was reported Kitano et al. [62]. This is 40 $kJmol^{-1}$ higher than the activation energy of NH_3 synthesis at 99 $kJmol^{-1}$. The temperature range was 340–400°C and pressure 0.267 bar. On a $Ca_{12}Al_7O_{33}$-electride supported Ru catalyst, the activation energies of NH_3 synthesis and nitrogen isotope exchange were 49 and 59 $kJmol^{-1}$, respectively. A 64 $kJmol^{-1}$ barrier of nitrogen desorption has been reported from TPD [63]. The lower barriers are suggested as much due to the electride-support significantly enhancing back-donation of electrons to the N_2 $2\pi^*$ antibonding orbital for dissociation, and electron transfer to the antibonding orbital of the Ru-N bond for association [63].

Since the activation energy from the isotope exchange reaction and temperature-programmed-desorption is close to identical, as seen for both Ru-Cs/MgO and Ru/C12A7:e^-, the rate determining step of isotope exchange is suggested to be associative desorption [62].

4 Experimental Methods

4.1 Sample preparation

Commercially available Ru/AC (5 wt% Ru basis on activated charcoal, Sigma-Aldrich) powder was promoted with barium through a wet impregnation route. A volumetric amount of a 0.5 M $Ba(NO_3)_2$ (Alfa Aesar, 99.95 %) solution, corresponding to a 1:1 mol ratio of Ba/Ru, was added to a sample of unpromoted Ru/AC. Until addition, the solution was heated at 85°C to maintain complete dissolution of $Ba(NO_3)_2$. An additional amount of deionized water (∼30 vol%) was added to the slurry of promoter solution and catalyst powder to improve the ease of mixing. The slurry was heated at 80°C under stirring (200 RPM) for 17 hours, before dried in a heating cabinet at 120°C for about 1 hour, following 5 hours at 50°C. The $Ba(NO_3)_2$ impregnated Ru/AC powder was then calcined under continuous evacuation at 550°C for 3 hours, with heating rate of 50°C per hour.

4.2 Sample characterization

4.2.1 Scanning electron microscopy (SEM)

The morphology of the powders was investigated by SEM, and EDS (Energy Dispersive X-Ray Spectroscopy) was utilized in order to estimate the apparent Ru/Ba ratio. The instrument used was a Hitachi TM3000 Tabletop Microscope.

4.2.2 Transmission electron microscopy (TEM)

The catalyst microstructure, including Ru particle size, Ba dispersion and the apparent Ru/Ba ratio, was investigated by TEM and EDS, using a JEOL 2000FX microscope with a NORAN System SIX EDS detector. The TEM sample was prepared by dispersing catalyst particles on a holey carbon film.

4.2.3 N_2 adsorption - BET

The Brunauer-Emmett-Teller (BET) specific surface area, pore volume and pore size was determined from N_2 adsorption measured using a routine sorption apparatus (BELSORP-MINI). Prior to the measurement of the powder sample, a pre-treatment

at 80°C for 1 hour then 300°C for 3 hours was performed in to remove absorbed species, such as water, from pores and surface.

4.3 Isotope exchange by gas-phase analysis with mass spectrometry

4.3.1 Instrumental setup

The apparatus used in the isotope exchange (IE) measurements is built up by four main parts: a quartz glass tube working as a reaction chamber, a quadrupole MS (QMS, Prisma Plus 220, Pfeiffer-Vacuum), a gas handling system including a pressure monitored gas-mixing chamber, and a tubular furnace. A schematic is shown in Fig. 4.1.

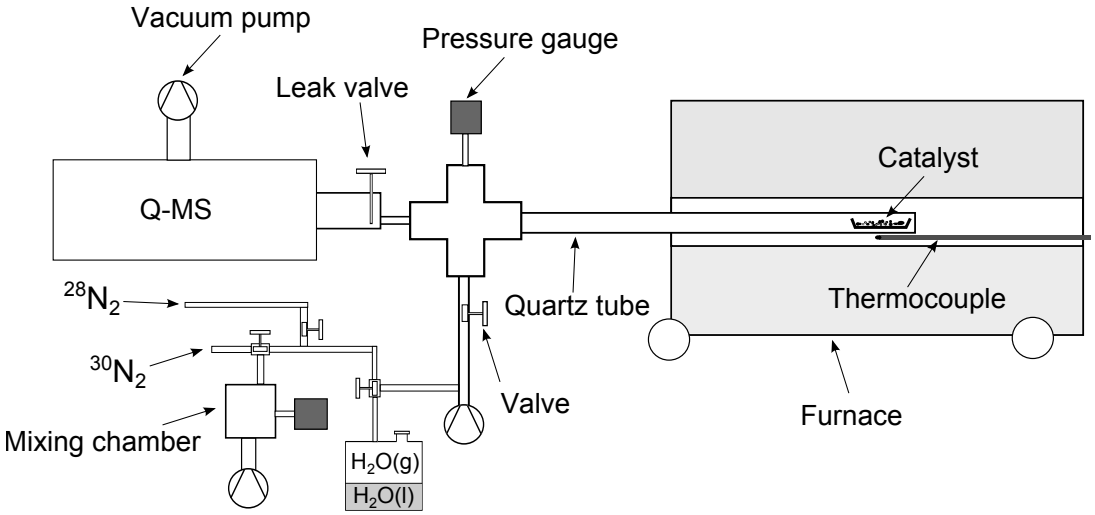

Figure 4.1: A schematic of the instrumentation used in the isotope exchange measurements.

The reaction chamber reaches half way into the furnace where the temperature is monitored with an S-type thermocouple (Pt/Pt90Rh10). At this position—inside the reaction chamber—a quartz boat containing powdered catalyst sample is positioned. The temperature of the catalyst and the surrounding gas is assumed to be the temperature of the furnace, and the reaction chamber pressure is monitored by a pressure-gauge (Compact capacitance gauge, Pfeiffer Vacuum) close to the MS-inlet. A small amount of gas enters the MS through a leak valve due to under-pressure created by a turbopump and membrane pump. At the very entrance (see leak valve in Fig. 4.1), a fraction of the gas phase molecules are ionized by open ion source yttria filaments, and separated by the quadupole mass filter according to the mass over charge ratio (m/z) before reaching the detector. The pressure inside the MS when operating

is commonly around 6×10^{-8} mbar, and since the MS gas consumption is minor, the reaction chamber pressure is assumed constant.

The QMS is equipped with two detectors, continuous secondary electron multiplier (C-SEM) and Faraday, where the detection limits are 5×10^{-12} and 1×10^{-14} mbar, respectively. In all experiments the former was utilized allowing for a higher signal-to-noise ratio while measuring small ion currents. The contribution from each mass signal to adjacent masses are less than 10 ppm.

4.3.2 Activity measurements

Prior to each experiment, the reaction chamber was evacuated down to a pressure of less than 0.1 mbar. In cases where the temperature was changed in between measurements, the reaction chamber containing catalyst was held under evacuation for about one hour after the measurement temperature was reached. This was in order to reduce the amount of adsorbed species, such as H_2O, on the catalyst and quartz tube, as well allowing the sample temperature to stabilize. A gas mixture (usually close to 1:1) of $^{28}N_2$ and $^{30}N_2$ (Sigma-Aldrich, 98 atom % ^{15}N) was prepared in the gas-mixing chamber at pressures ranging from 1–500 mbar, before introducing a given amount to the reaction chamber. The composition of the gas phase was continuously monitored as function of time by the MS. Most experiments were performed at a pressure of 50 mbar and with around 50 mg of catalyst sample. Deviations from this are specified in the result section, and when relevant.

In experiments where the influence of a secondary gas (e.g. H_2O) on the catalyst activity was investigated, a given amount the secondary gas was introduced to the reaction chamber prior to introducing the isotope mixture. Introduction of water vapor was done using the setup illustrated in Fig. 4.1. A chamber containing deionized water held at room temperature was attached to the gas handling system, allowing for evacuation of the gas phase. After evacuation, the gas phase should only be water vapor at a pressure determined by the vapor pressure. Compared to the evacuated reaction chamber the water chamber is at over pressure, and a given amount can therefore be introduced by connecting the two.

4.3.3 Data analysis

The raw data output from the MS is in the form of ion currents (IC) of the traced m/z values (Table 4.1). The signals of ^{14}N and ^{15}N give information about the isotope ratio and potential leaks into the reaction chamber. The signal of the former can also be used to identify an increase in $m/z = 28$ as due to nitrogen or carbon monoxide.

As explained in section 2.3 the IE reaction can be described by Eq. 2.26. To extract

Table 4.1: List of the usually traced values in the experiments.

m/z	Plausible origin species
14	^{14}N
15	^{15}N
28	$^{28}N_2$, CO
29	$^{29}N_2$
30	$^{30}N_2$
2	H_2
18	H_2O
32	O_2
44	CO_2

the isotope exchange rate (IER), several terms have to be determined. How the reaction temperature and reaction chamber volume are determined is treated in the next subsection.

The relative intensity I_n of each molecular nitrogen species n is taken as the IC of the given species divided by the total molecular nitrogen IC:

$$I_n = \frac{IC(n)}{IC(28) + IC(29) + IC(30)} \tag{4.1}$$

And similarly for an atomic nitrogen species m:

$$I_m = \frac{IC(m)}{IC(14) + IC(15)} \tag{4.2}$$

The relative intensities of the molecules are assumed to be directly reflected by the relative abundance of the same species in gas phase, i.e. $I_n = p_n/p^{\mathrm{tot}}_{\mathrm{N}_2}$. The same is true for the relative isotope abundance in gas phase and the relative atomic intensities. To calculate the relative molecular intensities at statistical equilibrium I_∞, the relative isotope abundances at $t = 0$ have to be determined. This can be done by three approaches. Firstly, I_∞ can be calculated directly from I_{14} and I_{15} at $t = 0$ (section 2.3). Secondly, it can be calculated by determining the relative isotope abundance from relative molecular intensities at $t = 0$:

$$^{14}\mathrm{N}_{\mathrm{rel}} = I_{28} + \frac{1}{2} I_{29} \tag{4.3}$$

$$^{15}\mathrm{N}_{\mathrm{rel}} = I_{30} + \frac{1}{2} I_{29} \tag{4.4}$$

And thirdly, relative isotope abundance can be taken as the average of the above approaches. In principle, the first and the second should give the same values for the isotope abundance. However, the ICs used in the first approach and $IC(29)$ used in the second are rather low. In some cases where the overall IC is especially low,

fluctuations in the signal may affect the accuracy of the values. Since it is difficult to determine which of the two gives the correct value, the third approach has been used in this work. Nevertheless, the magnitude of the difference between the first and second approach is 10^{-2} %, which is an insignificant uncertainty when determining the IER.

As explained in section 2.3 the isotope exchange rate (IER) can be found by fitting either of the equations 2.26 and 2.27. However, if for example the number of active sites changes during an experiment—e.g. due to competitive adsorption—the apparent IER may also change. This leads to Eq. 2.27 becoming non-linear. In such cases the IER can be extracted numerically by performing multiple linear fits in relatively short intervals of time, and taking the slope as the IER in the middle time interval; e.g., the slope in interval 0–2 hours is the IER at 1 hour. When the interval approaches zero the numerical solution converges toward the derivative of Eq. 2.27. Figure 4.2 shows the numerical solution at three different fit intervals. The resolution of the

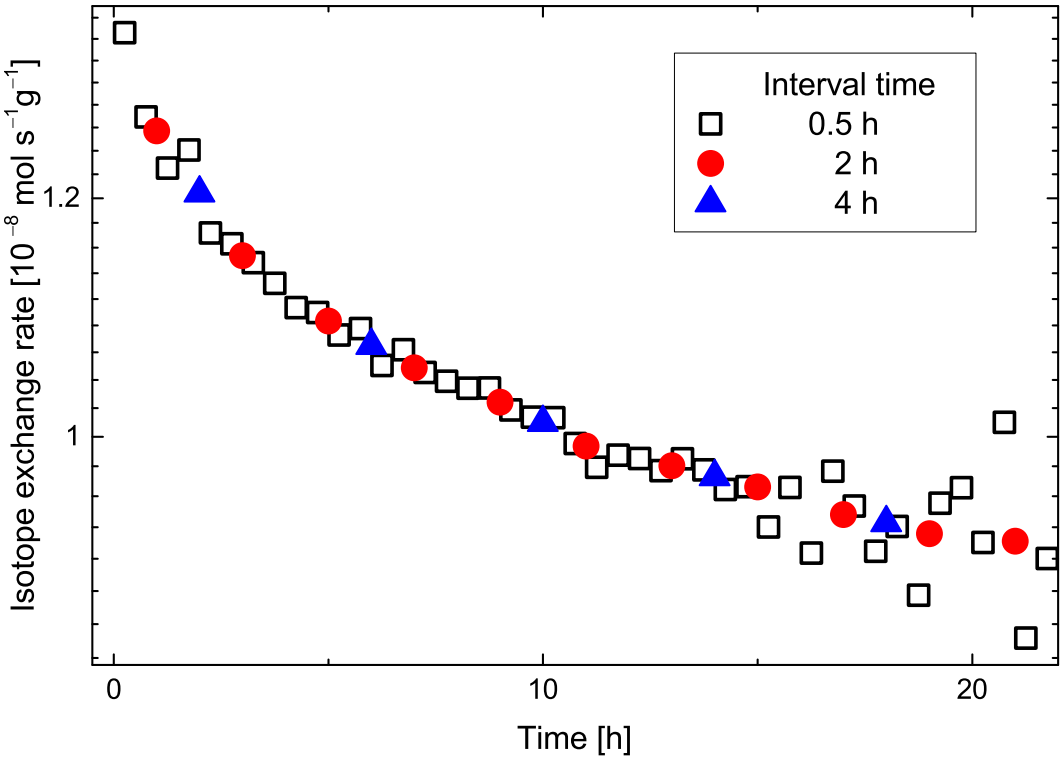

Figure 4.2: Illustration of how changes in fit interval time affects the numerically determined the IER. The measurement shown was conducted at 550°C.

IER increases with decreasing interval, however, the resolution achieved by all three intervals seems to sufficiently describe the IER. Because of noise in the ion currents,

short time intervals are prone to numerical errors. This is especially true when the IER is changing more slowly, as seen after about 15 hours into the measurement when the interval time is 0.5 hours (Fig. 4.2). In order to get a well resolved IER without large numerical errors, as well as being consistent with the method of analysis, an interval time of 2 hours was chosen for further measurements.

4.3.4 Additional sources of error and uncertainty in IE measurements

The reaction chamber is built up by two parts: a silica tube, and a 4-way cross attached to the MS, a pressure-gauge and the gas handling system. The volume of the silica tubes were estimated using water, and the volume of the 4-way fitting was estimated from the dimensions of the cylindrical parts. The uncertainty lies mainly in the estimation of the latter. If an incorrect volume is used when analyzing the data, a systematic error is introduced shifting the IER up or down by a factor of V_{true}/V.

As explained in section 4.3.1, the temperature of the reaction chamber—and catalyst—is taken as the temperature in the middle of the tubular furnace. Since it is not measured inside the reaction chamber, the true reaction chamber temperature might be slightly lower.

5 Computational Methods

5.1 Vienna Ab initio simulation package

All computations in this work were performed using the Vienna Ab initio Simulation Package (VASP), which iteratively solves the Kohn-Sham equations (section 2.4.2).

In a condensed phase, the number of electrons and atoms is huge, and in order to compute physical properties of such a system, a large number of calculations must be performed. As most periodic DFT packages do, VASP overcomes this problem by simulating the system with periodic boundary conditions. In this case, the wave function of the periodic system can be described as a Bloch wave, which is a product of a plane wave and a function with the same periodicity as the cell:

$$\Psi_{\boldsymbol{k}}(\boldsymbol{r}) = u_{\boldsymbol{k}}(r)\mathrm{e}^{i\boldsymbol{k}\cdot\boldsymbol{r}} \tag{5.1}$$

Here $u_{\boldsymbol{k}}(\boldsymbol{r})$ is called the periodic Bloch part, $\mathrm{e}^{i\boldsymbol{k}\cdot\boldsymbol{r}}$ is a plane wave, and $\boldsymbol{r}$ and $\boldsymbol{k}$ are continuous position vectors in real and reciprocal space, respectively. The Bloch part can be expanded in terms of a special set of plane waves [11],

$$u_{\boldsymbol{k}}(\boldsymbol{r}) = \sum_{\boldsymbol{G}} c_{\boldsymbol{G}}\mathrm{e}^{i\boldsymbol{G}\cdot\boldsymbol{r}} \tag{5.2}$$

which further leads to

$$\Psi_{\boldsymbol{k}}(\mathbf{r}) = \sum_{\boldsymbol{G}} c_{\boldsymbol{k}+\boldsymbol{G}}\mathrm{e}^{i(\boldsymbol{k}+\boldsymbol{G})\cdot\boldsymbol{r}} \tag{5.3}$$

where $\boldsymbol{G}$ is a set of all reciprocal lattice vectors. Thus, evaluating the equation at a single $\boldsymbol{k}$-point requires a summation over an infinite number of $\boldsymbol{G}$-values. This is a numerical problem which is approached in two ways. Firstly, since close $\boldsymbol{k}$-points give rather similar wave functions—and hence similar energies—only a finite number of sampling points is needed to properly describe the system. This number is dependent on the size and nature of the system; metals generally require a larger number of $\boldsymbol{k}$-points [11]. Secondly, Eq. 5.3 are solutions to the KS-equation (Eq.2.33) with kinetic energy

$$E = \frac{\hbar^2}{2m_{\mathrm{e}}}|\boldsymbol{k}+\boldsymbol{G}|^2 \tag{5.4}$$

Solutions with lower kinetic energies are generally considered to be more physically

important than solutions with very high, and included values of $\boldsymbol{G}$ are thus restricted to those yielding solutions with kinetic energy less than [11, 64]

$$E_{\text{cut}} = \frac{\hbar^2}{2m_{\text{e}}} G_{\text{cut}}^2 \tag{5.5}$$

which is referred to as the *cutoff-energy*. Equation 5.3 now only requires summation over a finite number of $\boldsymbol{G}$-values. Both the number of $\boldsymbol{k}$-points and the cutoff-energy are central parameters in DFT calculations, and how these are chosen is treated in section 5.4.

In VASP, the interaction between electrons and ions can either be described by pseudopotentials, or the Projector-Augumented-Wave (PAW) method. Both of which are so-called *frozen core* approaches. In such approaches, the computational effort is reduced by utilizing in different ways the fact that the physical properties of a system are largely determined by the valence electrons. In many cases the two give very similar results, as well as being in good agreement with methods without a frozen core [11]. In this work, the PAW method [65][66] is used.

5.1.1 Approximations to the exchange-correlation functional

Different versions of LDA, GGA and meta-GGA are implemented in VASP as approximations to the exchange-correlation functional (XC) (section 2.4.3). In the LDA, the XC potential is approximated to that of an uniform electron gas, with equal density as the local electron density of the system. GGA and meta-GGA are based on the LDA, but also include the electron density gradient, and its Laplacian (meta-GGA). Hybrid functionals, such as Heyd-Scuseria-Ernzerhof (HSE) [67], describe the XC potential as a combination of the Hartree-Fock exchange energy and a GGA functional [11]. Such approximations are successful in describing molecular properties, however, properties of condensed phases in the limit of uniform density (section 2.4.3) are less accurate [68, 69]. In this work, the Perdew-Burke-Ernzerhof exchange-correlation functional (GGA-PBE) [70], is used.

5.2 Surface modeling

A surface is modeled by terminating the periodic structure in one direction after a given number of atomic layers, leaving a portion of empty space above the top layer (Fig. 5.1). Due to periodicity of the cell, this creates a slab of atoms where two surfaces are exposed, which is repeated in space after a distance of empty space. The empty space is referred to as the *vacuum layer*. In the two other directions the surface is

infinite.

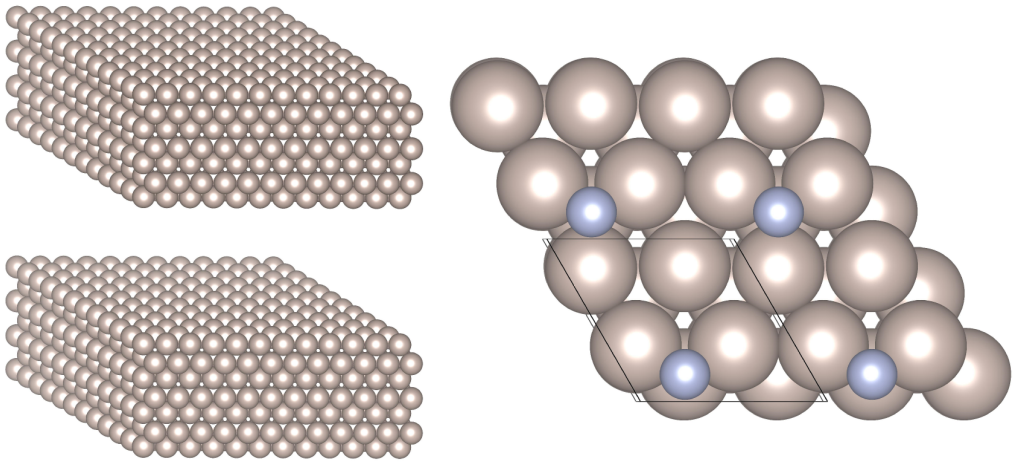

Figure 5.1: View of a seven-layer slab model of Ru(0001), repeated two times in z-direction (left), and of a 2×2 model with adsorbed atomic nitrogen, repeated 4 times in x and y-direction (right). The black lines indicate the boundary of the repeating unit cell.

Usually, 5 or more layers of atoms and a vacuum layer thickness of more than 10 Å, are used. However, this is dependent on factors such as the nature of the material and potential adsorbates. How these parameters are chosen is treated in section 5.4.

In this work, an asymmetric slab model is used. Here a few of the bottom atom layers are locked to the bulk positions while the others are allowed to structurally relax. This approach better mimics a real surface where the structure may gradually change with the distance from the surface into the material, until equal to that of bulk.

Since the slab is repeated periodically in each direction, so are the adsorbates. The size of the repeating unit cell in x and y-direction (i.e. the number of atoms in each direction) can be varied in order to model adsorbates at different surface coverages. For example, if two Ru bulk unit cells (i.e hcp with two atoms) are used in both directions (referred to as a 2×2 slab), a surface having 4 atoms in each layer is obtained. This is illustrated in Fig. 5.1 where atomic nitrogen is adsorbed at a coverage of 1/4 monolayer (ML). In an asymmetric slab model, adsorbates are only modeled on the relaxed surface. Several flat Ru(0001) surfaces of different xy-sizes were used to model a different surface coverage.

A stepped Ru surface was modeled by removing a given number of rows of the top layer of the slab, exposing atoms of the second top layer. In this case a 4×6 slab was used to achieve the desired periodicity. All slabs were of seven atom layers, where the positions of the first three were fixed. The vacuum layer thickness was 17 Å.

Gas phase molecules were modeled as a single unit in an otherwise empty $10 \times 10 \times 10\,\text{Å}$ unit cell.

5.2.1 Adsorption energy

The adsorption energy is important describing the stability of the adsorbed species compared gas phase molecules, and is calculated according to

$$E_{\text{ads}} = E_{\text{slab}+n\text{N}} - (E_{\text{clean slab}} - \frac{n}{2}E_{\text{N}_2(\text{g})}) \tag{5.6}$$

Here $E_{\text{slab}+n\text{N}}$ is the total energy of the slab cell with n nitrogen atoms, $E_{\text{clean slab}}$ is the total energy of the clean slab cell (i.e. without adsorbate), and $E_{\text{N}_2(\text{g})}$ is the energy of single isolated N_2 molecule. The adsorption energy is here in units of energy per n nitrogen atoms. However, for easier comparison between different systems, this number is in the rest of the text multiplied with $2/n$ to be expressed as energy per molecule, unless otherwise noted.

5.2.2 Adsorption entropy

As mentioned in section 2.5 the total energy from DFT is solely the electronic contribution to the energy, and to include the effects of temperature, the entropy change of the adsorption reaction must be calculated. Following the assumptions made in section 2.5.1, this can be estimated from the coverage dependent configurational entropy (Eq. 2.43) and the vibrational entropy (Eq. 2.42) of the adsorbates, where only the vibrational frequencies of the latter is calculated using VASP.

Following the harmonic approximation, VASP calculates vibrational frequencies from the second derivative of the systems total energy with respect to the positions of the adsorbed atoms as they are individually slightly displaced (e.g. 0.025 Å) in the direction of each Cartesian coordinate [11, 12].

5.3 Nudged elastic band method

The nudged elastic band (NEB) method is a tool for finding minimum energy paths (MEP) and saddle points between two known local structural minima, in processes such as atomic diffusion or molecular dissociation on a surface. In this method a series of equally spaced intermediate states, called images, forming a band between the minima, are energetically optimized. This is done by adding a spring force between the images along the band, and minimizing the force due to the potential perpendicular to the band. When the latter is zero, the images are at the MEP. However, since the

images are restricted to be equally spaced the exact saddle point (i.e. transition state (TS)) is not automatically found. To find the TS, an image has to be positioned at that exact position along the band.

Both the TS and the MEP can however be found automatically by using the climbing image nudged elastic band method (cNEB), developed by Henkelman et al. [71]. In this method the image of highest energy does not feel the spring force, but the true tangent force of the image is instead inverted. This results in the image maximizing its energy along the band, and hence travels up to the saddle point.
In this work, all minimum energy paths and transition states are found using the cNEB method.

5.4 Convergence and calculation parameters

The total energy of a system changes with number of $\boldsymbol{k}$-points, and the cutoff-energy. However, it usually converges when the parameters are increased to a certain value. To find the appropriate parameters, the convergence of the energy with respect to the number of $\boldsymbol{k}$-points and cutoff-energy, was investigated.

Tests of the convergence with respect to the $\boldsymbol{k}$-points, were performed for bulk ruthenium, using the standard energy cutoff specified in the potential. Since generally the density of $\boldsymbol{k}$-points should be equal in all directions, the energy was computed using 5–25 $\boldsymbol{k}$-points in x and y-direction and a value resulting in a corresponding $\boldsymbol{k}$-point density (points per Å^{-1}) in the z-direction. Figure 5.2 shows the convergence results.

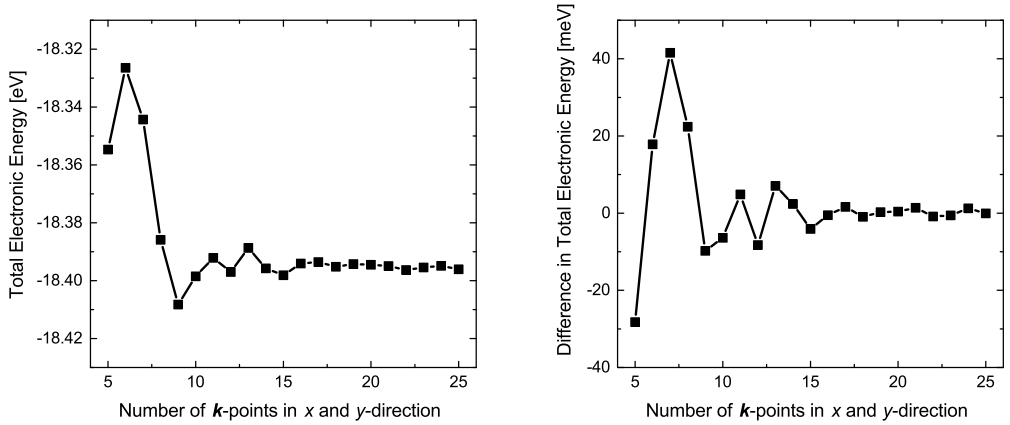

(a) Total electronic energy vs. number of $\boldsymbol{k}$-points in x and y-direction.

(b) Difference in total electronic energy between the data points in (a).

Figure 5.2: Results from convergence test with respect to the number of $\boldsymbol{k}$-points.

The total electronic energy was well converged within 2 meV per change in $\boldsymbol{k}$-points, when 16 $\boldsymbol{k}$-points were used in x and y-direction, and 9 in z-direction (i.e. a (16×16×9)-mesh). This corresponds to a $\boldsymbol{k}$-point density of approximately 6 points/Å^{-1}. In all subsequent calculations, $\boldsymbol{k}$-point meshes giving the same density was used. In the slab models, one $\boldsymbol{k}$-point is used in the z-direction normal to the surface.
Similar convergence tests were performed for the cutoff-energy. The total electronic energy of bulk Ru was calculated using cutoff-energies in range 250–700 eV (50 eV increments). A $\boldsymbol{k}$-mesh of (16 × 16 × 9) was used. Convergence was achieved within

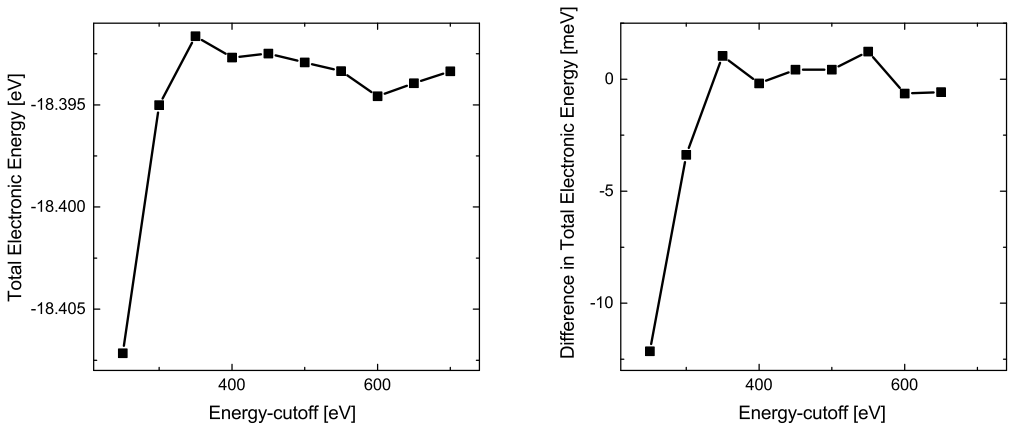

(a) Total electronic energy vs. energy-cutoff.

(b) Difference in total electronic energy between the data points in (a).

Figure 5.3: Results from convergence test with respect to energy-cutoff.

2 meV change per change in energy-cutoff, at 400 eV. Hence, this was used as energy-cutoff in all subsequent calculations.

To ensure that the distance between each slab as well as the number of layers were large enough for the surface to be treated as isolated, convergence of the surface energy with respect to vacuum layer thickness was checked for slabs with 2–12 layers. The vacuum layer thickness was varied from 2–22 Å in 2 Å increments.

The surface energy E_{surf} of a material describes the energy required to cleave a bulk structure, exposing a surface. This was calculated according to

$$E_{\text{surf}} = \frac{1}{2A}(E_{\text{slab}} - \frac{n}{m}E_{\text{bulk}}) \tag{5.7}$$

where A is the area of each surface, E_{slab} is the energy of the slab cell with n atoms and E_{bulk} is the energy of the bulk unit cell of m atoms. Convergence of the surface energy with respect to vacuum layer thickness was well converged within 0.1 meV per 2 Å change in vacuum layer thickness, already at 8 Å, for all slabs. However, this value is rather low and the computational effort of calculating E_{surf} of a clean slab was not

markedly increased by larger vacuum layer. Therefore, to make sure the slabs were well separated, the vacuum layer thickness used in further calculations was increased to 16 Å. When an adsorbate was added, this was further increased by 1 Å.

In Fig. 5.4, the surface energy is plotted as function of layers in the slab. The general

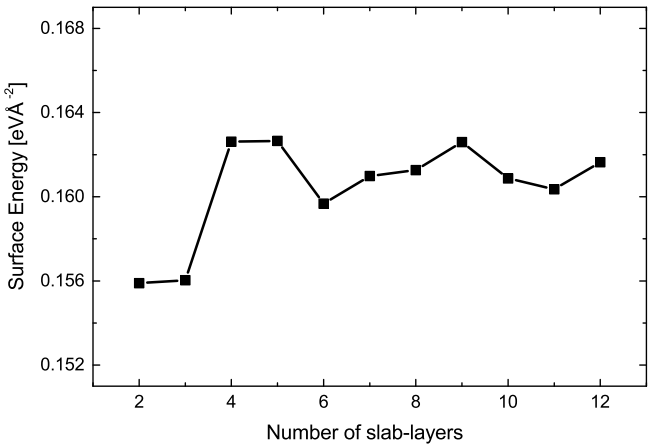

Figure 5.4: Results from convergence test of the surface energy with respect to number of slab-layers.

trend seems to be that the surface energy increases considerably when the number of layers increase from 3 to 4, before slightly stabilizing at larger numbers. Nevertheless, the change in surface energy per change in number of layers is rather small. Thus, the surface energy is converged fairly well at four layers. Seven layers were used in further calculations since this was somewhat more in line with the values at higher numbers of layers, and to ensure properly isolated potential adsorbates.

A summary of some key parameters is listed in Table 5.1

Table 5.1: Key parameters used in the calculations.

Parameters	
Potential	PAW
Exchange correlation functional	GGA-PBE
$\boldsymbol{k}$-point density	≈ 6 per Å^{-1}
Energy-cutoff	400 eV
Energy convergence criterion	10^{-5} eV
Force convergence criterion	0.02 eVÅ^{-1}

5.5 Accuracy and sources of error

The accuracy of a calculation can essentially be divided into numerical and physical accuracy. The former describes how well different aspects of the numerical solution are converged and the latter addresses the predictive power of the calculations, i.e, the agreement between calculated and true physical properties.

One aspect of numerical accuracy is how well the numerical approximation to the infinite-dimensional Bloch wave (5.3) is converged with respect to the number of $\boldsymbol{k}$-points and energy-cutoff. Or in other words, how close the numerical solution is to the analytical. Another regards how well the energy—or more conveniently the forces on the ions—is converged with respect to ion positions. If the force convergence criterion is too high, the relaxed positions may in fact be relatively far away from the true local minima, which further results in an incorrect minimum energy. A general note on energy minima found from calculations is that they can only be described as local, not global, since there is no way of to distinguishing the two. The numerical accuracy, or rather the numerical uncertainty, of both the above properties will potentially be sources of error in the physical accuracy of the calculations. However, compared to the uncertainty due to the slab model, i.e., number of layers, and even more so, to the exchange-correlation functional, this contribution will be minor.

Adsorption energies and bond strengths are generally overestimated by the various GGA functionals [11]. The adsorption energy of NO and CO in late transition metals has for instance been shown to be overestimated by approximately 0.5 eV per adsorbate [72].

The systematic overestimation of adsorption energies can to some extent be explained by comparison of chemically dissimilar states, i.e., "gas phase" molecule and on a solid surface [11]. Even though the absolute values may be off, relative energies between chemically similar systems are easier to predict and should therefore be more physically accurate. If for example the relative stability of adsorption at different sites are compared, the gas phase molecule can be neglected. Another example is the activation barrier of dissociative adsorption.

6 Experimental Results

6.1 Sample characterization

6.1.1 SEM

Three powder catalyst samples of the nominal composition from three different batches (A, B and C) which have been at different maximum temperatures (550, 700 and 750°C) were characterized. Batch A was used in all measurements of the isotope exchange rate (IER) except for the pressure dependency at 700°C (section 6.2.2) and high temperature deactivation (section 6.2.4), where the samples were from batch C. The activity of B was only briefly measured and is not included in the results.

In both sample A and B, agglomerates almost completely covered with a barium-rich compound were observed (Fig. 6.1). In sample C this was not observed to the same extent. The Ba/Ru ratio was estimated from EDS quantification at 10, 8 and 7 different areas in A, B and C, respectively. Areas where the surface was clearly covered with barium, as shown in Fig. 6.1, were avoided. The ratio was estimated to 1.6 ± 0.9 in A, 2.7 ± 1.1 in B, and 3.1 ± 1.5 in C. From the large uncertainties it is evident that the Ba:Ru ratio of the catalyst varies considerably with each batch.

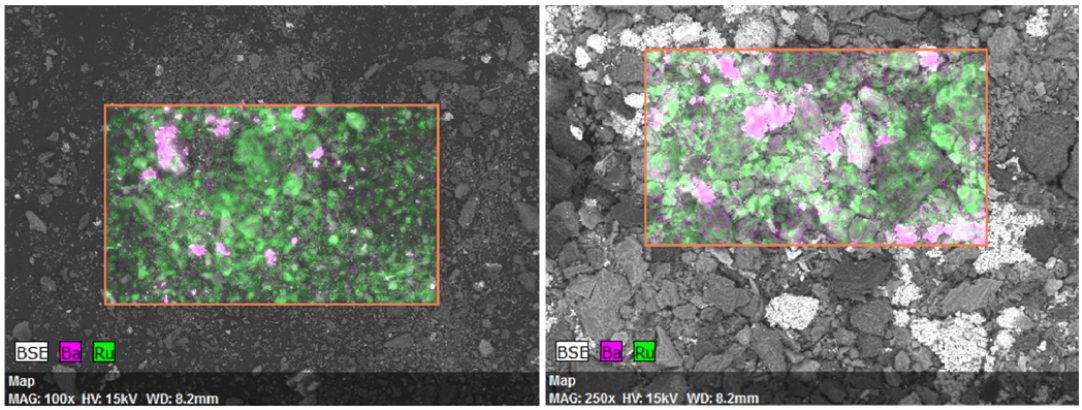

Figure 6.1: SEM image including EDS map of sample A and B, showing agglomeration of a Ba-rich compound.

6.1.2 TEM

The three samples investigated by SEM (A, B and C) were also characterized using TEM. Sample A was investigated two times; the first time a large amount of Zn was found in the sample, however, in the second measurement, when the TEM sample was prepared more carefully, Zn was not found. Hence, the presence of Zn was presumably due to the method of preparation prior to TEM analysis. The Ba/Ru ratio was quantified from several EDS maps at different magnifications. Ratios of 2.3, 0.87, 1.4 and 1.9 were found in the Zn contaminated sample, and 0.39 and 0.43 were found in the other. This is suggests that the ratio is varying locally in the sample. The average ratio is 1.2 ± 0.8. However, the number of EDS measurements is low and several more measurements are needed to estimate this with certainty.

Figure 6.2 shows STEM images of sample B and where the spot EDS analysis was performed. The smaller Ba/Ru ratio when more of the larger white particles are present indicate that these are Ru. Based on both images, the Ru particles seem to be less than 10 nm in diameter. However, this is a rough estimate only based on this specific area of the catalyst. Some larger particles around 20 nm were observed in other areas.

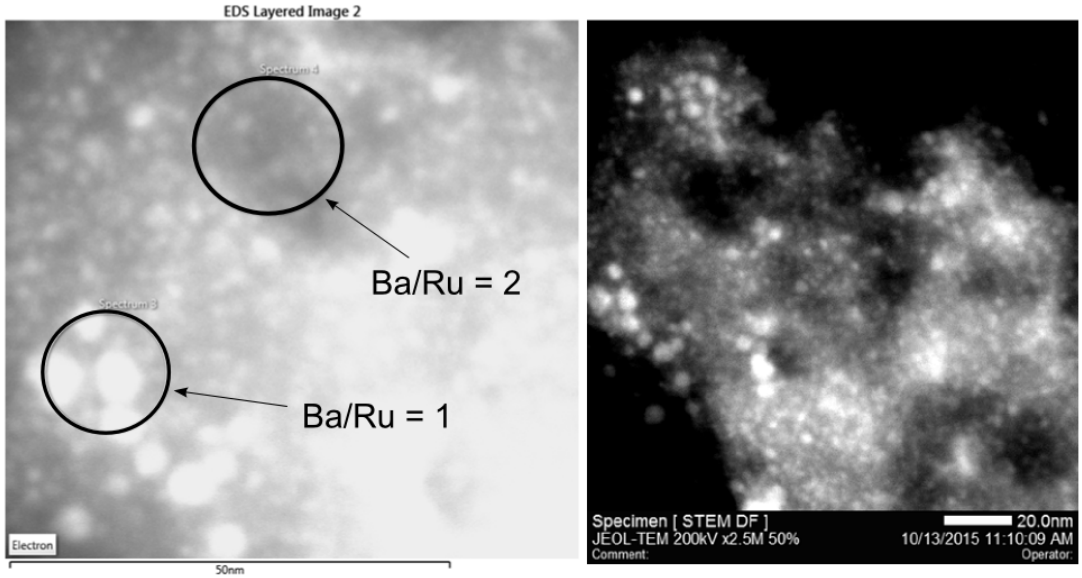

Figure 6.2: STEM images of sample B where the black circles indicate areas of spot EDS analysis.

Spot EDS analysis on sample C showed Ba/Ru ratios of 0.77 and 5.3 at the Ru particles and in between, respectively, while the entire map showed a ratio of 2.57 (Fig. 6.3). In another area (not shown), the same type of spot analysis showed 0.41

at the particles while no Ru was found in between. Based on the entire map, the ratio was 2.45. In this sample, the number of larger particles, some up to around 50 nm, seems to be higher as compared to sample B. However, it is possible that these "particles" are just clusters of smaller particles agglomerated together. To ascertain if the particles of sample C are generally larger, the sizes in several more areas of the catalyst have to be analyzed.

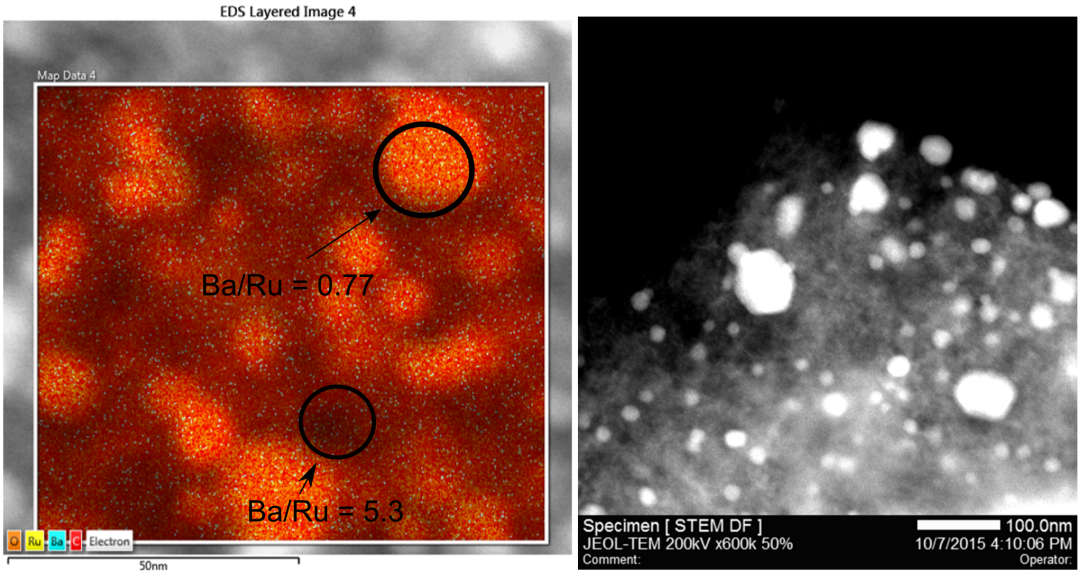

Figure 6.3: EDS map and STEM image of sample C. The black circles indicate areas of spot EDS analysis.

In general, based on all three samples, the Ba/Ru ratio varies locally with a rather large span of ratios from around 0.39 to around 5.3. The Ru particle size seems to be mostly smaller than around 10 nm in diameter, but particles up to around 50 nm are observed. To estimate both the Ba/Ru ratio and the Ru particle size with better accuracy, more areas have to be investigated.

6.1.3 N_2 adsorption - BET

The BET surface area, total pore volume and mean pore diameter were determined from N_2 adsorption for three powder catalyst samples from batch A, exposed to different maximum temperatures. The results are shown in Table 6.1. All samples show similar values regardless of maximum temperature.

Table 6.1: Results from the N_2 adsorption measurements.

Max temperature (°C)	Surface area (m^2g^{-1})	Total pore volume (cm^3g^{-1})	Mean pore diameter (nm)
550	626	0.57	3.7
650	647	0.59	3.6
750	635	0.56	3.5

6.2 Isotope exchange rate measurements (IER)

An illustrative example of the evolution of the gas phase with respect to nitrogen species is shown in Fig. 6.4, where the relative intensities of $^{28}N_2$, $^{28}N_2$, $^{29}N_2$ and $^{30}N_2$ are plotted as function of time at 600°C and $p_{N_2} = 50\,\text{mbar}$. The abundance of

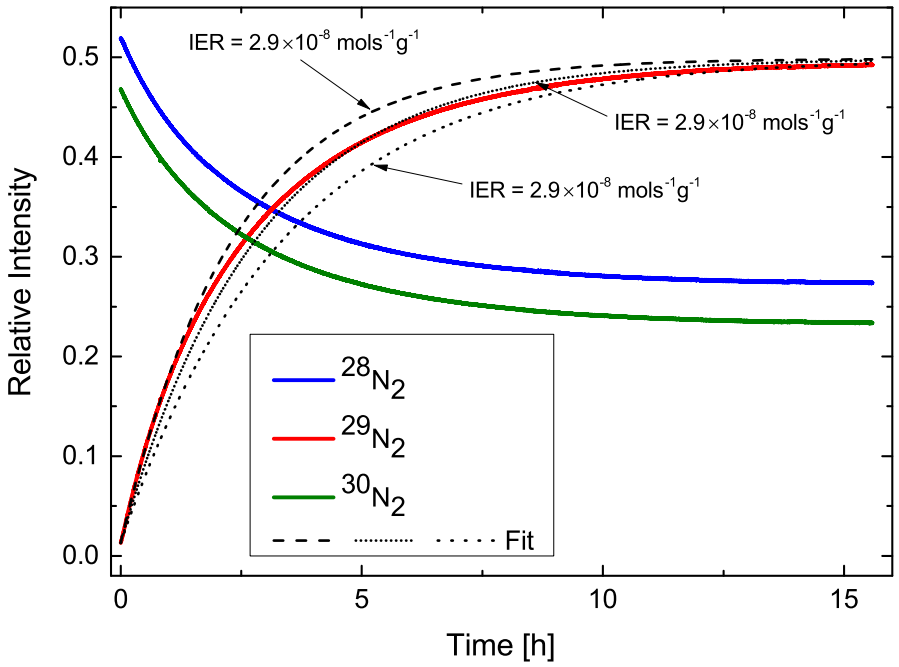

Figure 6.4: The relative intensity of the three N_2 species in the gas phase as function of time. The dashed and dotted lines represent the evolution of $^{29}N_2$ simulated from Eq. 2.26 at different IERs.

$^{28}N_2$ and $^{30}N_2$ decreases with time, while it increases for $^{29}N_2$, as expected if isotope exchange occurs. The dashed and dotted lines are simulated values from Eq. 2.26 of the relative intensity of $^{29}N_2$ for three different isotope exchange rates. The dashed line, simulated with IER of $2.9 \times 10^{-8}\,\text{mols}^{-1}\text{g}^{-1}$, correspond well with the measured values in the first few hours, but reaches statistical equilibrium too fast.

The close-dotted line, simulated with IER $= 2.4 \times 10^{-8}\,\text{mols}^{-1}\text{g}^{-1}$, gives too low intensity at first and slightly overshoots after 5 hours. An IER of $2.0 \times 10^{-8}\,\text{mols}^{-1}\text{g}^{-1}$

gives a reasonable fit only after 12 hours. This observation suggest that the ideal case described by Eq. 2.26 is not followed; i.e, the rate of exchange changes slightly, but still significantly, with time. In most of the measurements above 500°C and below 450°C, ideal behavior was not observed.

6.2.1 Temperature dependency of the IER

The IER measured at 50°C increments going down in temperature from 650°C to 450°C is plotted versus time in Fig. 6.5 for two subsequent series of measurements. The filled data-points represent the first measurement series (S1) and the open represent the second (S2). After S1, the catalyst was heated from 450–650°C under evacuation before S2 was initiated. Except for at 450°C, the two measurement series are in good agreement. At the higher temperatures, the IER decreases in a subsiding manner with

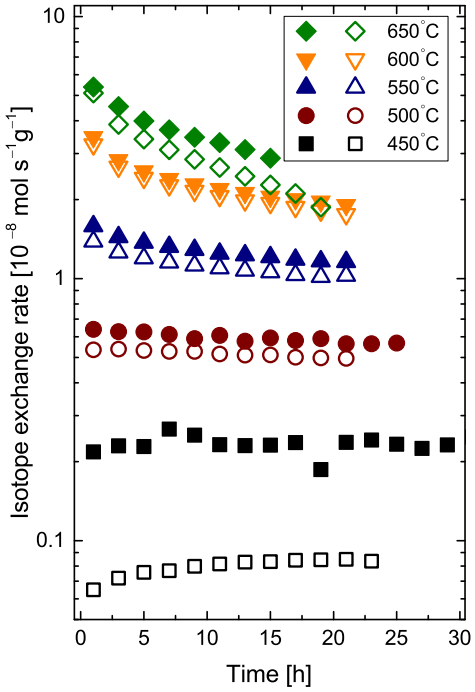

Figure 6.5: The isotope exchange rate (10^{-8}mols^{-1}g^{-1}) plotted as function of time for a set of different temperatures. The filled and open markers represent the first and the second measurements series, respectively

time throughout the measurement. The magnitude of the decrease diminishes when going down in temperature, and at 450 (S1) and 500°C (S2) the IER remains fairly constant. At 450°C (S2), the IER gradually increases with time and is in general about six times lower than in S1—which is a considerable difference compared to the other

temperature-couples.

Figure 6.6 shows Arrhenius-type plots of the S1 and S2 data, where the logarithm of the IER is plotted versus reciprocal temperature 1, 7 and 15 hours into the measurement. In Fig. 6.6a the open black circles correspond to values averaged of the IER in Fig. 6.5 for the cases where the IER was practically constant. An additional

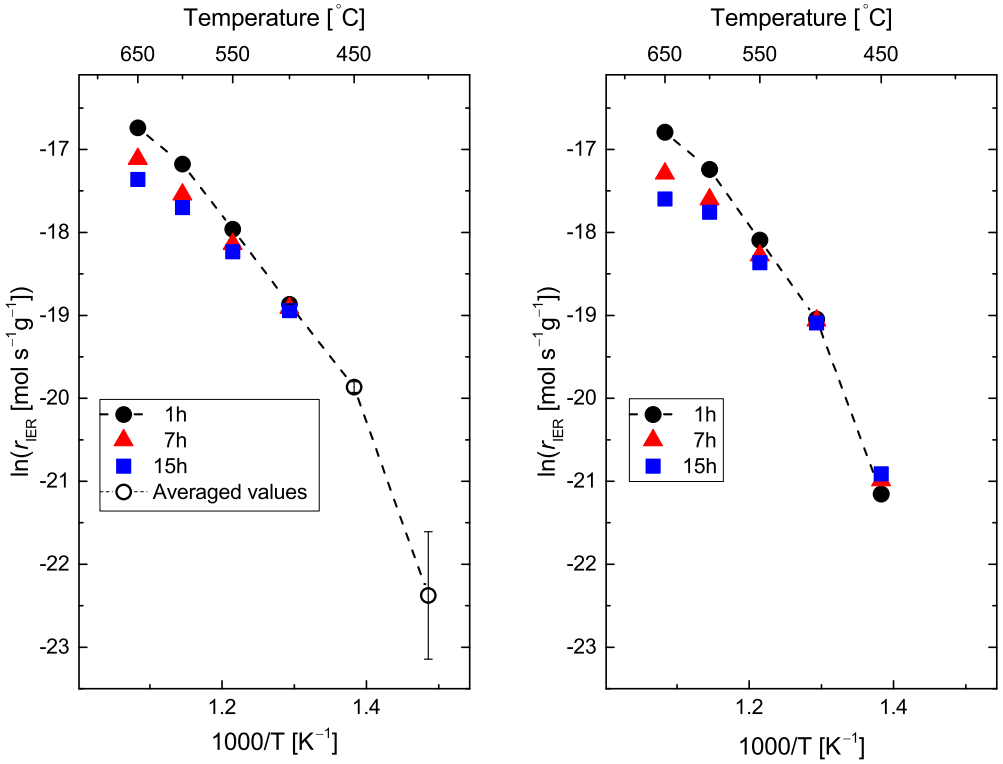

(a) S1 **(b)** S2

Figure 6.6: Temperature dependency of the IER after 1, 7 and 15 hours into the measurements of S1 (a) and S2 (b) (Fig. 6.5).

data-point at 400°C is included. At this temperature the rate of formation of $^{29}N_2$ was very slow making it difficult to determine the IER; hence the value has a large uncertainty. In both series the IER decreases more with time at higher temperatures. The slope in range 450–600°C in S1 and 500–600°C in S2 is seemingly linear, but levels off at 650°C. Further into the measurement the slope levels off at lower temperatures. In general, the temperature dependency decreases with increasing temperatures.

A similar series of measurements (referred to as S3X) was performed using three times the amount of catalyst sample (compared to S1 and S2) in order to achieve a faster increase of $^{29}N_2$, thus enabling higher measurement quality at lower temperatures. In Fig. 6.7a the IER at different temperatures is plotted versus time. In general,

the same trend as in S1 and S2 is observed; at 500–600°C the IER decreases with time, and the magnitude of the decrease is increasing with temperature. At 400–475°C the IER remains rather constant throughout the measurement, except for the first few hours at 425°C where it increases slightly. At the two lowest temperatures this increase is more evident and continues throughout the measurement. The Arrhenius

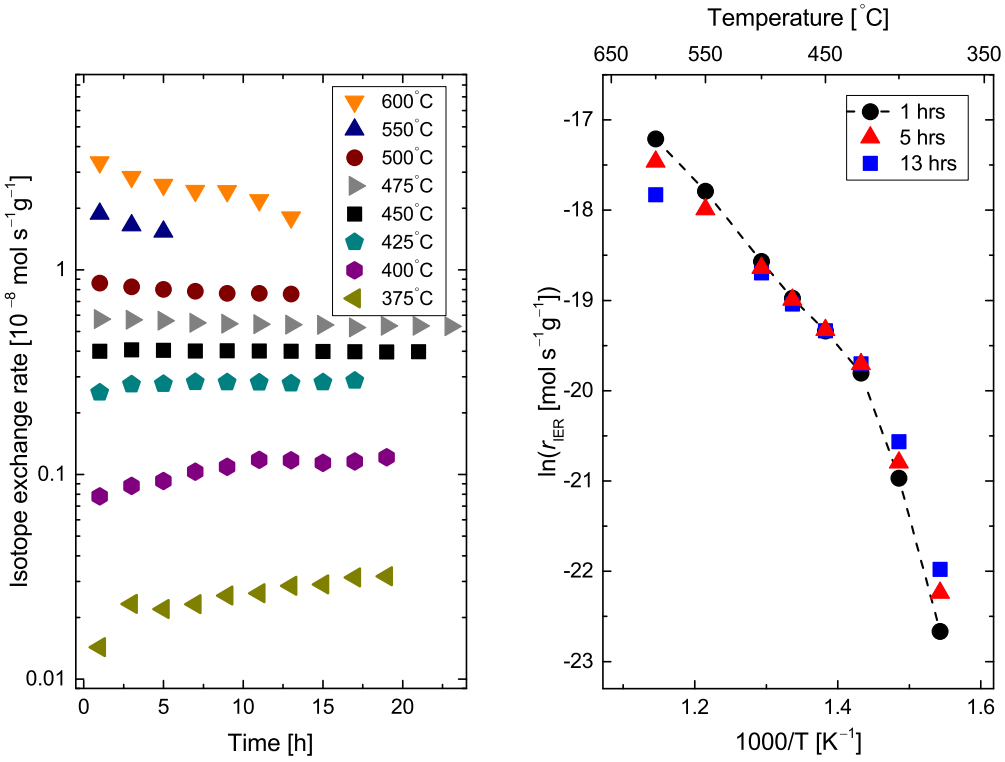

Figure 6.7: The isotope exchange rate versus time at different temperatures (a) and an Arrhenius-type plot (b) of the S3X series.

plot in Fig. 6.7b shows that the IER decreases more with time at the higher temperatures—as was also the case with S1 and S2. In temperature range 425–600°C and 375–425°C, different slopes are observed, and the former less steep than the latter. This shift is also indicated by S1 and S2. In these cases however, the shift appears at slightly higher temperatures.

6.2.2 Pressure dependency of the IER

The pressure dependence of the isotope exchange rate with respect to nitrogen partial pressure, was investigated at 450, 625, 650 and 700°C. Figure 6.8 shows the logarithm of the average IER as function of the logarithm of nitrogen pressure. Based on a power rate law (Eq. 2.6), the reaction order with respect to nitrogen partial pressure is

represented by the slope, and the intercept represents the logarithm of a rate constant k. The IERs are averaged over a certain time interval, e.g. the first 5 hours or first 13 hours of the measurements. Within each series of measurements, the average is taken over the same time-period. At 625°C and 700°C, a reaction order of 0.83± 0.02

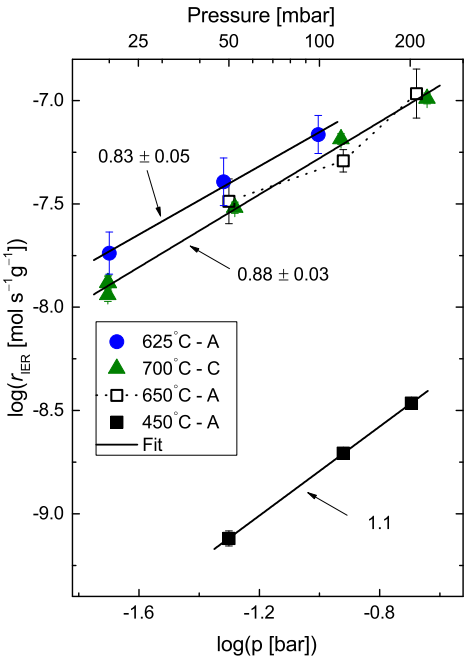

Figure 6.8: Nitrogen partial pressure dependency of the average IER, at different temperatures. The slope represents the reaction order with respect to nitrogen partial pressure. The letters in the legend represent the catalyst batches.

and 0.88± 0.03 is observed, respectively. The uncertainty in both cases is that of the linear fit, not the overall uncertainty of the reaction order. At 650°C, the log-log relationship is not linear; compared to 700°C, the middle data-point is lower than expected. A reaction order of 1.1 is obtained at 450°C.

6.2.3 The influence of water vapor on the IER

When water vapor was introduced to the evacuated reaction chamber containing catalyst sample, higher mass spectrometry ion currents of some of the traced masses were observed. This is shown in Fig. 6.9, where the relative ion currents are plotted versus time. The experiment was conduced at 600°C and 1 mbar of H_2O was introduced. At time of introduction, the signals of m/z = 2, 18 and 28 increase. Presumably also 44, however, the signal is close to the detection limit. The signal of water (18) increases for about 5 minutes before slightly decreasing. Both the signal of hydrogen (2) and nitrogen/carbon monoxide (28) are increasing until the isotope mixture is introduced.

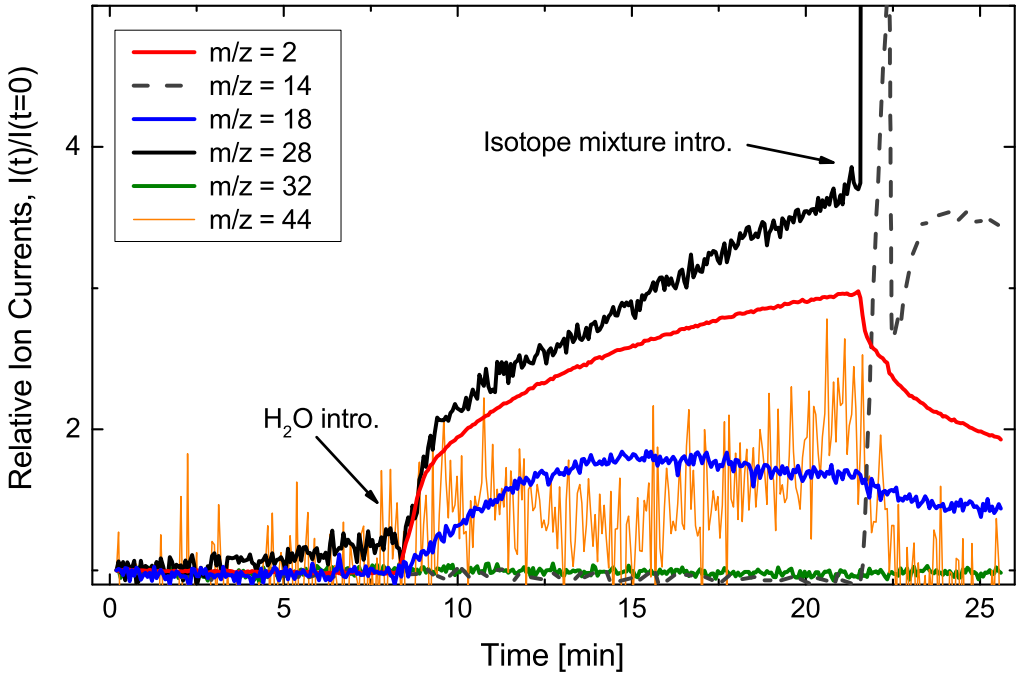

Figure 6.9: Relative ion currents (I(t)/I(t=0)) versus time. The times of introduction of water vapor and isotope mixture are marked with arrows.

At that time, the signal of hydrogen drops. This can presumably be explained by an increased total pressure which reduces the absolute amount of measured hydrogen. By normalizing the hydrogen signal against an inert species of constant abundance, the decreased signal could possibly be avoided. As suggested by Truszkiewicz et al. [43], the evolution of H_2 may indicate the presence of partially reduced barium:

$$\mathrm{Ba} + 2\mathrm{H_2O} \rightleftharpoons \mathrm{Ba(OH)_2} + \mathrm{H_2} \tag{6.1}$$

If the 28 signal is due to $^{28}N_2$, a small increase in the 14 signal, representing ^{14}N, is expected. When the isotope mixture is introduced, signal 14 increases, however, it does not increase when water is introduced. Nevertheless, the 14 signal prior to the introduction of isotope mixture was very low and small changes may thus be difficult to detect. On these bases, it is indicated that the increased signal of 28, as a result of the water, may be both due to CO formation and increased abundance of N_2. The former presumably formed in reaction between either water or oxygen with the carbon support, and the latter originating from leaks into the water vapor chamber prior to introduction.

Figure 6.10a shows how the IER is affected by the presence of water vapor at 575–

625°C. A similar trend is observed in both dry and wet conditions; the IER decreases throughout the measurement, more rapidly the first few hours. In wet conditions, however, the IERs are approximately 2×10^{-8} lower than those in dry. In Fig. 6.10b the temperature dependency of the IER in the two cases is presented in an Arrhenius-type plot. Each data-point is here the IER averaged over the first 3 hours of each measurement. In dry conditions, the slope corresponds to an apparent activation

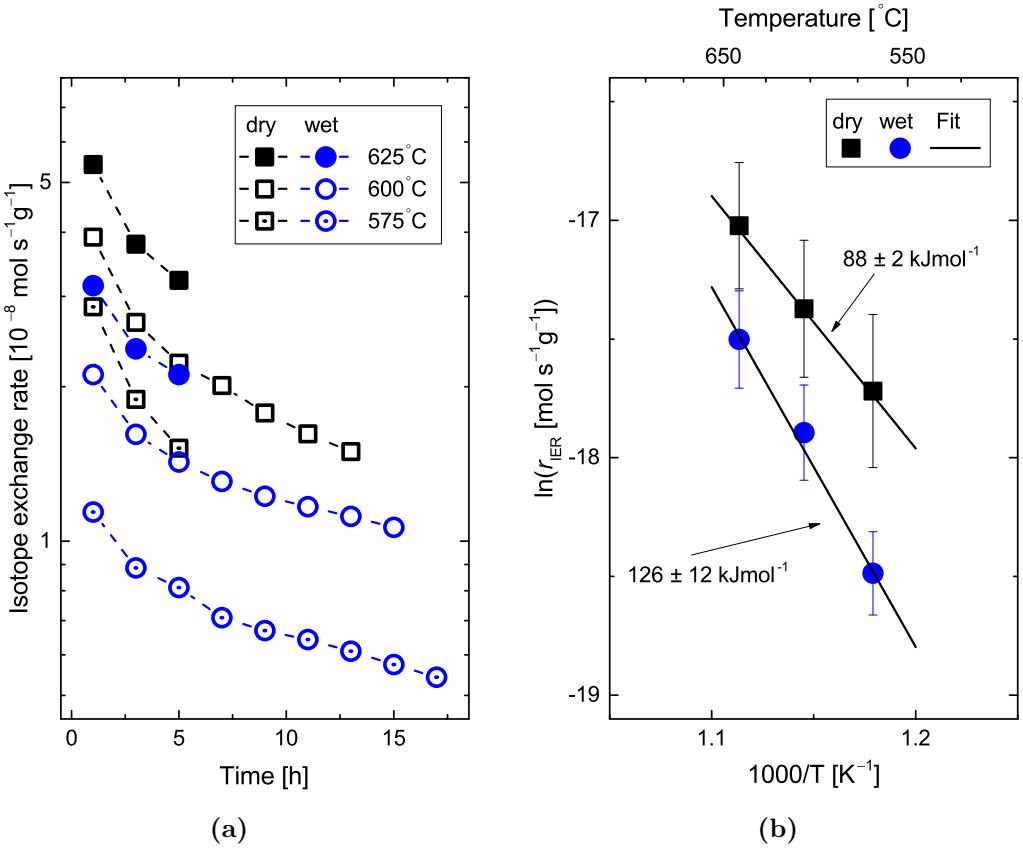

Figure 6.10: Rate vs. time (a) and Arrhenius-type plot (b) in dry and wet conditions.

energy of 88±2 kJmol^{-1}, while in wet conditions this is increased to 126±12 kJmol^{-1}. The error bars relate to the linear fit of the slope and not the overall uncertainty of the apparent activation energy.

6.2.4 High temperature deactivation of the catalyst

After a measurement at 700°C, the sample was further heated up to 750°C, where another measurement was performed. As shown in Fig. 6.11a, the IER was initially lower than at 700°C, but increased to higher values throughout the measurement. A subsequent measurement—also at 750°C—showed a practically constant (except for the first few hours) IER reduced by approximately 30% compared to at 700°C (1).

When the rate was measured once again at 700°C, after being at 750°C for several hours, it was reduced with half an order of magnitude. As seen in Fig. 6.11b, the apparent activation energy after deactivation is $155 \pm 2\text{kJmol}^{-1}$.

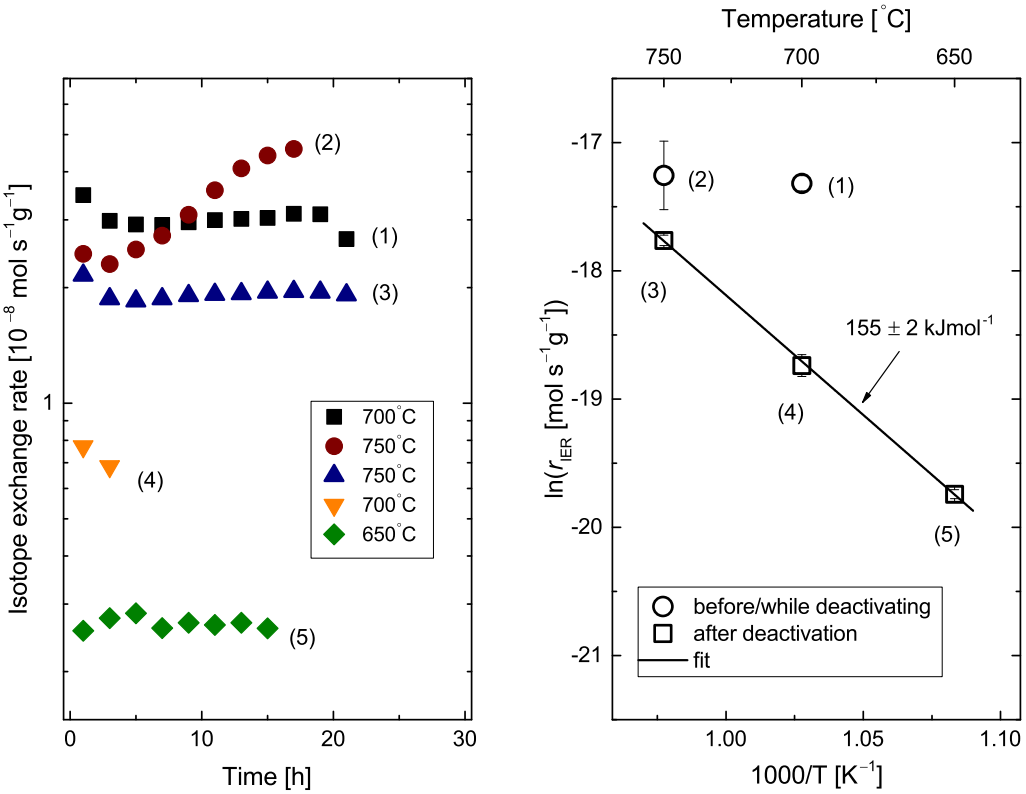

(a) (b)

Figure 6.11: Rate vs. time (a) and Arrhenius-type plot (b). In (b) the rates at each temperature are the average rates of the whole measurement. The numbers indicate the order at which the experiments were performed.

7 Computational Results

7.1 Adsorbed nitrogen on the Ru(0001) terrace

The relaxed structure of molecularly adsorbed N_2 and atomically adsorbed nitrogen are shown in Fig. 7.1 for the Ru(0001) surface. Four states of molecularly adsorbed N_2, three of which metastable, and two states of atomically adsorbed nitrogen, are found. In the stable molecular state, N_2 is adsorbed perpendicular to the surface on top site, and in the metastable states, the molecule is oriented parallel to the surface. Atomic nitrogen at the hcp site is the most stable species with an adsorption energy of $-194\,\mathrm{kJmol^{-1}}$/molecule (Table 7.1). Since this also is accepted in literature [26, 32, 36, 37, 73], from now on "the adsorption energy" refers to that of the atomic nitrogen at hcp site, unless otherwise noted.

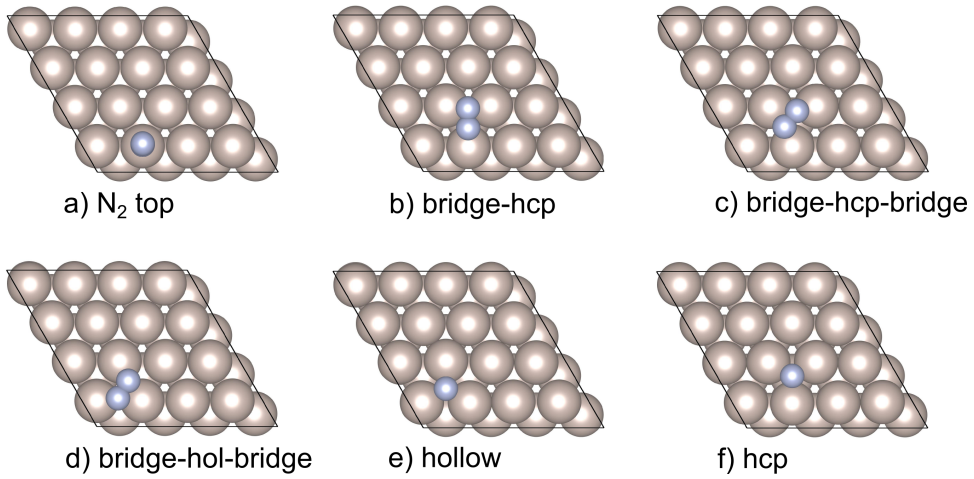

Figure 7.1: Illustration of the four states of molecularly adsorbed N_2 and the two atomic. "Bridge" refers to the site in between hollow and hcp.

The adsorption energy was calculated for coverages from 1 ML down to 1/16 ML (Fig. 7.2 and Table 7.1). Going down from 1 ML, the adsorption energy gradually decreases until 1/9 ML. A further decrease in coverage to 1/16 ML slightly increases the adsorption energy. The large coverage dependency of the adsorption energy is suggested by Mortensen et al. [26] to be related to "sharing" of the Ru atoms and

repulsive N-N interactions above 1/4 ML. The adsorption energy of N_2 at top site is significantly less affected by coverage compared to adsorbed atomic nitrogen.

Table 7.1: Adsorption energies of molecularly and atomically adsorbed states of nitrogen. The adsorption energy of N_2 at top site and atomic nitrogen at hcp site are computed for a set of different slab-coverages.

Position	E_{ads} (kJmol^{-1}/molecule)	Literature (kJmol^{-1}/molecule)
top (N_2) ($\theta = 1/16$)	-60	
top (N_2) ($\theta = 1/9$)	-62	
top (N_2) ($\theta = 1/4$)	-59	-45 [26]
top (N_2) ($\theta = 1/3$)	-63	-59 [26]
bridge-hcp (N_2) ($\theta = 1/16$)	1.3	
bridge-hcp-bridge (N_2) ($\theta = 1/16$)	3.3	
bridge-hol-bridge (N_2) ($\theta = 1/16$)	9.0	
hollow (N) ($\theta = 1/16$)	-61	
hcp (N) ($\theta = 1/16$)	-194	
hcp (N) ($\theta = 1/9$)	-205	
hcp (N) ($\theta = 1/4$)	-172	-150 [26]
hcp (N) ($\theta = 1/3$)	-145	
hcp (N) ($\theta = 2/3$)	-41	-37 ($\theta = 1/2$)[26]
hcp (N) ($\theta = 1$)	76	

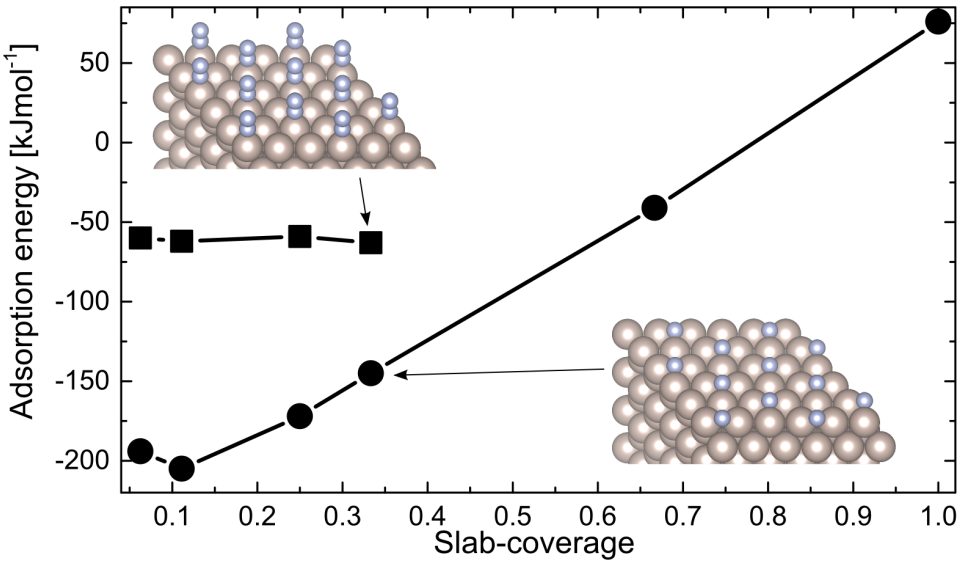

Figure 7.2: Adsorption energy of N_2 at top site (squares) and atomic nitrogen at hcp site (circles) as function of slab coverage (Table 7.1).

The equilibrium surface coverage of nitrogen has been calculated as function of temperature from Eq. 2.45, for each of the adsorption energies obtained for different

slab-coverage. In Fig. 7.3 each line represents the equilibrium surface coverage in a theoretical scenario where the N-N interaction—hence the adsorption energy—is constant with temperature. Thus, the equilibrium surface coverage in each case is only strictly valid when equal to the respective slab-coverage. The temperature at the point of equality therefore represents the temperature at which the respective coverage is the most favorable. These temperatures are listed in Table 7.2. Based solely on this, about 25% of the Ru surface is expected to be covered by nitrogen at conditions comparable to those in the isotope exchange experiments (i.e. 450°C and 50 mbar pressure, seen for example in Fig. 6.7).

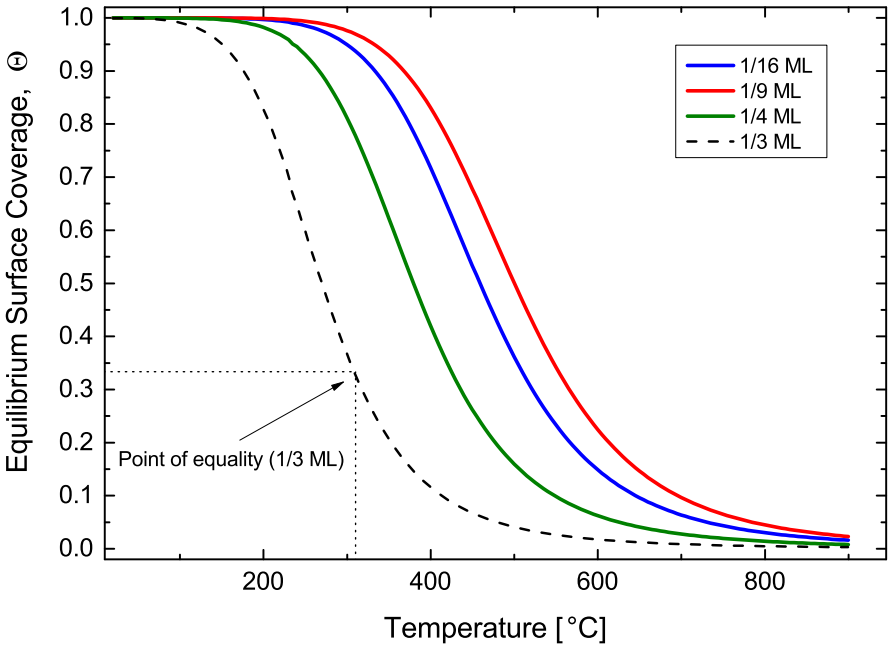

Figure 7.3: Equilibrium surface coverage of atomic nitrogen adsorbed at hcp site on Ru(0001), calculated from Eq. 2.45 at different adsorption energies. The respective slab-coverages are specified in the legend. The nitrogen pressure is 50 mbar.

Table 7.2: The temperatures at which the respective point of equality surface coverages are the most favorable.

Point of equality	Temperature (°C)
1/16	700–705
1/9	680–685
1/4	450–455
1/3	305–310
2/3	N/A
1	N/A

The equilibrium coverage calculated from 2/3 ML slab-coverage is several orders of magnitude lower than the others, increasing to a significant extent only at temperatures lower than -50°C. Due to the largely positive adsorption energy at slab-coverage of 1 ML, the equilibrium coverage increases from around 10^{-8} to around 10^{-6} in the temperature range. In both cases, the point of equality is not reached in the relevant temperature range.

7.2 Stepped Ru surface

A stepped surface was modeled by removing three rows from the top layer of a $4 \times 6 \times 7$ slab, leaving 3 rows of atoms between each step, exposing the highly active b5 site which extends from an hcp up 1-step (marked in gray in Fig. 7.4).

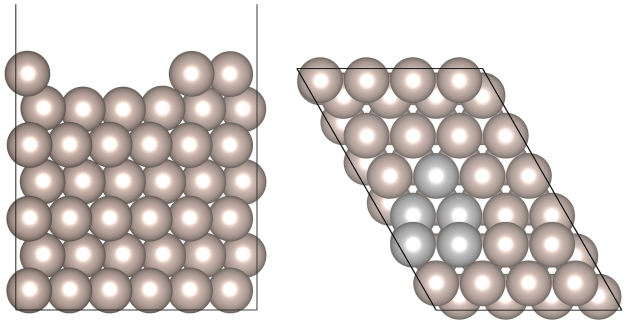

Figure 7.4: Side view (left) and top view (right) of the 3-row stepped $4 \times 6 \times 7$ slab. One b5-site is marked in gray.

The adsorption energy of molecularly adsorbed N_2 at the b5 site at -84 kJmol^{-1} is much more stable than its terrace equivalent at 9 kJmol^{-1}. This is explainable by the d-band of the step-atoms being raised in energy, which leads to an increased activity (section 3.2). This is further seen from the density of states (DOS) of bulk, terrace and step Ru in Fig. 7.5. The black line is the average discrete state energy, and as expected, it increases with decreasing coordination of the Ru-atoms.

7.3 Activation of nitrogen on a stepped Ru surface

The dissociation of N_2 up the step was investigated using the cNEB method, starting from molecularly adsorbed N_2 and ending with one N-atom at the b5-hcp site and the other at the first hcp site going up the step. The latter site is referred to as *hcphcp*. The resulting potential energy landscape, and notable configurations, are shown in Fig. 7.6. Initial calculations indicated that the b5 and the hcphcp configuration were separated by another local minimum, which is to the best of the authors knowledge,

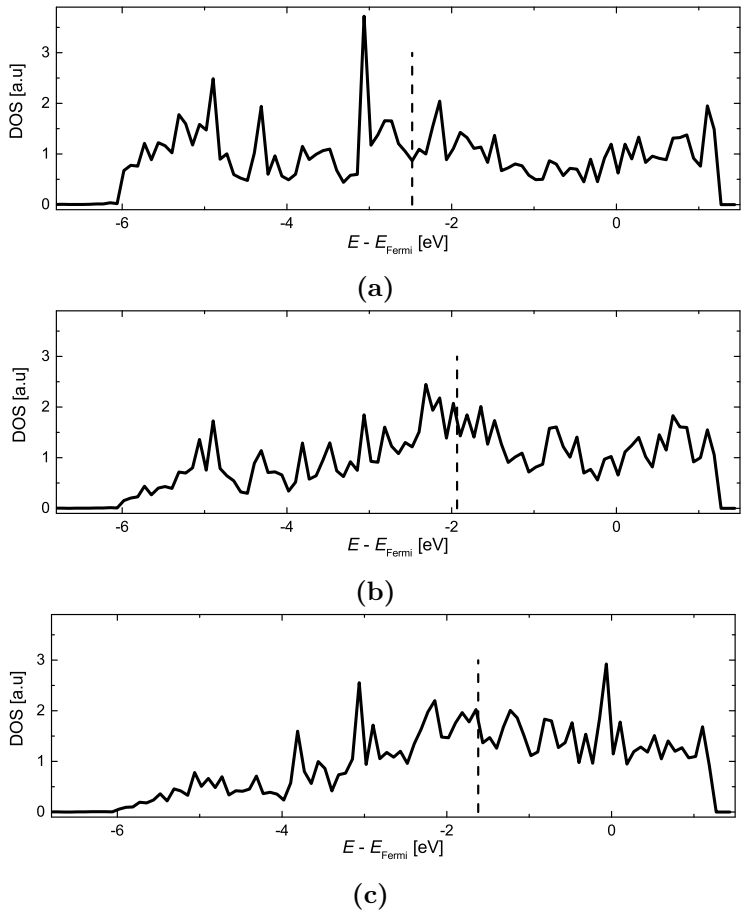

Figure 7.5: Density of states of the d-band versus energy in bulk (a), terrace (b) and step (c) Ru. The dashed lines represent the average discrete state energy, i.e., $E_i \times \mathrm{DOS}(E_i)/\mathrm{DOS}(\mathrm{total})$. The energy of the Fermi level is taken as energy zero.

not reported in literature. This means that the dissociation from b5 to hcphcp is in fact two elementary steps. At the local minimum, referred to as the *step-bridge* configuration, the N-atom going up the step is located at the step-bridge site while the other is located at the b5-hcp site. The adsorption energy of the step-bridge configuration is -109 kJmol^{-1}, 59 kJmol^{-1} higher than that of the hcphcp configuration at -168 kJmol^{-1} (Table 7.3). Since the dissociation starting in b5 and ending in hcphcp

Table 7.3: Adsorption energies of N_2 at the b5-site, and N-N at step-bridge and hcphcp configuration, on a clean (unpromoted) Ru step.

Configuration	N-N distance (Å)	E_{ads} (kJmol^{-1}/molecule)
b5	1.318	-84
step-bridge	3.116	-109
hcphcp	3.840	-168

is separated by a local minimum, two separate calculations were performed in order to properly resolve the minimum energy pathway and find the correct transition state (TS). One was performed using the b5 and step-bridge configurations as start and end-points, respectively, and the other starting in step-bridge and ending in hcphcp.

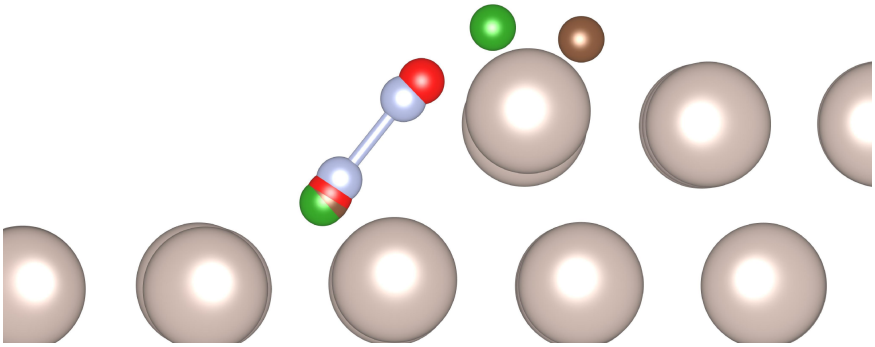

(a) Configurations of b5 (light-blue), TS (red), step-bridge (green) and hcphcp (brown).

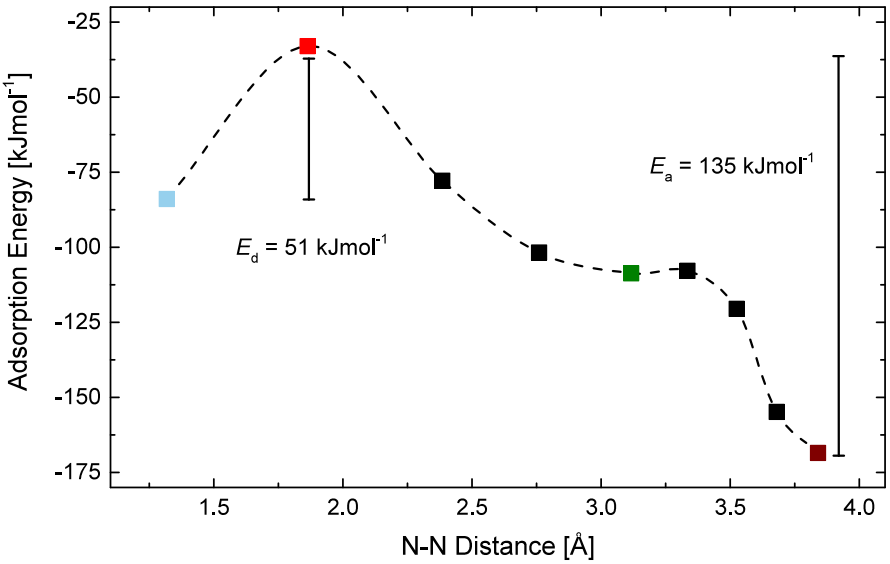

(b) Potential energy landscape of dissociation from the b5 to the hcphcp configuration.

Figure 7.6: Notable configurations (a) and potential energy landscape (b) of N_2 dissociation over a clean Ru step. The activation energy of dissociation E_d and association E_a are 51 and 135 kJmol^{-1}, respectively.

In the b5 site, N_2 has a bond length of 1.318 Å, which is longer than that of the terrace counterpart at 1.221 Å, and gas-phase N_2 at 1.117 Å,. This indicates that the molecule is somewhat stretched and more prone to dissociation. The bond length of

gas-phase N_2 is in good agreement with the computational [26], but larger than the experimental value at 1.0977 Å (NIST). Lengthening of diatomic bonds is expected with the PBE functional [74]. At a N-N distance of 1.864 Å and adsorption energy of -33 $kJmol^{-1}$, the main TS is found. This corresponds to an activation energy of 51 $kJmol^{-1}$. A very small barrier separates the step-bridge configuration from the hcphcp. The activation energy of association following the same mechanism the opposite way is 135 $kJmol^{-1}$.

7.4 Promoters at Step

To investigate how the activation of nitrogen is affected by the oxidation state of the barium promoter, three slabs with different Ba-species were created. One fully reduced, modeled by a single Ba ad-atom, one partially reduced, modeled as a single BaOH unit, and one fully oxidized, modeled as a single unit of BaO. Starting from different configuration, the promoters were allowed to relax. The most energetically stable configurations were found to be the b5 site for all promoters, with -OH and -O oriented up the step at bridge site (Fig. 7.7).

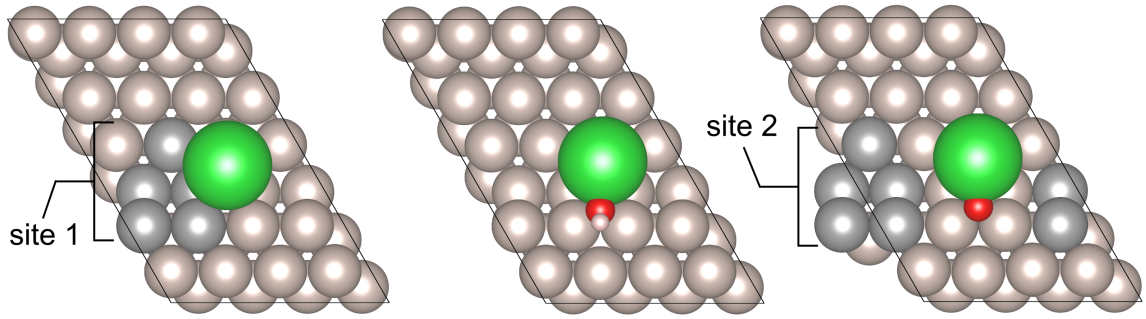

Figure 7.7: Configuration of Ba (left), BaOH (middle) and BaO (right). The five Ru atoms marked in gray in Ba and BaO slabs represent step-site one and two, respectively. The distance from the closest N-atom in b5-adsorbed N_2 to the Ba part of the promoters is 2.9 Å at site one and 5.6 Å at site two.

The adsorption energies of N_2 at the b5-site, and N-N in the step-bridge and the hcphcp configuration, were calculated in the three promoter scenarios, at the step-site closest (site one) and second closest (site two) to the promoter, respectively (Fig. 7.7). The results are listed in Table 7.4 and 7.5. At site one, the stability of all three configurations is increasing with the degree of reduction of the promoter, i.e. Ba>BaOH>BaO. Compared to the clean step, the configurations (except at b5 for BaO) are more stable, and the N-N distance of the b5 configuration is significantly

longer, while shorter at the step-bridge. At site two, a similar trend is observed, however, the difference between the promoters is less significant, showing that the proximity of the promoter is of importance.

Table 7.4: Site one adsorption energies of N_2 at the b5-site, and N-N at step-bridge and hcphcp configuration, on a promoted Ru step.

Promoter	Configuration	N-N distance (Å)	E_{ads} (kJmol^{-1}/molecule)
Ba	b5	1.353	-102
	step-bridge	2.893	-157
	hcphcp	3.853	-188
BaOH	b5	1.354	-93
	step-bridge	2.836	-131
	hcphcp	3.883	-180
BaO	b5	1.354	-81
	step-bridge	2.863	-118
	hcphcp	3.900	-177

Table 7.5: Site two adsorption energies of N_2 at the b5-site, and N-N at step-bridge and hcphcp configuration, on a promoted Ru step.

Promoter	Configuration	N-N distance (Å)	E_{ads} (kJmol^{-1}/molecule)
Ba	b5	1.323	-92
	step-bridge	3.122	-117
	hcphcp	3.838	-174
BaOH	b5	1.321	-89
	step-bridge	3.159	-115
	hcphcp	3.840	-172
BaO	b5	1.320	-88
	step-bridge	3.109	-115
	hcphcp	3.826	-171

7.5 Activation of nitrogen on a promoted Ru step

The activation of nitrogen was investigated at both site one and site two for all three promoted steps, in the same manner as for the clean step. The resulting potential energy landscapes are shown in Fig. 7.8, and the activation barriers of dissociation and association, as well as the TS energies, are listed in Table 7.6. In general, at site one, the activation energy of dissociation is significantly reduced by all three promoters by roughly 20 kJmol^{-1}, Ba slightly more than the two others. Also for association, the energy barrier is significantly reduced, however, in this case, the difference amongst the promoters is more evident. Ba reduces it by 19 kJmol^{-1}, BaOH by 15 kJmol^{-1} and BaO by 5 kJmol^{-1}. At site two, Ba is still the most effective promoter, however, both

the activation energy of dissociation and association are in fact increased compared to the clean surface. Another notable difference between site one and the clean step (as well as site two), is that the N-N distances of the TS are shifted to lower values; which is opposite of what happens in b5.

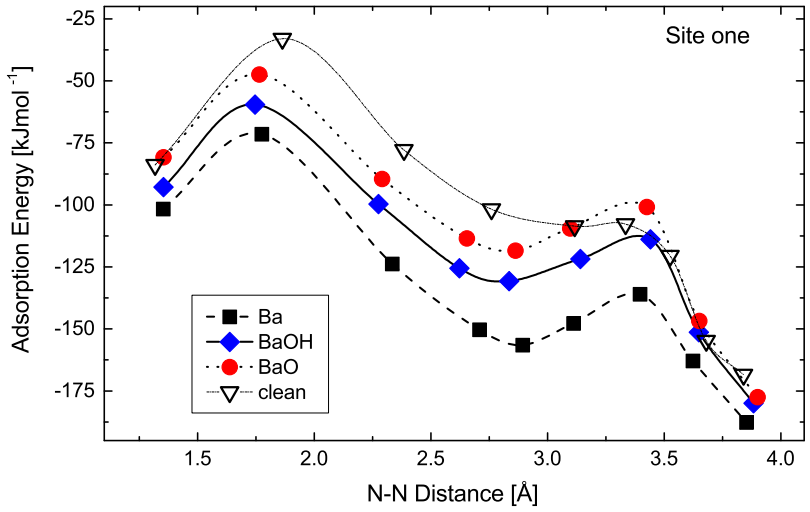

(a) Site one

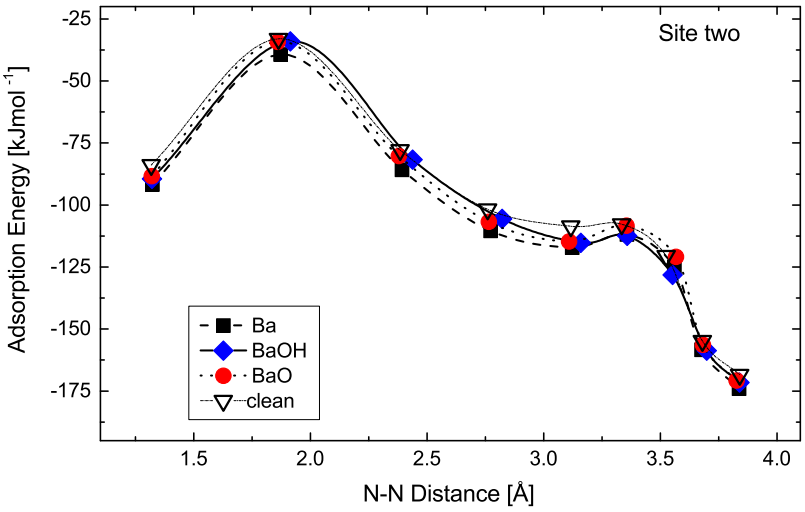

(b) Site two

Figure 7.8: Potential energy landscape of N_2 dissociation at site one (a) and site two (b) over a promoted Ru step.

Table 7.6: Summarizing list of the TS-energy, and activation energy of dissociation and association, for all systems. The values marked with $*$ are not final; i.e., the system could not be fully relaxed nor is a final high accuracy total energy calculation performed.

System	E_{TS} (kJmol^{-1})	E_{d} (kJmol^{-1})	E_{a} (kJmol^{-1})
Clean	-33	51	135
Ba - site one	-71	30	116
BaOH - site one	-60*	33*	120*
BaO - site one	-47	33	130
Ba - site two	-39	52	136
BaOH - site two	-34*	55*	138*
BaO - site two	-34	54	137

8 Discussion

In this chapter, the results from the computational investigation of nitrogen activation and the isotope exchange experiments will be discussed in light of relevant literature. A main focus is to elucidate the effect of the promoters chemical state on the catalytic activity and the activation energy of associative desorption of nitrogen.

8.1 Activation barriers from DFT

On the clean Ru(0001) step a barrier of 51 and 135 $\mathrm{kJmol^{-1}}$ is found for dissociation and association, respectively. The former is somewhat higher than the experimental single crystal literature values of $36 \pm 5\,\mathrm{kJmol^{-1}}$ and $39 \pm 10\,\mathrm{kJmol^{-1}}$ [29, 36], and other computational values in range 39–47 $\mathrm{kJmol^{-1}}$ [29, 73, 75]. The association barrier is, however, 10 $\mathrm{kJmol^{-1}}$ lower than the experimentally reported single crystal value [29]. In the computational studies [29, 73, 75], the association barrier is not reported. As the barriers are dependent on the nature of the promoter and the support, it is more relevant to compare promoted and supported Ru catalysts to the promoted step instead of to the clean. This is treated in a later section. Nonetheless, barriers in the range 27–60 $\mathrm{kJmol^{-1}}$ are expected for dissociation, and around 137–158 $\mathrm{kJmol^{-1}}$ for association [61, 62, 76].

One aspect of the deviation from the reported DFT values might be the computational method, where the exchange-correlation functional presumably is the most significant source of difference. In the present work, the PBE functional is utilized, while in Ref. [29, 73, 75] the functional used is revised-PBE (RPBE) [72]. This is expected to result in different adsorption energies as the various GGA functionals, such as PBE, generally overbinds adsorbed species (section 5.5), while in RPBE [72] the degree of overbinding is significantly reduced. For instance, Wellendorff et al. [77] found adsorption energies of -182 and -162 $\mathrm{kJmol^{-1}}$ for CO on Ru(0001) with a 1/4 ML coverage using PBE and RPBE, respectively. In comparison to the experimental value of -161 $\mathrm{kJmol^{-1}}$, RPBE is in much better agreement. Nevertheless, much of the difference between PBE and experimental values can be attributed to difficulties in comparing chemically dissimilar states, such as gas phase molecules and adsorbates (section 5.5). Thus, as the activation energy of dissociation and association is the

energy difference between chemically similar states, it is not expected to be equally affected by overbinding as the adsorption energy, which relates to the difference between a gaseous molecule and an adsorbate.

That being said, a difference of $14\,\mathrm{kJmol^{-1}}$ has been reported between PW91 and RPBE in the estimated barrier of diffusion (hcp-bridge-hollow) of atomic nitrogen on Ru(0001) [78]. In comparison to the experimental diffusion barrier of $91\,\mathrm{kJmol^{-1}}$, PW91 and RPBE overestimated the barrier by 23 and $9\,\mathrm{kJmol^{-1}}$, respectively [78]. Since PBE is more similar to PW91 in adsorption energies than RPBE [72, 77], it suggests that the transition states (TS) in this work are in fact affected differently than the start and end species. Thus, the activation barriers are also affected by overbinding, which possibly provides an explanation to the larger dissociation barrier of $51\,\mathrm{kJmol^{-1}}$ found in the present work.

In light of the above, it is also expected that the association barrier is somewhat larger than the experimental. However, the calculated barrier of $135\,\mathrm{kJmol^{-1}}$ is, on the contrary, $10\,\mathrm{kJmol^{-1}}$ lower than the experimentally reported single crystal value [29]. The latter was determined at a coverage of 0.15 ML [29]—which from symmetry corresponds to a step occupancy of around 1/3, i.e., every third b5-site (Fig. 7.4) is occupied. In the present work, the slab occupancy was 1/4. The barrier difference between this work and Ref. [29] could therefore be related to the slab coverage. The adsorption energy of atomic nitrogen at hcp site on terrace Ru(0001) has been shown highly dependent on the coverage, while molecularly adsorbed N_2 on the top site is nearly independent in the same coverage range (Fig. 7.2 and Table 7.1). The initial and final states of dissociation and association on the step, as well as the TS, are therefore presumably affected differently by changing coverage. In fact, the dissociation barrier on terrace Ru(0001) has been reported to increase by $15\,\mathrm{kJmol^{-1}}$ when the coverage is increased from 1/4 to 1/2 ML [26]. For the same increase in coverage, the adsorption energy of the final state increased by as much as $113\,\mathrm{kJmol^{-1}}$. Assuming the difference in dissociation barrier was largely due to destabilization of the TS, it can be estimated that the association barrier decreased by $98\,\mathrm{kJmol^{-1}}$ when the coverage was increased from 1/4 to 1/2 ML [26]. The different coverage dependency of the dissociation and association barriers observed on the terrace is presumably relatable to the step, since nearby intermediate species in ammonia synthesis, such as H and NH_2, are known to increase the dissociation barrier of nitrogen over the step [75], and suggested to decrease the association barrier [79]. Following the above, it is indicated that the association barrier calculated in this work would decrease if the nitrogen coverage increased. However, if the adsorption energy of the step hcphcp configuration (Fig. 7.6) is similarly dependent on coverage as atomic nitrogen on the terrace, it would mean that by increasing the step occupancy from 1/4 to 1/3—corresponding to 1/16 and

1/9 terrace ML, respectively—the association barrier would instead of decreasing be expected to increase slightly. Thus, it would become closer to the experimental value.

The barrier height of association is also affected by which configuration is taken as the initial state in the association reaction. In this work, the initial state is taken as the hcphcp configuration, where one nitrogen atom is adsorbed at b5-hcp and another is adsorbed at the first hcp site up the step (Fig. 7.6a). As adsorbed nitrogen on the terrace (1/16 ML) is 26 $kJmol^{-1}$ lower in energy than the hcphcp configuration, the experimentally reported barrier is expected to instead be reflected by the stability of terrace adsorbed nitrogen. In fact, it has been suggested that nitrogen atoms occupy the terrace before diffusing—presumably with a barrier around 91 $kJmol^{-1}$ as this is reported for Ru(0001) [33]—to the step for association [29]. While diffusion is very slow at room temperature, it is suggested as faster than associative desorption at the step at elevated temperatures, and hence not rate limiting [29]. Then, if nitrogen atoms sufficiently far away from the step on the terrace, with an adsorption energy of -194 $kJmol^{-1}$, is taken as the initial state of association, the barrier increases from 135 $kJmol^{-1}$ to 161 $kJmol^{-1}$. In light of the PBE overbinding, this is in much better agreement with the experimental value.

In summary, the calculated dissociation barrier is higher than the experimental and computational literature values, and the most significant cause of the difference seems to be PBE overbinding. For association the calculated barrier is on the contrary slightly lower than the experimental, while when diffusion to the terrace as well as coverage is taken into account, the barrier increases toward the experimental value.

8.2 The effect of promoters

The above discussion is also expected to be applicable to the promoted step. Thus, the calculated dissociation barriers for the promoted steps are presumably higher than the true barrier due to PBE overbinding. Similar behavior is expected for the association barrier, although this is also affected by what is taken as the initial state. In a case where the promoting effect is similar at the terrace and at the step, the energy barrier of association can be expected to increase to a somewhat higher value than the true barrier.

A potential issue with respect to comparison of the different promoters is that the magnitude of the overbinding seems to be dependent on the state or site of the adsorbates. This suggests that it may be difficult to unequivocally compare the relative effect of the promoters, as the species present in the three cases (i.e. Ba, BaOH and

BaO) differ. On the other hand, since the configuration of the promoter in each case is fairly constant throughout the dissociation process, the contribution from the promoter to overbinding of nitrogen in the different states can be expected to remain fairly constant. In that case, if the three promoting species contribute differently to overbinding, the potential energy landscape of nitrogen dissociation in the three cases would simply be shifted differently in energy. Thus, effects of PBE overbinding on the barriers of dissociation and association due to the promoters are expected to be rather small, and the relative effect of the promoters on the barriers should therefore be reasonably comparable.

The general picture from literature is that the Ru surface is partly covered by partially reduced Ba, BaO and $Ba(OH)_2$, where the chemical state is dependent on the environmental conditions [43, 44, 45]. Both structural [46, 79] and electronic [44, 45] promotion effects have been suggested, and more recently this has been linked to the chemical state, i.e., Ba acts as a electronic promoter, while BaO acts as structural promoter [43].

In the present work all three promoting species, Ba, BaOH and BaO, are suggested to act as electronic promoters, and are shown to reduce the nitrogen dissociation barrier at site one (Fig. 7.7) by approximately 21, 18 and 18 $kJmol^{-1}$, respectively. For dissociation at site two, the energy barriers increased slightly compared to the clean step. This significant dependence of proximity is in agreement with that expected for interactions of an electronic nature [38]. Because of this, an increased abundance of type one sites (Fig. 7.7) are expected to result in a higher overall effectiveness of the promoter. The increased activity for ammonia synthesis observed in Ru-Ba/AC with increasing promoter load (section 3.4.2) may be due to an increased number of type one sites.

All three promoting species reduce the site one dissociation barrier less than Cs on terrace Ru(0001), where the barrier was reduced by 28 $kJmol^{-1}$ [37], and slightly more than Cs on Ru/MgO, which reduced the barrier by 15 $kJmol^{-1}$ [61]. The former can presumably be explained from the lower electronegativity of Cs compared Ba, which could also explain the lower effect of BaOH and BaO relative to Ba. The larger reduction in dissociation barrier by Cs may also be related to a different promoting effect on the terrace compared to the step. To assess this further, both promoters should be investigated on both the step and the terrace. The difference in barrier reduction by the Ba promoters on the step compared to Cs on Ru/MgO may be related to Cs being in a hydroxide state on oxide supported Ru [45]; in that case, the barrier reduction is expected to be more similar to BaOH and BaO, as they are more comparable to CsOH in electronegativity [45]. For the association reaction, however, the effect of Cs on Ru/MgO is on the contrary more comparable to the single Ba atom and lowers the

barrier by 21 kJmol^{-1} [61].

Regardless of the proximity of the promoter, i.e., site one or two, the barrier of dissociation was only slightly affected by the chemical state of the promoter. However, for association, a clear difference was observed at site one, while at site two it was similar to that of dissociation at site two (Table 7.6). A possible explanation for this is the promoter model. Figure 8.1 illustrates notable configurations of nitrogen dissociating over a BaOH promoted Ru step. As in all three promoter cases, Ba was positioned at b5, while O/OH was oriented up the step. Because of this, the nitrogen

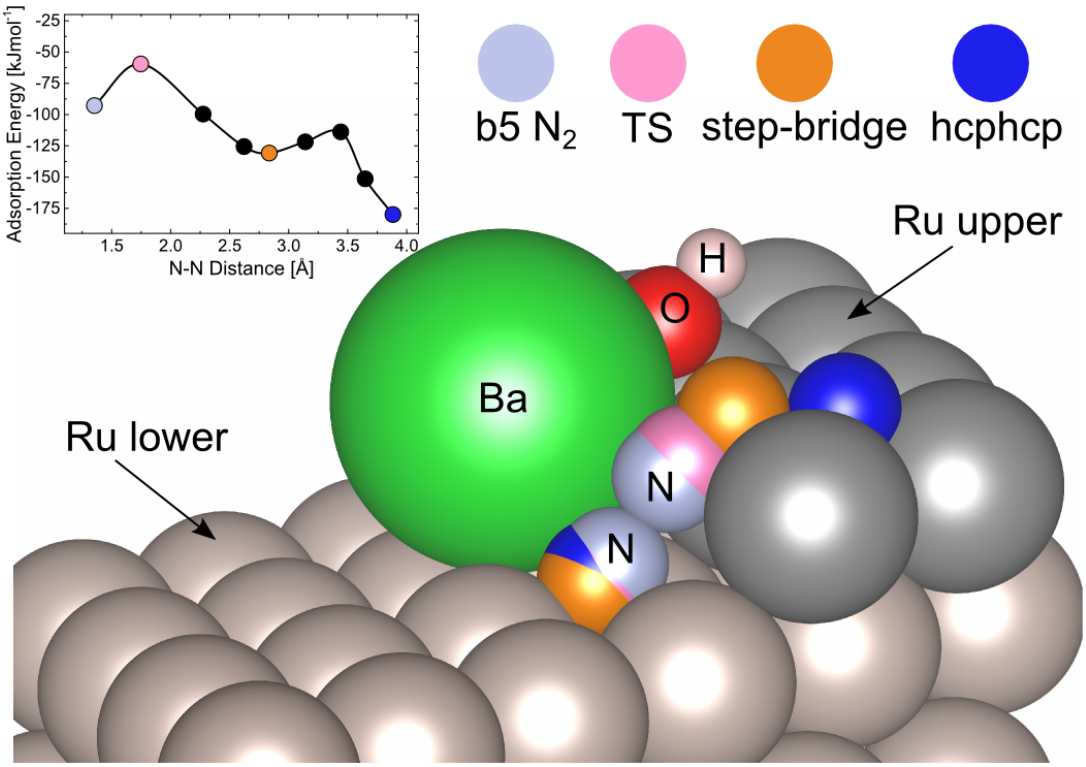

Figure 8.1: Notable configurations of nitrogen dissociation over a BaOH promoted Ru step.

atom moving up the step also comes in closer proximity to O/OH, which results in an unfavorable interaction. It is therefore evident that b5 N_2 at site one is less affected by the promoters chemical state than at the final hcphcp configuration. Even though the state of Ba presumably is affected by O/OH, the nitrogen configurations where both atoms are close to Ba (most notably b5 and TS), seem to be predominately affected by the Ba part of the promoter. At greater N-N distances, one nitrogen atom is predominately affected by Ba while the other atom is increasingly affected by O/OH. At site two there is less difference between the promoters with respect to the barrier of association, presumably because the nitrogen atoms feel a somewhat averaged elec-

trostatic interaction of the whole promoting unit.

On these bases, it is suggested that regardless of the overall chemical state of the promoter in a real system, where partially reduced Ba, BaO and $Ba(OH)_2$ are present, sites close to the Ba part are more active than sites close to the O/OH part. A possible explanation for the experimentally observed decreasing rate of ammonia synthesis with increasing abundance of $Ba(OH)_2$ [45] is provided.

As seen in Fig. 7.8, the local minimum of the step-bridge configuration could be even more affected than the other notable configurations by the presence of the promoter. In addition, the relatively small barrier separating it from the hcphcp configuration is shifted up in energy compared to the clean step. This intermediate minimum is not reported in the literature for nitrogen dissociation, however, a somewhat similar state is identified as the TS for NH + H = NH_2 [22]. Moreover, in the most stable state of NH_2, the nitrogen is positioned at the step-bridge site [73]. Zhang et al. [22] have suggested that NH_2 adsorbed at this site plays an important role in NH_3 synthesis, as it is unstable and prone to dehydrogenation. Since the promoters significantly stabilize the nitrogen dissociation equivalent of this state, it is possible that also the NH_2 state in ammonia synthesis is stabilized by the promoters. Thus, if NH_2 hydrogenation is particularly important in ammonia synthesis [22], the present work suggests that stabilization of this species may be an important role of the promoter.

8.3 Temperature dependency of the IER

In this section, the temperature dependency of the isotope exchange rate on Ru-Ba/AC is compared to relevant literature reports, and the observed trends are addressed. Since the IER changes with time, the temperature dependency of the IER is here presented based on averaged values with respect to time for each specific temperature (similarly to that in Fig. 6.10b), in order to treat the overall trend. The time dependence itself is specifically discussed in a later section.

8.3.1 Comparison to literature

In Fig. 8.2, the apparent IE activation energies (E_{app}) determined from S3X (Fig. 6.7), S1 and S2 (Fig. 6.6) are presented. The apparent activation energy for S3X is $64 \pm 2\,kJmol^{-1}$ in the temperature range 425–600°C. For S1 and S2 it is significantly higher at $82 \pm 3\,kJmol^{-1}$ (450–650°C) and $81 \pm 4\,kJmol^{-1}$ (500–650°C), respectively. Below 425°C, E_{app} for S3X increases to $178 \pm 14\,kJmol^{-1}$. Also for S1 and S2 the effect of temperature on the IER considerably increases at lower temperatures.

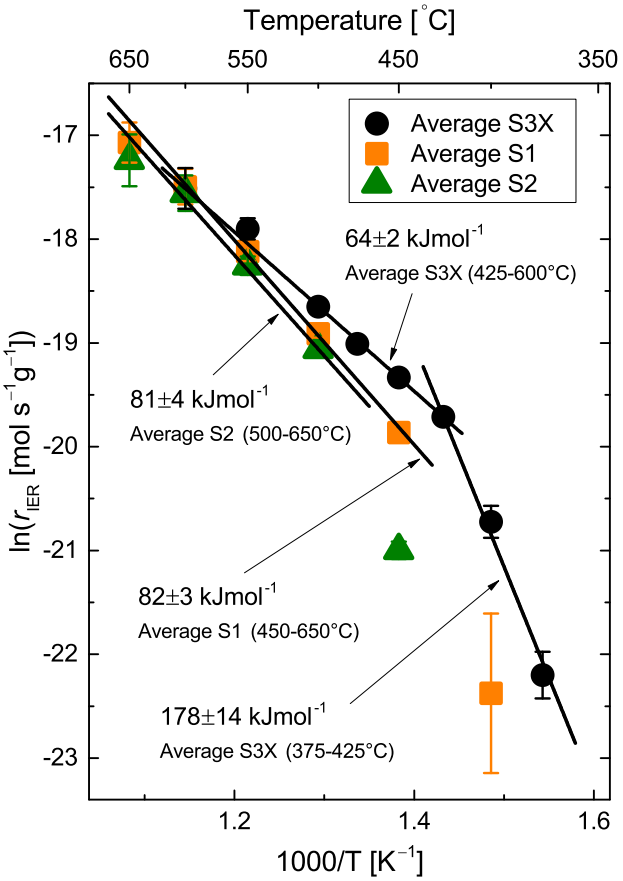

Figure 8.2: Temperature dependency of the averaged IERs in measurement series S1, S2, S3X (Fig. 6.6 and 6.7).

For Ru-K/AC and Ru-Cs/MgO, the apparent IE activation energy has been reported to 96 kJmol^{-1} (250–450°C) and 137 kJmol^{-1} (167–400°C), respectively [60, 61]. Both of these are in between the values found for Ru-Ba/AC in the present work. Raróg-Pilecka et al. [79] showed in a comparison of the three promoters K, Cs and Ba on Ru/AC, that the temperature of desorption maximum was shifted up 80°C by Ba compared to K and Cs, based on N_2 temperature-programmed-desorption (TPD). This indicates that the activation energy of IE, as it is limited by associative desorption, is higher on Ru-Ba/AC than on Ru-K/AC and Ru-Cs/AC. Since the reported E_{app} on Ru-K/AC is 96 kJmol^{-1} [60], it suggests that an E_{app} above this value is reasonable for the apparent IE activation energy on Ru-Ba/AC. Moreover, as the rate limiting step for NH_3 decomposition is regarded as associative desorption of N_2 [63, 79, 80], the activation energies of IE and NH_3 decomposition should be similar. For Ru-Cs/AC and Ru-Ba/AC, the latter is reported to 134 and 158 kJmol^{-1} (370–400°C), respectively [79]. The apparent activation energy of IE is presumably slightly higher than that of NH_3 decomposition, as adsorbed nitrogen may be destabilized through repul-

sive interactions with nearby intermediates of NH_3 decomposition, such as NH, H and NH_2, leading to a lower barrier of associative desorption of N_2 [79]. Thus, based on the computational results and literature reports, it is more plausible that the apparent IE activation energy obtained below 425°C represents associative desorption-limited isotope exchange, rather than that below 425°C.

Figure 8.3 summarizes the comparison of the experimental and computational activation energies presented in this work to values reported in the literature. Activation energies of processes limited by associative desorption of nitrogen obtained at various temperatures are presented.

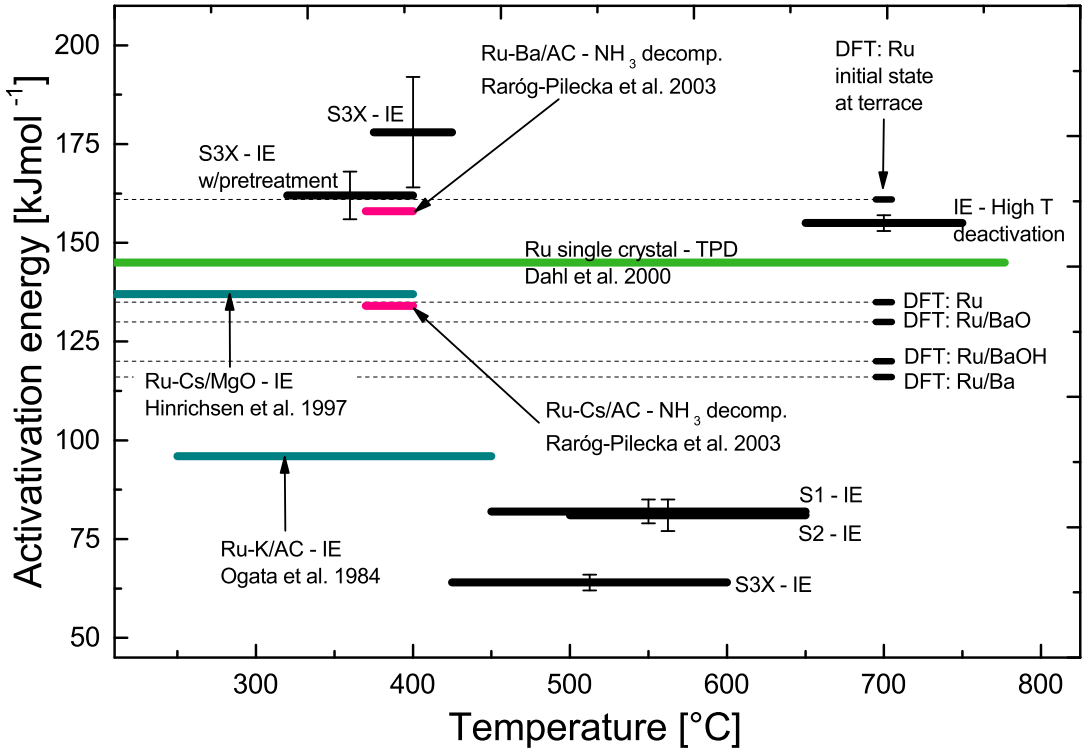

Figure 8.3: Summarizing figure of activation energies of processes limited by associative desorption of nitrogen obtained at various temperatures. Results of the present work are marked in black. The literature values are from Ref. [29, 60, 61, 79].

8.3.2 Temperature regimes of the apparent activation energy

The decreasing apparent activation energy (Fig. 8.2) when going to higher temperatures may indicate that different processes are rate limiting at high and low temperatures. The activation energy at higher temperates seems too low for a associative desorption-limited IE reaction, and in addition, too high for dissociative adsorption.

Limitations by mass transfer in the reaction chamber have been reported to cause a plateau in the temperature dependency of the O_2 IER at higher temperatures [81]. However, as this was O_2 exchange where the IER was much higher and the statistical equilibration time was around 5 hours or less—which is one order of magnitude less than in the present work. Thus, such limitation seems implausible.

A possible explanation for the changing slope is reaction limitations by pore diffusion in the high temperature regime. In highly porous catalysts when the intrinsic catalytic activity is high at elevated temperatures, the transport of reactants to and from the active sites inside narrow pores may become rate limiting [4]. In such a case, the apparent activation energy is reduced to half the original value [4]. Then, if the apparent activation energy in the high temperature regime (Fig. 8.2) is in fact half of the true value due to pore diffusion limitations, the true value is expected to be in range 128–164 $\mathrm{kJmol^{-1}}$. An apparent activation energy of this size is both closer to the low temperature value and that after high temperature deactivation, as well as in better arrangement with computational results and with the literature.

On these bases, lower porosity may be a possible explanation for the increase in apparent activation energy in the high temperature regime after high temperature deactivation (Fig. 6.11). Lower porosity could both explain the overall lower activity as much active surface area would be lost, and the higher apparent activation energy as pore diffusion would no longer limit the IER. The possibility of reduced porosity was further investigated by surface area and pore volume determination through N_2 adsorption (BET) measurements (section 4.2.3). The amount of deactivated catalyst was not sufficient for proper determination, so another sample with a larger amount of catalyst was heated at 750°C for several hours to achieve high temperature deactivation before the N_2 adsorption measurements. The IER decreased more than an order of magnitude the first 13 hours while heating the sample at 750°C. This can indicate that the sample was deactivated, but this is not conclusive as the activation energy was not determined. Moreover, the surface and pore volume of the presumably deactivated sample did not change significantly compared to the other samples (Table 6.1), which suggests that either the loss of surface area and pore structure was not the cause of the high temperature deactivation, or that deactivation was not achieved.

The low activity observed in the high temperature deactivated sample could potentially be explained by loss of active surface area due to Ru sintering—as seen in section 6.1.2 the abundance of larger particles might have increased. Moreover, the increase in apparent activation energy of approximately 90 $\mathrm{kJmol^{-1}}$ could be related to the highly catalytically active b5-type sites no longer dominating. In that case, the desorption would proceed on the terrace, where the activation barrier is reported to 218 $\mathrm{kJmol^{-1}}$ for Ru(0001) single crystal and 230 $\mathrm{kJmol^{-1}}$ from DFT calculations [29]. Although

the barium promoter, and promoters in general, significantly reduce the barrier of associative desorption, a reduction of more than $60\,\mathrm{kJmol^{-1}}$ seems implausible.

8.3.3 Variable promoting effect

If the abrupt change in apparent activation energy is due to limitation by pore diffusion, the apparent activation energy at high temperatures should be half of the true value, and the apparent activation energies for S3X in Fig. 8.2 are then not fully in agreement. This may possibly be related to gradual catalyst deactivation, most importantly in terms of the state of the promoter.

In all three measurement series, S1, S2 and S3X, the same method was followed: starting at high temperature (650°C for S1 and S2, and 600°C for S3X) and evacuating the reaction chamber in between measurements. As the pressure is reduced significantly during evacuation, equilibria involving a surplus of reactant gas species are left shifted. Thus, the equilibria suggested as responsible for changing the state of the promoter,

$$\mathrm{Ba} + 2\mathrm{H_2O} \rightleftharpoons \mathrm{Ba(OH)_2} + \mathrm{H_2} \tag{8.1}$$

$$\mathrm{BaO} + \mathrm{H_2O} \rightleftharpoons \mathrm{Ba(OH)_2} \tag{8.2}$$

and hence the effect, are also left shifted. As a result, evacuation of the reaction chamber has a regenerative effect on the catalyst. However, since the effect of the carbon support as a reducing agent increases with temperature, and reaction 8.1, 8.2 and $\mathrm{Ru} + \mathrm{O_2} = \mathrm{RuO_2}$ are exothermic (HSC Chemistry 8.2.0), the degree of regeneration decreases with decreasing temperature. Consequently, the overall state of the promoter will change with temperature. Since the state of the promoter influences the dissociation and association barriers, the apparent activation energy of the IE reaction may be differently affected by the promoter at different temperatures.

In section 7.5, it was shown that the site specific activation energy for nitrogen association at a step—which dominates the activity [29]—is significantly influenced by the chemical state of the promoter. In this respect, the apparent activation energy of the IE reaction is dependent on the overall chemical state of the promoter. Thus, if the overall state of the promoter is fixed, a given apparent activation energy is measured. However, if the state is changing with conditions (e.g. temperature), the number of active sites with a given site specific activation energy also changes. As a result, when going down in temperature, the IER decreases not only due to the site specific activation energy, but also due a changing ratio of sites with different specific activation energy. This is illustrated in Fig. 8.4. For instance, if the ratio of promoting

species Ba:BaO:$Ba(OH)_2$ is 0.2:0.7:0.1, the activation energy is expected to be lower than for the ratio 0:0.4:0.6 since the effectiveness follows Ba>BaO>$Ba(OH)_2$. As the promoter ratio is temperature dependent, the IER increases with temperature both because isotope exchange is a thermally activated process, and because the intrinsic catalytic activity increases. The effect of changing ratio of promoters were possibly

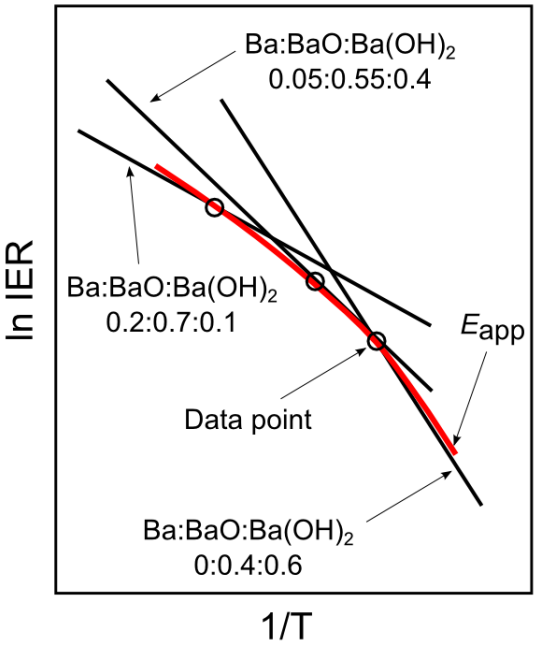

Figure 8.4: Illustration of the influence of the promoters state on the apparent activation energy. The black lines illustrate the arbitrary temperature dependency of a catalyst with a constant ratio of Ba:BaO:$Ba(OH)_2$.

observed when water vapor was introduced to the reaction chamber (Fig. 6.10b). The promoter reacts more with H_2O at lower temperatures since the equilibrium is right shifted [45], which results in a corresponding decrease in the IER. Thus, the apparent activation energy under wet conditions is increased compared to at dry.

The above provides a possible explanation for the apparent activation energy in the high temperature regime being less than half of that at low temperatures: the intrinsic activation energy is lower at high temperatures since the promoter equilibria are left shifted. A slightly lower apparent activation energy would then still be observed at higher temperatures if pore diffusion was not limiting. Thus, the magnitude of the shift in apparent activation energy is presumably increased due to deactivation mainly through promoter changes.

To further clarify the effect of deactivation in the low temperature regime, a series of measurements were performed where the catalyst was pretreated at 550°C for 3 hours under evacuation prior to each measurement. This is shown in comparison to the S3X

measurement series in Fig. 8.5. At all temperatures the IER significantly increased

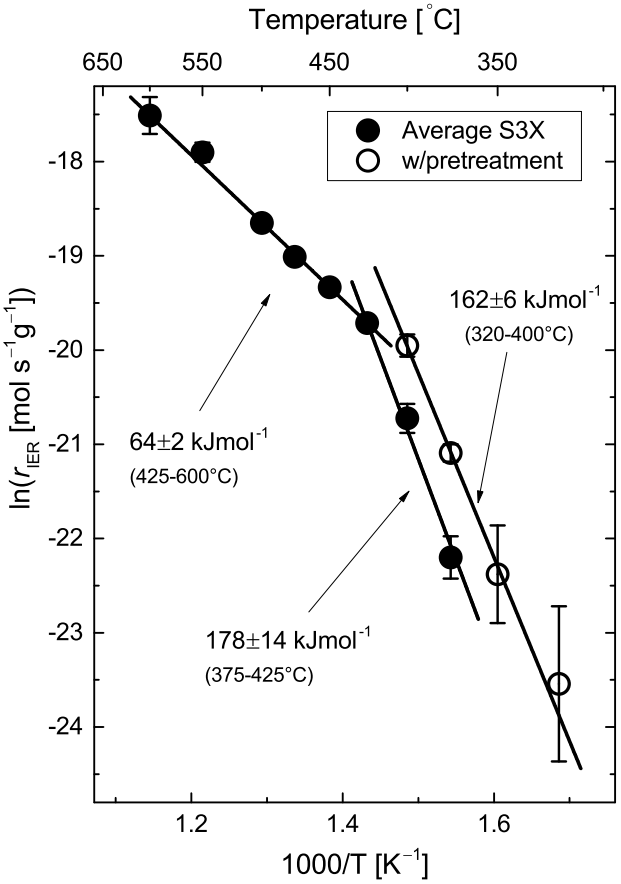

Figure 8.5: Temperature dependency of the averaged IER in S3X and in a low temperature series where the catalyst was pretreated for 3 hours at 550°C under evacuation prior to each measurement.

compared to the ones measured without pretreatment. Furthermore, the apparent activation energy also seems to be slightly lower. Both of which is in agreement with the above discussion.

8.3.4 Difference between S1, S2 and S3X

The apparent activation energy of the S1 and S2 measurement series compared to S3X is slightly higher (Fig. 8.2). This is possibly related to the amount of catalyst used in the measurements. In the latter, three times the amount of catalyst was used compared to S1 and S2. Assuming the IER scales linearly with the amount of catalyst, $\frac{\mathrm{d}^{29}\mathrm{N}_2}{\mathrm{d}t}$ becomes larger and more distinct from instrumental noise in the signal. This is especially important at lower temperatures where exchange is slow. Moreover, the conditions might be somewhat more reducing since more carbon is present in the

reaction chamber, and the regenerative effect will therefore be greater. In addition, assuming that the amount of species responsible for deactivation is equal in all three measurement series, an increased amount of catalyst will result in a smaller percentage of the catalyst deactivating. Thus, the increased slope of S1 and S2 above 450°C compared to S3X may be explained by the latter being less prone to deactivation due to the increased amount of catalyst used.

8.4 Pressure dependency of the IER

The pressure dependency in the high temperature regime was investigated at three different temperatures. As seen in Fig. 6.8, the IERs are higher at 625°C than the corresponding IERs at 650 and 700°C. The low IERs at 700°C series compared to the other two can possibly be explained by this sample being from a different catalyst batch (section 6.1). Thus, it is plausible that the IER differences are due to factors such as different promoter content and active surface per gram of catalyst. Similar is presumably true for the 625 and 650°C measurements series, even though they are both from the same batch (A). As seen in section 6.1, the powder seems to be somewhat inhomogeneous in terms of barium content. The two samples may therefore have different overall Ba:Ru ratio, and in addition, they may also have different active surface area due to catalyst particle segregation. In turn this may influence the activity. Nevertheless, these differences should not significantly influence the pressure dependency more than the overall uncertainty of the measurements.

The reaction order of ammonia synthesis with respect to N_2 partial pressure is usually found to be in range 0.8–1 for catalysts similar to Ru-Ba/AC [62, 62]. In the present work, the reaction order in both temperature regimes are in agreement with this, and the different reaction order in the two regimes may therefore well be due to uncertainty in the data. That being said, one may speculate that it might instead indicate that two different processes are limiting at high and low temperatures. Which is in agreement with the different temperature dependencies.

8.5 Time dependence of the IER

Ideally, in a closed system at a given temperature, where the catalyst surface is in thermodynamic equilibrium with the gas phase, the isotope exchange rate (IER) is constant. In the present work it has however been shown that the IER changes with time at high and low temperatures, while being constant at intermediate. Similar changes as observed above 500°C have been reported for the rate of ammonia synthesis below 400°C [45]. In that case the decreasing rate is ascribed to formation of $Ba(OH)_2$ from BaO and H_2O. As discussed earlier, the state of the promoter also influences

the IER, however, the reaction conditions are rather different compared to those of ammonia synthesis, and the time dependent changes may therefore have other causes as well.

8.5.1 Nitrogen coverage

In this subsection, the changing IER is treated in light of nitrogen coverage in an ideal scenario where the catalyst surface is otherwise constant with time.

The coverage of nitrogen increases with increasing pressure (Eq. 2.14), and similarly does the IER (section 6.2.2). Hence, the IER increases with coverage, and it is evident that increased coverage is not the cause of the decreased IER at higher temperatures. On the other hand, if the coverage slowly decreased with time, a decreasing IER would be expected. For instance, at 650°C in S1 (Fig. 6.5), the IER decreased approximately 50% over the first 15 hours. This cannot be explained by a higher coverage prior to gas introduction than after, as the pressure under evacuation is about three order of magnitude lower than after introduction.

On the contrary to at higher temperatures, the IER increases with time below 450°C. As the IER is expected to increase with coverage, this is a plausible explanation. Since the rate of adsorption depends exponentially on temperature—and in the case of N_2 on Ru it is highly activated [29]—it takes longer time to reach saturation coverage below 450°C than above 500°C. In addition, the saturation coverage is higher at lower temperatures (Fig. 7.3), which contributes to an increased equilibration time. The degree of change in the IER is also more evident for S3X, where 3 times as much catalyst was used. Thus, it is suggested that time dependent increase of the IER below 450°C may be an effect of longer surface-gas phase equilibration time.

8.5.2 Gradual change of catalyst state

As discussed in section 8.3.3, the state of the promoter is highly important for the activity, and it is dependent on several factors, such as the presence of H_2O and temperature. Moreover, a reduced number of active sites due to Ru oxidation or competitive adsorption (section 2.2.3) will also decrease the IER. It is therefore reasonable that the time dependent decrease in the IER at higher temperatures is related to changes in the catalyst state.

In all three measurements S1, S2 and S3X, the presence of other gases was minor. Nevertheless, small amounts of impurity gases may be introduced to the reaction chamber with the isotope mixture or gradually through small leaks during the measurement. The most abundant impurities are probably H_2O and O_2, where the former reacts with the promoter evolving H_2 (Fig. 6.9) [43] and the latter with the carbon support forming CO and CO_2. However, since nitrogen adsorption reaches equilibrium

at high temperatures after a short period of time, it seems improbable that it takes the impurity gases in the isotope mixture 10 hours or more to react. This is indicated by the influence of water vapor on the IER (Fig. 6.10b): the IER is significantly reduced already at 1 hour (first data point) and the IER subsequently decreases in a similar manner as to in dry conditions. Thus, much of the gradual change is suggested to be related to small leaks.

Nevertheless, no significant change in pressure or in the MS signals corresponding to air molecules or their potential products through reactions with the catalyst were observed. The amount of leak is therefore presumably minor. However, in this regard, leakages can be masked in two ways: firstly, if a significant amount of the gas adsorbes on or reacts with the catalyst, the increase in pressure and MS signals would be less than what is expected for a similar sized leak where all species are in gas phase. Secondly, if a small leak is composed of several species, the contribution of each to the respective MS signals would be minor, and possibly close to the detection limit. That being said, small amount of impurity gases can potentially result in a significant decrease in the IER as the activity is strongly dependent on a rather small amounts of partially reduced Ba and highly active step sites [19].

The relative change in the IER increases with temperature, and the rate of change decreases with time. This can possibly be explained by a fairly empty surface and left shifted promoter equilibria at higher temperatures (section 8.3.3). Since the amount of partially reduced Ba is rather small (below 20 mol% of the total Ba content [43]), but nonetheless very active, gases reacting with the reduced promoter will probably have the greatest effect on the IER. As more promoter is oxidized, reactions between water and the promoter has less effect on the IER. Since the promoter is not fully regenerated in between measurements, the initial amount of partially reduced Ba is less in subsequent measurements. Thus, the largest changes in the IER can possibly be attributed to oxidation of the promoter, and slower changes may be more closely related to formation of barium hydroxide. At intermediate temperatures, the IER is constant presumably due to saturation of $Ba(OH)_2$.

8.6 Future work

In the discussion regarding the validity of the computational results a main topic was the effect of overbinding due to the PBE functional. Performing key calculations using the revised PBE functional would therefore be of importance. Moreover, elucidating the promoted Ru(0001) terrace in combination with diffusion to and from the step would allow for better comparison with literature, as well as the results of isotope exchange. Lastly, both experimental and computational studies in the literature of

the Ba promoter in regards of nitrogen activation are scarce, thus, performing similar calculations for Cs, and possibly IE measurement, could give a more quantitative comparison with literature and different catalyst systems.

A more thorough investigation of the high temperature deactivation of the catalyst would be of interest. In order to exclude that the lossof porosity was the cause of the high temperature deactivation, N_2 adsorption (BET) has to be performed on a sample that certainly is deactivated, i.e., a significantly higher apparent activation energy is measured after high temperature treatment is performed.

Investigation of the water vapor pressure dependency at different temperature regimes would further elucidate the state of the promoters. In this regard, including a bed of drying agent (e.g. P_2O_5) at the cold zone of the reaction chamber would presumably allow for measurements less influence by H_2O impurities from leakages and from the isotope mixture. Thus, such experiments would provide valuable information regarding the time dependent deactivation, as well possible temperature dependencies of the apparent activation energy.

9 Conclusions

On the basis of the computational and experimental results, it can be concluded that nitrogen dissociation and association on barium promoted ruthenium catalysts is highly dependent of the chemical state of the barium promoter.

Through computational methods, the adsorption energy of N_2 on the Ru(0001) terrace was shown to be significantly less dependent on the surface coverage compared to adsorbed atomic nitrogen. Both species were more strongly adsorbed to the surface compared to what is reported in the literature. The N_2 dissociation energy on the clean step was calculated to 51 kJmol^{-1}, which is slightly higher than values reported in literature. The differences from the literature are mainly attributed to the tendency of the PBE functional to overbind adsorbates. The association energy calculated to 135 kJmol^{-1} is slightly lower than literature values due to what was defined as initial state of association. When instead the terrace adsorbed nitrogen was taken as initial state to account for diffusion along the terrace, the energy barrier of association increased to 161 kJmol^{-1}, which is in better agreement with the literature.

In close proximity of a unit of atomic Ba, BaOH or BaO, the nitrogen dissociation barrier was reduced approximately 20 kJmol^{-1}, regardless of the chemical state of the promoter. The association barrier was more influenced by the chemical state of the promoter and was reduced by approximately 20, 15 and 5 kJmol^{-1} by the three promoters, respectively. It is suggested that the larger dependence of the association barrier on the chemical state of the promoters is due to increased repulsive interactions between nitrogen and the O/OH group at longer N-N distances. At the second closest b5 site to the promoter, the promoting effect is practically non existing. These findings indicate the observed decrease in catalytic activity of ammonia synthesis with increased presence of $Ba(OH)_2$ as much due to a higher abundance of sites in close proximity of O/OH groups.

Isotope exchange measurements (IE) have for the first time been employed for Ru-Ba/AC. The apparent activation energy (E_{app}) for the isotope exchange reaction was found highly dependent on the working state of the catalyst. Above 425°C E_{app} varies in range 64–88 kJmol^{-1}, and at lower temperatures down to 320°C in range 162–178 kJmol^{-1}, the latter in good agreement with the literature. The apparent

activation energy in the high temperature regime seems too large for dissociative adsorption and too small for associative desorption in comparison with the literature and the computational results. The presence of two distinct regimes of different apparent activation energy is therefore suggested to be caused by limitations of the isotope exchange rate by pore diffusion at higher temperatures. The variations in apparent activation within each temperature regime are mainly attributed to partially reduced Ba and BaO reacting with H_2O, which increases the intrinsic activation energy of IE as more active sites are close to O and OH groups. In that regard, gradual deactivation of the catalyst through reaction with O_2 and/or H_2O causes the isotope exchange rate to significantly decrease with time at temperatures above 500°C, when partially reduced barium and BaO are most abundant. A more controlled p_{H_2O} is advised for further studies. Similar to values reported in literature for NH_3 synthesis, the reaction order of the isotope exchange with respect to p_{N_2} was determined to 1.1 at 450°C, and 0.83 ± 0.05 and 0.88 ± 0.03 at 625°C and 700°C, respectively.

A local intermediate energy minimum was identified for nitrogen dissociation over the Ru(0001) step. The intermediate state is shown to be significantly stabilized by the presence of barium promoters. An important role of the promoter in ammonia synthesis is suggested to be stabilization of the NH_2 intermediate, as the site of adsorption is similar to the intermediate state of nitrogen dissociation at step-bridge site.

Bibliography

[1] D. Fowler, M. Coyle, U. Skiba, M. A. Sutton, J. N. Cape, S. Reis, L. J. Sheppard, A. Jenkins, B. Grizzetti, J. N. Galloway, A. Vitousek, P. amd Leach, K. Bouwman, A. F. nad Butterbach-Bahl, F. Dentener, D. Stevenson, M. Amann, and M. Voss. The global nitrogen cycle in the twenty-first century. *Philosophical Transactions of the Royal Society of London B: Biological Sciences*, 368(1621), 2013.

[2] F. Haber. The synthesis of ammonia from its elements, Nobel lecture (1920), 1920.

[3] J. W. Erisman, M. A. Sutton, J. Galloway, Z. Klimont, and W. Winiwarter. How a century of ammonia synthesis changed the world. *Nature Geoscience*, 1(10):636–639, 2008. 10.1038/ngeo325.

[4] I. Chorkendorff and J.W. Niemantsverdriet. *Concepts of Modern Catalysis and Kinetics*. Wiley, 2003.

[5] T. Bligaard, J. K. Nørskov, S. Dahl, J. Matthiesen, C. H. Christensen, and J. Sehested. The bronsted-evans-polanyi relation and the volcano curve in heterogeneous catalysis. *Journal of Catalysis*, 224(1):206–217, 2004.

[6] Z. Wang, H. Wang, and P. Hu. Possibility of designing catalysts beyond the traditional volcano curve: a theoretical framework for multi-phase surfaces. *Chemical Science*, 6:5703–5711, 2015.

[7] O. Deutschmann, H. Knözinger, K. Kochloefl, and T. Turek. *Heterogeneous Catalysis and Solid Catalysts, 1. Fundamentals*. Wiley-VCH Verlag GmbH & Co. KGaA, 2000.

[8] Erik Hörnlund. Studies of dissociation of diatomic molecules with isotope spectroscopy. *Applied Surface Science*, 199(1-4):195–210, 2002.

[9] M. Byrne and G. R. Belton. Studies of the interfacial kinetics of the reaction of nitrogen with liquid iron by the ^{15}N-^{15}N isotope exchange reaction. *Metallurgical Transactions B*, 14(3):441–449, 1983.

[10] C. Persson. Brief introducion to the density functional theory - lecture notes to M.Sc course FYS-MENA4111 - Quantum mechanical modeling of nano-materials at University of Oslo, 2013.

[11] D. S. Sholl and J. A. Steckel. *Density Functional Theory - A Practical Introduction*. Wiley, 2009.

[12] P. Atkins and J. de Paula. *Atkins' Physical Chemistry*. Oxford University Press, 9th edition, 2010.

[13] A. Soon, M. Todorova, B. Delley, and C. Stampfl. Oxygen adsorption and stability of surface oxides on Cu(111): A first-principles investigation. *Physical Review B*, 73:165424, Apr 2006.

[14] E. Skúlason, Tripkovic V., M. E. Bjoerketun, S. Gudmundsdottir, G. Karlberg, J. Rossmeisl, T. Bligaard, H. Jonsson, and J. K. Nørskov. Modeling the electrochemical hydrogen oxidation and evolution reactions on the basis of density functional theory calculations. *The Journal of Physical Chemistry C*, 114(42):18182–18197, 2010.

[15] G. S. Karlberg, T. F. Jaramillo, E. Skúlason, J. Rossmeisl, T. Bligaard, and J. K. Nørskov. Cyclic voltammograms for H on Pt(111) and Pt(100) from first principles. *Physical Review Letters*, 99:126101, Sep 2007.

[16] C. Liang, Z. Wei, Q. Xin, and C. Li. Ammonia synthesis over Ru/C catalysts with different carbon supports promoted by barium and potassium compounds. *Applied Catalysis A: General*, 208(1–2):193–201, 2001.

[17] J. J. Mortensen, L. B. Hansen, B. Hammer, and J. K. Nørskov. Nitrogen adsorption and dissociation on Fe(111). *Journal of Catalysis*, 182(2):479–488, 1999.

[18] I. Rossetti, N. Pernicone, and L. Forni. Promoters effect in Ru/C ammonia synthesis catalyst. *Applied Catalysis A: General*, 208(1–2):271–278, 2001.

[19] S. Dahl, J. Sehested, C.J.H. Jacobsen, E. Törnqvist, and I. Chorkendorff. Surface science based microkinetic analysis of ammonia synthesis over ruthenium catalysts. *Journal of Catalysis*, 192(2):391 – 399, 2000.

[20] O. Hinrichsen, F. Rosowski, M. Muhler, and G. Ertl. The microkinetics of ammonia synthesis catalyzed by cesium-promoted supported ruthenium. *Chemical Engineering Science*, 51(10):1683 – 1690, 1996. Chemical Reaction Engineering: From Fundamentals to Commercial Plants and Products.

[21] O Hinrichsen. Kinetic simulation of ammonia synthesis catalyzed by ruthenium. *Catalysis Today*, 53(2):177 – 188, 1999.

[22] C.J. Zhang, M. Lynch, and P. Hu. A density functional theory study of stepwise addition reactions in ammonia synthesis on Ru(0001). *Surface Science*, 496(3):221 – 230, 2002.

[23] G. Ertl. Primary steps in catalytic synthesis of ammonia. *Journal of Vacuum Science & Technology A*, 1(2):1247–1253, 1983.

[24] P. Stoltze and J. K. Nørskov. Bridging the "pressure gap" between ultrahigh-vacuum surface physics and high-pressure catalysis. *Physical Review Letters*, 55:2502–2505, Nov 1985.

[25] B. Fastrup. Temperature programmed adsorption and desorption of nitrogen on iron ammonia synthesis catalysts, and consequences for the microkinetic analysis of NH_3 synthesis. *Topics in Catalysis*, 1(3):273–283, 1994.

[26] J.J. Mortensen, Y. Morikawa, B. Hammer, and J.K. Nørskov. Density functional calculations of N_2 adsorption and dissociation on a Ru(0001) surface. *Journal of Catalysis*, 169(1):85 – 92, 1997.

[27] A. B. Anton, N. R. Avery, T. E. Madey, and W. H. Weinberg. The coadsorption of nitrogen with carbon monoxide and oxygen on the Ru(001) surface: Local chemical interactions in mixed overlayers. *The Journal of Chemical Physics*, 85(1):507–518, 1986.

[28] P. Feulner and D. Menzel. Unusual coverage dependence of a sticking coefficient: N_2/Ru(001). *Physical Review B*, 25:4295–4297, Mar 1982.

[29] S. Dahl, E. Törnqvist, and I. Chorkendorff. Dissociative adsorption of N_2 on Ru(0001): A surface reaction totally dominated by steps. *Journal of Catalysis*, 192(2):381–390, 2000.

[30] Y. Lilach, I.M. Danziger, and M. Asscher. Second order isothermal desorption kinetics. *Catalysis Letters*, 76(1):35–39, 2001.

[31] H. Shi, K. Jacobi, and G. Ertl. Dissociative chemisorption of nitrogen on Ru(0001). *The Journal of Chemical Physics*, 99(11):9248–9254, 1993.

[32] M. J. Murphy, J. F. Skelly, A. Hodgson, and B. Hammer. Inverted vibrational distributions from N_2 recombination at Ru(001): Evidence for a metastable molecular chemisorption well. *The Journal of Chemical Physics*, 110(14):6954–6962, 1999.

[33] T. Zambelli, J. Trost, J. Wintterlin, and G. Ertl. Diffusion and atomic hopping of N atoms on Ru(0001) studied by scanning tunneling microscopy. *Physical Review Letters*, 76:795–798, Jan 1996.

[34] L. Romm, G. Katz, R. Kosloff, and M. Asscher. Dissociative chemisorption of N_2 on Ru(001) enhanced by vibrational and kinetic energy: Molecular beam experiments and quantum mechanical calculations. *The Journal of Physical Chemistry B*, 101(12):2213–2217, 1997.

[35] R. C. Egeberg, J. H. Larsen, and I. Chorkendorff. Molecular beam study of N_2 dissociation on Ru(0001). *Physcal Chemisty Chemical Physics*, 3:2007–2011, 2001.

[36] S. Dahl, A. Logadóttir, R. C. Egeberg, J. H. Larsen, I. Chorkendorff, E. Tórnqvist, and J. K. Nørskov. Role of steps in N_2 activation on Ru(0001). *Physical Review Letters*, 83(9):1814–1817, 1999. PRL.

[37] J. J. Mortensen, B. Hammer, and J. K. Nørskov. Alkali promotion of N_2 dissociation over Ru(0001). *Physical Review Letters*, 80(19):4333–4336, 1998. PRL.

[38] J. J. Mortensen, B. Hammer, and J. K. Nørskov. A theoretical study of adsorbate-adsorbate interactions on Ru(0001). *Surface Science*, 414(3):315–329, 1998.

[39] N. D. Lang, S. Holloway, and J. K. Nørskov. Electrostatic adsorbate-adsorbate interactions: The poisoning and promotion of the molecular adsorption reaction. *Surface Science*, 150(1):24–38, 1985.

[40] L. Forni, D. Molinari, I. Rossetti, and N. Pernicone. Carbon-supported promoted Ru catalyst for ammonia synthesis. *Applied Catalysis A: General*, 185(2):269–275, 1999.

[41] S. Kowalczyk, Z.and Jodzis, J. Raróg, W.and Zieliński, Jerzy Pielaszek, and A. Presz. Carbon-supported ruthenium catalyst for the synthesis of ammonia. the effect of the carbon support and barium promoter on the performance. *Applied Catalysis A: General*, 184(1):95–102, 1999.

[42] M. Kitano, Y. Inoue, Y.and Yamazaki, F. Hayashi, S. Kanbara, S. Matsuishi, T. Yokoyama, S. Kim, M. Hara, and H. Hosono. Ammonia synthesis using a stable electride as an electron donor and reversible hydrogen store. *Nature Chemistry*, 4(11):934–940, 2012. 10.1038/nchem.1476.

[43] E. Truszkiewicz, W. Raró-Pilecka, K. Schmidt-Szałwski, S. Jodzis, E. Wilczkowska, D. Łmot, Z. Kaszkur, Z. Karpiński, and Z. Kowalczyk. Barium-promoted Ru/carbon catalyst for ammonia synthesis: State of the system when operating. *Journal of Catalysis*, 265(2):181–190, 2009.

[44] T. W. Hansen, P. L. Hansen, S. Dahl, and C. J. H. Jacobsen. Support effect and active sites on promoted ruthenium catalysts for ammonia synthesis. *Catalysis Letters*, 84(1-2):7–12, 2002.

[45] H. S. Zeng, K. Inazu, and K. Aika. The working state of the barium promoter in ammonia synthesis over an active-carbon-supported ruthenium catalyst using barium nitrate as the promoter precursor. *Journal of Catalysis*, 211(1):33–41, 2002.

[46] W. Raróg, Z. Kowalczyk, J. Sentek, D. Składanowski, and J. Zieliński. Effect of K, Cs and Ba on the kinetics of NH_3 synthesis over carbon-based ruthenium catalysts. *Catalysis Letters*, 68(3):163–168, 2000.

[47] Z. Kowalczyk, S. Jodzis, W. Raróg, J. Zielinski, Zieliński, and J. Pielaszek. Effect of potassium and barium on the stability of a carbon-supported ruthenium catalyst for the synthesis of ammonia. *Applied Catalysis A: General*, 173(2):153–160, 1998.

[48] Z. Kowalczyk, S. Jodzis, and J. Sentek. Studies on kinetics of ammonia synthesis over ruthenium catalyst supported on active carbon. *Applied Catalysis A: General*, 138(1):83–91, 1996.

[49] Z. Kowalczyk, J. Sentek, S. Jodzis, E. Mizera, J. Góralski, T. Paryjczak, and R. Diduszko. An alkali-promoted ruthenium catalyst for the synthesis of ammonia, supported on thermally modified active carbon. *Catalysis Letters*, 45(1):65–72, 1997.

[50] S. A. Wasileski and M. J. Janik. A first-principles study of molecular oxygen dissociation at an electrode surface: a comparison of potential variation and coadsorption effects. *Physical Chemistry Chemical Physics*, 10(25):3613–3627, 2008.

[51] N. Saadatjou, A. Jafari, and S. Sahebdelfar. Ruthenium nanocatalysts for ammonia synthesis: A review. *Chemical Engineering Communications*, 202(4):420–448, 2015.

[52] Z. Kowalczyk, M. Krukowski, W. Raró-Pilecka, D. Szmigiel, and J. Zieliński. Carbon-based ruthenium catalyst for ammonia synthesis: Role of the barium and caesium promoters and carbon support. *Applied Catalysis A: General*, 248(1–2):67–73, 2003.

[53] Francisco R. Garcia-Garcia, Nicolas Bion, Daniel Duprez, Inmaculada Rodriguez-Ramos, and Antonio Guerrero-Ruiz. H_2/D_2 isotopic exchange: A tool to characterize complex hydrogen interaction with carbon-supported ruthenium catalysts. *Catalysis Today*, 259, Part 1:9 – 18, 2016. ICP, a meeting point for catalysis around the world. 40th Anniversary.

[54] R. Hancke, Z. Li, and R. Haugsrud. Hydrogen surface exchange on proton conducting oxides studied by gas phase analysis with mass spectrometry. *Journal of Membrane Science*, 439:68 – 77, 2013.

[55] Z. Li, R. Haugsrud, and T. Norby. Oxygen bulk diffusion and surface exchange in Sr-substituted $La_2NiO_{4+\delta}$. *Solid State Ionics*, 184(1):42 – 46, 2011. Exploring Chemical and Structural Complexity of Novel Ion Conductors.

[56] Clara Anghel and Qian Dong. A gas phase analysis technique applied to in-situ studies of gas-solid interactions. *Journal of Materials Science*, 42(10):3440–3453, 2007.

[57] S. M. Hunter, D. H. Gregory, J. S. J. Hargreaves, M Richard, D. Duprez, and N. Bion. A study of $^{15}N/^{14}N$ isotopic exchange over cobalt molybdenum nitrides. *ACS Catalysis*, 3(8):1719–1725, 2013. PMID: 24265977.

[58] G. E. Moore and F. C. Unterwald. Interaction of nitrogen with Mo and the reaction $^{28}N_2 + {}^{30}N_2 = 2^{29}N_2$ catalyzed by mo and observed by mass spectrometer. *The Journal of Chemical Physics*, 48(12):5393–5408, 1968.

[59] T. Hikita, Y. Kadowaki, and K. Aika. Promoter action of alkali nitrate in raney ruthenium catalyst for activation of dinitrogen. *The Journal of Physical Chemistry*, 95(23):9396–9402, 1991.

[60] Y. Ogata, K. Aika, and T. Onishi. Isotopic equilibration reaction of dinitrogen over raney ruthenium with and without potassium. *Chemistry Letters*, 13(5):825–828, 1984.

[61] O. Hinrichsen, F. Rosowski, A. Hornung, M. Muhler, and G. Ertl. The kinetics of ammonia synthesis over Ru-based catalysts: 1. the dissociative chemisorption and associative desorption of N_2. *Journal of Catalysis*, 165(1):33–44, 1997.

[62] S. Kitano, M.and Kanbara, Y. Inoue, N. Kuganathan, P. V. Sushko, T. Yokoyama, M. Hara, and H. Hosono. Electride support boosts nitrogen dissociation over ruthenium catalyst and shifts the bottleneck in ammonia synthesis. *Nature Communications*, 6, 2015.

[63] Y. Hayashi, F.and Toda, Y. Kanie, M. Kitano, Y. Inoue, T. Yokoyama, M. Hara, and H. Hosono. Ammonia decomposition by ruthenium nanoparticles loaded on inorganic electride C12A7:e^-. *Chemical Science*, 4:3124–3130, 2013.

[64] M. C. Payne, M. P. Teter, D. C. Allan, T. A. Arias, and J. D. Joannopoulos. Iterative minimization techniques for *ab initio* total-energy calculations: molecular dynamics and conjugate gradients. *Reveiws of Modern Physics*, 64:1045–1097, Oct 1992.

[65] P. E. Blöchl. Projector augmented-wave method. *Physical Review B*, 50:17953–17979, Dec 1994.

[66] G. Kresse and D. Joubert. From ultrasoft pseudopotentials to the projector augmented-wave method. *Physical Review B*, 59:1758–1775, Jan 1999.

[67] Jochen Heyd, Gustavo E. Scuseria, and Matthias Ernzerhof. Hybrid functionals based on a screened coulomb potential. *The Journal of Chemical Physics*, 118(18):8207–8215, 2003.

[68] J. Hafner. Ab-initio simulations of materials using VASP: Density-functional theory and beyond. *Journal of Computational Chemistry*, 29(13):2044–2078, 2008.

[69] J. Paier, M. Marsman, K. Hummer, G. Kresse, I. C. Gerber, and J. G. Ángyán. Screened hybrid density functionals applied to solids. *The Journal of Chemical Physics*, 124(15), 2006.

[70] J. P. Perdew, K. Burke, and M. Ernzerhof. Generalized gradient approximation made simple. *Physical Review Letters*, 77:3865–3868, Oct 1996.

[71] G. Henkelman, B. P. Uberuaga, and H. Jonsson. A climbing image nudged elastic band method for finding saddle points and minimum energy paths. *The Journal of Chemical Physics*, 113(22):9901–9904, 2000.

[72] B. Hammer, L. B. Hansen, and J. K. Nørskov. Improved adsorption energetics within density-functional theory using revised perdew-burke-ernzerhof functionals. *Physical Review B*, 59:7413–7421, Mar 1999.

[73] A. Logadóttir and J.K. Nørskov. Ammonia synthesis over a Ru(0001) surface studied by density functional calculations. *Journal of Catalysis*, 220(2):273 – 279, 2003.

[74] M. Ernzerhof and G. E. Scuseria. Assessment of the perdew-burke-ernzerhof exchange-correlation functional. *The Journal of Chemical Physics*, 110(11):5029–5036, 1999.

[75] K. Honkala, A. Hellman, I. N. Remediakis, A. Logadóttir, A. Carlsson, S. Dahl, C. H. Christensen, and J. K. Nørskov. Ammonia synthesis from first-principles calculations. *Science*, 307(5709):555–558, 2005.

[76] F. Rosowski, O. Hinrichsen, M. Muhler, and G. Ertl. The temperature-programmed desorption of N_2 from a Ru/MgO catalyst used for ammonia synthesis. *Catalysis Letters*, 36(3):229–235, 1996.

[77] J. Wellendorff, T. L. Silbaugh, D. Garcia-Pintos, J. K. Nørskov, T. Bligaard, F. Studt, and C. T. Campbell. A benchmark database for adsorption bond energies to transition metal surfaces and comparison to selected DFT functionals. *Surface Science*, 640:36 – 44, 2015. Reactivity Concepts at Surfaces: Coupling Theory with Experiment.

[78] J. A. Herron, S. Tonelli, and M. Mavrikakis. Atomic and molecular adsorption on Ru(0001). *Surface Science*, 614:64 – 74, 2013.

[79] W. Raróg-Pilecka, D. Szmigiel, Z. Kowalczyk, S. Jodzis, and J. Zielinski. Ammonia decomposition over the carbon-based ruthenium catalyst promoted with barium or cesium. *Journal of Catalysis*, 218(2):465 – 469, 2003.

[80] W. Raróg, Z. Kowalczyk, J. Sentek, D. Składanowski, D Szmigiel, and J. Zieliński. Decomposition of ammonia over potassium promoted ruthenium catalyst supported on carbon. *Applied Catalysis A: General*, 208(1-2):213 – 216, 2001.

[81] J. B. Smith. *Mixed oxygen ion/electron cconductor for oxygen seperationprocesses: Surface kinetics and cataion diffusion.* PhD thesis, University of Oslo, 2005.